New Jersey Institute of Technology
Digital Commons @ NJIT

Dissertations | Electronic Theses and Dissertations

Spring 5-31-2004

Boron and phosphorous implantation into (100) germanium : modeling and investigation of dopant annealing behavior

Yong Seok Suh
New Jersey Institute of Technology

Follow this and additional works at: https://digitalcommons.njit.edu/dissertations

Part of the Materials Science and Engineering Commons

Recommended Citation

Suh, Yong Seok, "Boron and phosphorous implantation into (100) germanium : modeling and investigation of dopant annealing behavior" (2004). *Dissertations*. 640.
https://digitalcommons.njit.edu/dissertations/640

This Dissertation is brought to you for free and open access by the Electronic Theses and Dissertations at Digital Commons @ NJIT. It has been accepted for inclusion in Dissertations by an authorized administrator of Digital Commons @ NJIT. For more information, please contact digitalcommons@njit.edu.

Copyright Warning & Restrictions

The copyright law of the United States (Title 17, United States Code) governs the making of photocopies or other reproductions of copyrighted material.

Under certain conditions specified in the law, libraries and archives are authorized to furnish a photocopy or other reproduction. One of these specified conditions is that the photocopy or reproduction is not to be "used for any purpose other than private study, scholarship, or research." If a, user makes a request for, or later uses, a photocopy or reproduction for purposes in excess of "fair use" that user may be liable for copyright infringement,

This institution reserves the right to refuse to accept a copying order if, in its judgment, fulfillment of the order would involve violation of copyright law.

Please Note: The author retains the copyright while the New Jersey Institute of Technology reserves the right to distribute this thesis or dissertation

Printing note: If you do not wish to print this page, then select "Pages from: first page # to: last page #" on the print dialog screen

The Van Houten library has removed some of the personal information and all signatures from the approval page and biographical sketches of theses and dissertations in order to protect the identity of NJIT graduates and faculty.

ABSTRACT

BORON AND PHOSPHORUS IMPLANTATION INTO (100) GERMANIUM: MODELING AND INVESTIGATION OF DOPANT ANNEALING BEHAVIOR

by
Yong Seok Suh

Germanium is increasingly being considered at this time for future silicon compatible optoelectronic and complementary metal oxide semiconductor (CMOS) device application. Germanium implantation will be a critical process for future device fabrication. However, critical properties like Pearson parameters and dopant activation temperatures are not well established. In this study, boron and phosphorus were implanted into (100) germanium with energies ranging from 20 to 320 keV and doses of 5×10^{13} to 5×10^{16} cm^{-2}. The behavior of the boron and phosphorus before and after annealing for 3 hours at 400, 600 or 800°C in ultra high purity nitrogen were characterized using secondary ion mass spectrometry (SIMS), spreading resistance profiling (SRP) measurements, Hall Effect measurement, X-ray diffraction (XRD) measurement, and Rutherford backscattering spectrometry (RBS). A predictive model for the implanted dopant distribution's dependence on energy was developed using the experimentally determined implant moments combined with Pearson distributions and the post-annealing electrical, structural and diffusion behavior was characterized. Results from numeric simulation and analytic calculations using Lindard-Scharff-Schiott (LSS) theory are presented to offer insight into the physics of the pre-annealed implanted dopant distributions.

BORON AND PHOSPHORUS IMPLANTATION INTO (100) GERMANIUM: MODELING AND INVESTIGATION OF DOPANT ANNEALING BEHAVIOR

by
Yong Seok Suh

A Dissertation
Submitted to the Faculty of
New Jersey Institute of Technology
in Partial Fulfillment of the Requirements for the Degree of
Doctor of Philosophy in Materials Science and Engineering

Interdisciplinary Program in Materials Science and Engineering

May 2004

Copyright © 2004 by Yong Seok Suh

ALL RIGHTS RESERVED

APPROVAL PAGE

BORON AND PHOSPHORUS IMPLANTATION INTO (100) GERMANIUM: MODELING AND INVESTIGATION OF DOPANT ANNEALING BEHAVIOR

Yong Seok Suh

Dr. Roland A. Levy, Dissertation Advisor — Date
Distinguished Professor of Physics, NJIT

Dr. Malcolm S. Carroll, Committee Member — Date
Member of Technical Staff, Sandia National Laboratories, Albuquerque, NM

Dr. Marek Sosnowski, Committee Member — Date
Professor of Electrical and Computer Engineering, NJIT

Dr. Anthony Fiory, Committee Member — Date
Research Professor of Physics, NJIT

Dr. Andrei Sirenko, Committee Member — Date
Assistant Professor of Physics, NJIT

Dr. Conor Rafferty, Committee Member — Date
Chief Executive Officer, Noble Device Technologies, Newark, NJ

BIOGRAPHICAL SKETCH

Author: Yong Seok Suh

Degree: Doctor of Philosophy

Date: May 2004

Undergraduate and Graduate Education:

- Doctor of Philosophy in Materials Science and Engineering
  New Jersey Institute of Technology, Newark, NJ, 2004
- Master of Science in Materials Science and Engineering
  New Jersey Institute of Technology, Newark, NJ, 2001
- Bachelor of Science in Metallurgical Engineering
  Kyung-pook National University, Deagu, Republic of Korea, 1998

Major: Materials Science and Engineering

Presentations and Publications:

Y. S. Suh, R. A. Levy, M. S. Carroll, C. A. King, and A. Sahiner
"Modeling of Boron and Phosphorus Implantation into (100) Germanium," submitted to *J. Appl. Phys.* 2004.

Y. S. Suh, M. S. Carroll, R. A. Levy, A. Sahiner, and C. A. King
"Phosphorus and Boron Implantation into (100) Germanium,"
Materials Research Society Symposium Proceedings Vol. 809, B8.11, San Francisco, CA, April 2004.

"... to begin always anew, to make, to reconstruct, and to not spoil, to refuse to bureaucratize the mind, to understand and to live life as a process-live to become"

- Paulo Freire -

To my loved family

감사합니다.

ACKNOWLEDGMENT

I wish to express my sincere gratitude to my dissertation advisor, Dr. Roland A. Levy, who not only served as my research supervisor, but also provided valuable and countless resources, insight, and intuition. I am thankful for his support, encouragement, and reassurance during the course of this research.

I would like to express my deepest gratitude to Dr. Malcolm S. Carroll, who advised and provided me with valuable guidance and suggestions throughout the work. I am grateful for his efforts and kindness.

Sincere gratitude also goes to Dr. Marek Sosnowski and Dr. Anthony Fiory for serving as committee members. Special thanks are given to Dr. Andrei Sirenko and Dr. Conor Rafferty for their technical assistance and comments as well as for serving as members of my dissertation committee.

I gratefully acknowledge helpful comments from Dr. Alper Sahiner, Dr. Clifford King, and Dr. Gabriele Bisognin regarding this work.

I also would like to thank my fellow graduate students, Dianhong (Diane) Luo and Liwei Li, of the Chemical Vapor Deposition Laboratory at New Jersey Institute of Technology for their friendship and encouragement throughout these years. I also would like to sincerely thank my family for their endless love.

This work was partially supported by Agere Systems. I also thank Evans East for performing the SIMS measurements.

TABLE OF CONTENTS

Chapter	Page
1 INTRODUCTION	1
1.1 Motivation of the Research	1
1.2 Renewed Interest in Germanium	1
1.3 Recent Advances in Process Technologies for Germanium	5
2 REVIEW OF LITERATURE	7
2.1 Ion Stopping Theory	7
2.1.1 Stopping Powers based on LSS theory	8
2.1.2 Monte-Carlo based SRIM	13
2.2 Channeling	17
2.3 Analytical Modeling Method	22
2.3.1 Distribution Functions	22
2.3.2 Pearson Distribution	23
3 EXPERIMENTAL METHODOLOGY	28
3.1 Description of Samples	28
3.2 Process of Ion Implantation	29
3.3 Process of Activation Annealing	30
4 CHARACTERIZATION METHODS	34
4.1 Secondary Ion Mass Spectrometry (SIMS)	34
4.2 Spreading Resistance Profiling (SRP)	38
4.3 X-ray Diffraction (XRD)	41
4.4 Hall Effect Measurement	43

TABLE OF CONTENTS
(Continued)

Chapter **Page**

4.5 Rutherford Backscattering Spectrometry (RBS) 45

5 RESULTS AND DISCUSSION 47

5.1 Observation of Dopants Implanted into Germanium 47

5.1.1 Observation of Dopant Distribution by SIMS 48

5.1.2 Modeling by Pearson Distribution 52

5.1.3 Relationship between Moments and Energy 59

5.2 Activation Annealing 71

5.2.1 Boron Activation Behavior 71

5.2.2 Phosphorus Activation Behavior 75

5.3 Observation of Damage Induced by Ion Implantation 82

6 CONCLUSIONS 93

APPENDIX PROGRAMMING FOR CALCULATION OF MOMENTS 96

REFERENCES 101

LIST OF TABLES

Table		Page
1.1	Properties of germanium and silicon at room temperature	3
1.2	Effective masses for electron and hole at room temperature	5
2.1	Constants for boron or phosphorus in germanium	11
2.2	Calculation of ψ_1 and $\psi_{1/2}$ for born and phosphorus implanted into germanium and silicon	20
2.3	The different Pearson types and Gaussian distribution with conditions	26
3.1	Certified test data of germanium and silicon wafers	28
3.2	Conditions of ion implantation into (100) germanium and silicon wafers	30
4.1	Instrument conditions and detection limits for the analyses	35
4.2	Values of K_x for various assumed values of G_x	42
5.1	The implantation conditions and the obtained areal density from SIMS measurement for the boron implanted into germanium and silicon witness wafers	51
5.2	The implantation conditions and the obtained areal density from SIMS measurement for the phosphorus implanted into germanium and silicon witness wafers	51
5.3	The first four moments with Pearson type for boron and phosphorus in germanium	53
5.4	The first four moments with Pearson type for boron and phosphorus in silicon	54
5.5	Summary of Pearson parameters for boron implanted into germanium	70

LIST OF TABLES
(Continued)

Figure **Page**

5.6 Summary of Pearson parameters for phosphorus implanted into germanium... 70

5.7 Sheet resistance from SRP for boron in germanium 74

5.8 Sheet resistance from SRP for phosphorus in germanium 77

5.9 The result of ^{11}B (p,α) ^{8}Be nuclear reaction 84

LIST OF FIGURES

Figure		Page
1.1	Optical absorption coefficients vs. wavelength for the selected semiconductor materials	2
1.2	Schematic diagram for energy band vs. wave vector for germanium	4
1.3	Schematic of epitaxial germanium growth on silicon substrate using graded buffer layer ($Si_{1-x}Ge_x$)	6
2.1	Description of the ion *range*, R, and *projected range*, R_p	7
2.2	Schematic diagram before a collision between two atoms	8
2.3	Schematic diagram after a collision between two atoms	9
2.4	Nuclear and electronic energy loss vs. energies for (a) boron and (b) phosphorus in germanium and silicon, calculated from LSS theory	12
2.5	SRIM simulation: (a) ion trajectories of 180 boron ions (b) ion ranges of 99,999 boron ions implanted into amorphous germanium at 60 keV	14
2.6	Effect of the adopted potential for nuclear stopping power	15
2.7	SRIM simulation of the collision events for phosphorus implant into germanium at 170 keV, which was carried out 99,999 counts	17
2.8	Schematic illustration of channeling	18
2.9	Back-scattering yield around a channeling direction. Yield is a minimum when beam is well aligned with a channel	18
2.10	Model of germanium crystal seen along the <100> direction	21
2.11	Model of germanium crystal tilted 7° with respect to <100> direction	21

LIST OF FIGURES
(Continued)

Figure		Page
2.12	Schematic illustration of the skewness and kurtosis	24
3.1	Schematic of the annealing system	31
3.2	Effect of annealing at high temperature: 60 keV, 1×10^{15} cm^{-2} boron implantation into germanium with annealing temperature of (a) 600°C and (b) 800°C for 3 hours in N_2 (60×10 magnification)	33
4.1	Schematic diagram of the sputtering process	34
4.2	Example of "knock-on" effect with primary ion beam energies	37
4.3	Schematic diagram of spreading resistance profiling	39
4.4	The principle of Hall effect measurement	43
4.5	Detection of an amorphous layer with RBS. (a) Ion beam penetrating crystal in "open" direction; (b) corresponding spectrum of channel and random; (c) ion beam scattered from amorphous layer; (d) corresponding spectrum	46
5.1	SIMS data of (a) boron and (b) phosphorus implanted into germanium with various doses and energies	49
5.2	SIMS data of (a) boron and (b) phosphorus implanted into silicon with various doses and energies	50
5.3	The SIMS data and the fitted Pearson distribution curves of (a) 60 keV boron and (b) 170 keV phosphorus implanted into germanium with various doses	56
5.4	Comparison of experimental data from SIMS and fitted Pearson curves with various energies and same dose (5×10^{13} cm^{-2}): (a) boron and (b) phosphorus implantation into germanium	57

LIST OF FIGURES
(Continued)

Figure **Page**

5.5 Comparison of SIMS data, Gaussian distribution based on LSS theory, and SRIM simulation compared to the fitted Pearson distribution curves of (a) 60 keV, 1×10^{15} cm^{-2} boron and (b) 170 keV, 1×10^{15} cm^{-2} phosphorus implanted into germanium 58

5.6 Experimental points, fitted curve, and data from LSS theory and SRIM simulation for *projected range* (R_p) of (a) boron and (b) phosphorus 5×10^{13} cm^{-2} implants into germanium. The fitted curve for boron is $R_p[\mu m] = 0.00786E^{0.783}$ and $R_p[\mu m] = 0.00311E^{0.780}$ for phosphorus. The unit of energy is keV 60

5.7 Experimental points, fitted curve, and data from LSS theory and SRIM simulation for straggle (σ_p) of 5×10^{13} cm^{-2} (a) boron and (b) phosphorus implants into germanium. The fitted curves are $\sigma_p[\mu m] = 0.0101E^{0.537}$ and $\sigma_p[\mu m] = 0.00216E^{0.713}$ for boron and phosphorus, respectively. The unit of energy is keV 63

5.8 Experimental points, fitted curves, and data from SRIM simulation for skewness (γ) of 5×10^{13} cm^{-2} (a) boron and (b) phosphorus implants into germanium. The fitted curves are $\gamma = 3.53-(0.707)\ln E$ and $\gamma = 3.00-(0.474)\ln E$ for boron and phosphorus, respectively. The unit of energy is keV 65

5.9 The kurtosis (β) dependence on energy for 5×10^{13} cm^{-2} (a) boron and (b) phosphorus implants calculated from SIMS profiles and SRIM simulated profiles. The experimental kurtosis was fit with (a) $\beta = 3.33+(1.64)\gamma^2$ for boron and (b) $\beta = 2.46+(2.51)\gamma^2$ for phosphorus 67

5.10 Domains of Pearson types on the β-γ^2 plane: the experimental points and SRIM simulation (a) for boron and (b) for phosphorus implantation into germanium and silicon. The region of Pearson type is indicated (i.e. I, IV, or VI). The line A and B are the boundary between Pearson types 69

5.11 Comparison of SIMS data for 60 keV, 1×10^{15} cm^{-2} boron implanted into germanium after 400 and 600°C annealing, and as-implanted case 72

LIST OF FIGURES
(Continued)

Figure **Page**

5.12 SIMS and SRP data of the as-implanted and annealed cases (3 hours at either 400 or 600°C in N_2) for 60 keV, 1×10^{15} cm^{-2} boron implant into germanium. The n and p's indicate carrier type 73

5.13 Summary of peak for boron concentrations measured from SRP and SIMS assuming single crystal mobilities for germanium. Previously reported solid solubilities of boron in germanium were also shown 75

5.14 SIMS and SRP data of the as-implanted and annealed cases (3 hours at either 400 or 600°C in N_2) for 170 keV, 5×10^{16} cm^{-2} phosphorus implant into germanium. The n and p's indicate carrier type 76

5.15 SIMS of the as-implanted and annealed cases (3 horus at either 400 or 600°C in N_2) for 170 keV, 5×10^{13} cm^{-2} phosphorus implant into germanium 79

5.16 SIMS and SRP data of the as-implanted and annealed cases (3 hours at either 400 or 600°C in N_2) for 170 keV, 1×10^{15} cm^{-2} phosphorus implant into germanium 80

5.17 Summary of peak phosphorus concentrations measured from SRP and SIMS assuming single crystal mobilities for germanium. Previously reported solid solubilities of phosphorus in germanium were also shown 81

5.18 The RBS spectra for various boron and phosphorus doses implanted into germanium. The red curve indicates random spectrum 83

5.19 The random spectra of α particle from ^{11}B (p,α) ^{8}Be nuclear reaction on 5×10^{16} and 1×10^{15} cm^{-2} boron implant into germanium 85

5.20 The rocking curves for 60 keV boron implantation into germanium with various doses 87

5.21 Comparison of two rocking curves related to 5×10^{13} and 1×10^{15} cm^{-2} boron implanted into germanium with the energy of 60 keV 87

LIST OF FIGURES
(Continued)

Figure **Page**

5.22 The rocking curves for 170 keV phosphorus implantation into germanium with various doses 89

5.23 Comparison of the rocking curves of boron and phosphorus with the dose of 5×10^{16} cm^{-2} 89

5.24 The reciprocal space map around (224) reflection of the germanium implanted with 5×10^{16} cm^{-2} (a) boron and (b) phosphorus 91

CHAPTER 1

INTRODUCTION

1.1 Motivation of the Research

Interest in germanium has been renewed because of recent process advances, such as progress in low defect density $Si_{1-x}Ge_x$ heteroepitaxy on silicon [1] and the development of new high-k gate dielectrics for germanium based metal oxide semiconductor field effect transistors (MOSFET) [2]. The progress in these areas has resulted in significant efforts to develop germanium on silicon or germanium on insulator (GeOI) communication wavelength photodetectors and high mobility FETs [3-5]. Ion implantation and dopant activation are crucial steps for the fabrication of these device structures. However, critical modeling, for which modeling parameters typically available for silicon fabrication (e.g. Pearson's implant parameters, accurate diffusivities, and solid solubilities) are either not reliable [6, 7] or are not available for germanium. Therefore, it is necessary to establish these experimental parameters.

1.2 Renewed Interest in Germanium

Germanium, which was discovered by Winkler in 1886 [8], and which was the material used for the first transistor [9] in 1947, is a gray-white semiconductor material. Several material properties of germanium like a suitable band gap (0.67 eV), high absorption coefficients at the wavelengths of interest (1.3 and 1.55 μm [10]), Figure 1.1, and high hole mobility make it a superior choice for fabrication of detectors and transistors to silicon. Some critical properties of germanium and silicon [11-15] are shown in

Table 1.1. Historically, however, the lack of a stable oxide on germanium (germanium oxide (GeO_2) is water-soluble and dissociates at 800°C [16]) as well as the inability to epitaxially grow thick layers of germanium on silicon, has made it difficult to integrate germanium into mainstream silicon based complementary metal oxide semiconductor (CMOS) technologies.

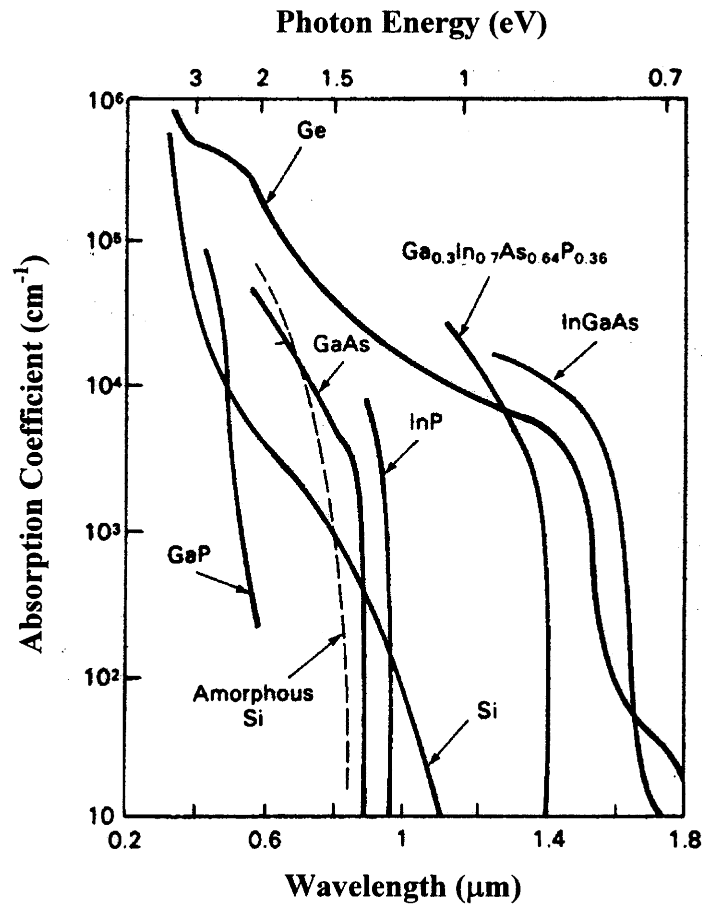

Figure 1.1 Optical absorption coefficients vs. wavelength for the selected semiconductor materials [17].

Table 1.1 Properties of Germanium and Silicon at Room Temperature

		Germanium	Silicon
Lattice type		Diamond	Diamond
Atomic number		32	14
Lattice constant a_0 (Å)		5.657	5.431
Energy gap (eV) at 300 K		0.67 (Indirect)	1.11 (Indirect)
Dielectric constant ε_r		16.2	11.9
Atomic weight		72.590	28.090
Atomic density (atoms/cm^3)		4.419×10^{22}	4.995×10^{22}
Bulk intrinsic mobility (cm^2/V-s)	Electrons	3900	1450
	Holes	1800	505
Melting point (°C)		938.3	1414

The lattice structure of germanium is the diamond configuration, which is the same as silicon, but the lattice constant of germanium is 5.657 Å, which is 4.2% greater than that of silicon (Table 1.1).

The electron and hole mobility in germanium is three times as high as that in silicon. For this reason, germanium is attracting attention in the field of silicon based high-frequency devices. The carrier mobility (μ) is related with the effective mass (m^*) of the respective carrier in Equation (1.1):

$$\mu = \frac{q}{m^*}\tau, \qquad (1.1)$$

where q is the carrier charge (= 1.602×10^{-19} C), and τ is the transport scattering time [12]. The effective mass is inversely proportional to the curvature of band in the relationship

between energy (E) and wave vector (**k**), as described in Equation (1.2) and Figure 1.2 [18-20]:

$$m^{*} \propto \frac{1}{d^{2}E/d\mathrm{k}^{2}}. \tag{1.2}$$

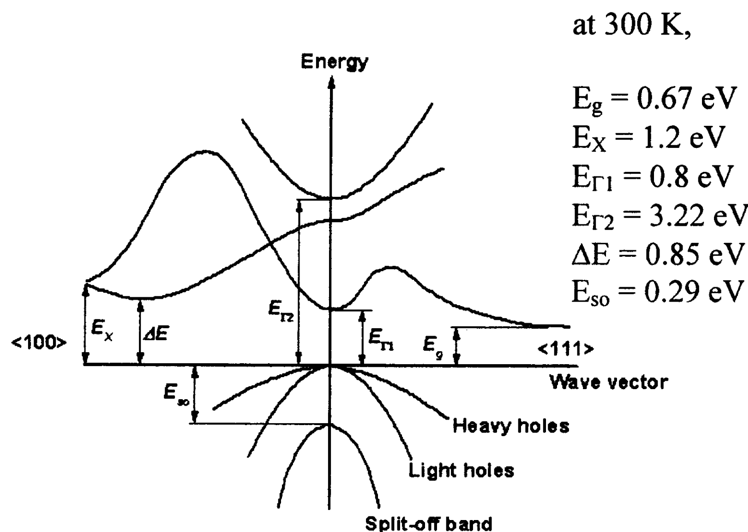

Figure 1.2 Schematic diagram for energy band vs. wave vector for germanium [19].

In Table 1.2, the known values for the effective masses for germanium and silicon are shown. The effective masses of germanium are smaller than those of silicon. Thus, according to Equation (1.1), the carrier mobility of germanium is higher than that of silicon. To get the conductivity effective mass (m_n^*) for electrons, Equation (1.3) is used:

$$\frac{1}{m_n^{*}} = \frac{1}{3}\left(\frac{1}{m_l} + \frac{2}{m_t}\right), \tag{1.3}$$

where m_l and m_t are the longitudinal and transverse effective mass, respectively [18].

Table 1.2 Effective Masses for Electron and Hole at Room Temperature [12]

	Germanium	Silicon
Longitudinal effective mass (m_l)	$0.08m_0$	$0.19m_0$
Transverse effective mass (m_t)	$1.59m_0$	$0.91m_0$
Conductive effective mass for electron (m_n^*)	$0.26m_0$	$0.12m_0$
Heavy hole effective mass (m_{hh})	$0.28m_0$	$0.53m_0$
Light hole effective mass (m_{lh})	$0.04m_0$	$0.15m_0$
Split-off band effective mass (m_{so})	$0.09m_0$	$0.23m_0$

Note that m_0 is the free electron mass in vacuum (= 9.11×10^{-28} g).

1.3 Recent Advances in Process Technologies for Germanium

As mentioned in Section 1.2, germanium does not have a stable oxide, which is a major problem for the fabrication of semiconductor devices. Recant technologies in the fabrication of a thin high-permittivity (k) gate dielectric material, such as zirconium oxide (ZrO_2) or germanium oxynitride (GeON) for germanium have been presented [2, 4]. For example, Chui, et al. successfully developed germanium MOSFET having a ZrO_2 gate dielectric with an equivalent oxide thickness (EOT) of 6-10 Å, which showed relatively good MOSFET I-Vs with high mobilities [2].

In optical communication, 1.3 and 1.55 μm wavelengths are preferred because of the low attenuation in the fiber. Germanium is a good candidate because of a high absorption coefficient in this wavelength range as shown in Figure 1.1. Recently, germanium optoelectronic devices have been explored in the hope of developing a communication wavelength silicon compatible technology that would be low cost [21]. The mismatch of lattice constants between germanium and silicon, however, has been

a challenge because the mismatch can make defects and degrade the performance of devices. Recently, low defect density germanium epitaxially deposited on silicon substrate has been achieved by a number of groups using graded buffer layer (Figure 1.3). Using these relaxed graded buffer layers, photodetectors for communication wavelength application were demonstrated [1].

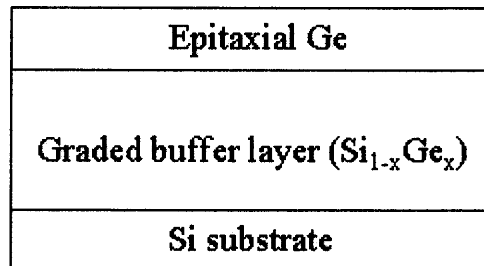

Figure 1.3 Schematic of epitaxial germanium growth on silicon substrate using graded buffer layer ($Si_{1-x}Ge_x$).

CHAPTER 2

REVIEW OF LITERATURE

2.1 Ion Stopping Theory

When an energetic ion moves through a solid, the kinetic energy of the ion is transferred to the lattice through the coulombic interaction in nuclear collisions with the lattice nuclei and with the electrons around the lattice atoms. The energy loss per unit length due to nuclear collisions is called the nuclear stopping power $S_n(E)$, and the electronic stopping power $S_e(E)$ for electrons. The total distance of ion traveled in target is the *range* (R); the penetration depth of the implanted ion along the implantation direction is known as the *projected range* (R_p), as in Figure 2.1.

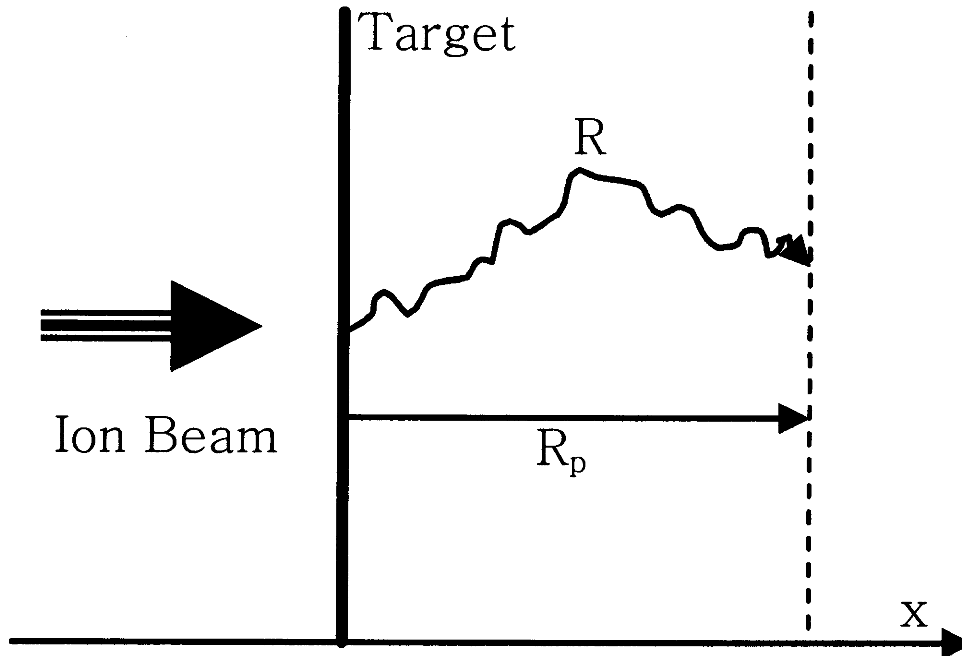

Figure 2.1 Description of the ion *range*, R, and *projected range*, R_p.

The loss rate of energy (*dE/dx*) can be expressed by Equation (2.1):

$$-\frac{dE}{dx} = N[S_n(E) + S_e(E)] \qquad (2.1)$$

where E is the energy of the ion at a point x along its path, and N is the atomic density. The negative sign means that the energy is decreased with depth due to the collision and the coulombic interaction. Thus, the total *range*, which ion travels, can be obtained by integrating Equation (2.1) with respect to energy, Equation (2.2) [13, 16, 22]:

$$R = \int_0^R dx = \frac{1}{N}\int_0^{E_0} \frac{dE}{S_n(E) + S_e(E)}. \qquad (2.2)$$

2.1.1 Stopping Powers based on LSS theory

As mentioned above, the total *range* is strongly related with the nuclear and electronic stopping power. Basically, nuclear stopping can be imagined by a collision between two atoms as shown in Figure 2.2 [23].

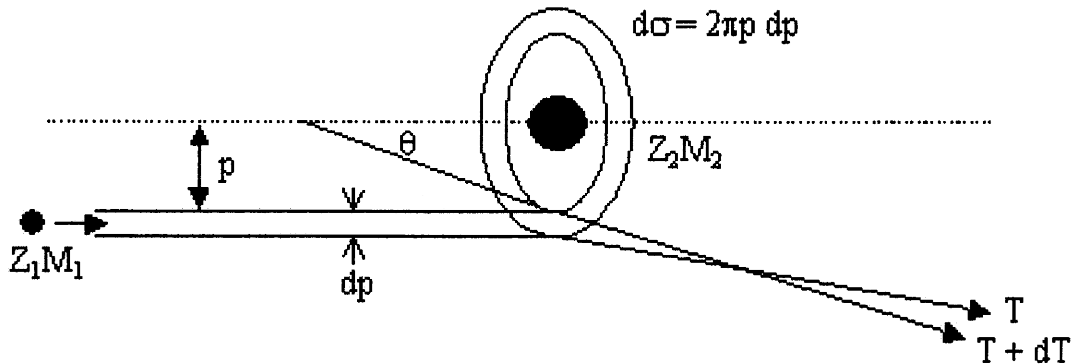

Figure 2.2 Schematic diagram before a collision between two atoms.

The nuclear stopping power can be obtained from a transferred energy (T) during a collision, considering the conservation of energy and momentum [23]:

$$NS_n = -\left(\frac{dE}{dx}\right)_{nuclear} = N\int_0^{T_{max}} T d\sigma\,, \tag{2.3}$$

$$T = \frac{4M_1 M_2 E}{(M_1 + M_2)^2}\sin^2\frac{\theta_c}{2} \tag{2.4}$$

where M_1 and M_2 are the masses of the projectile and the target atom, respectively. In Equation (2.3), $d\sigma$ is the differential cross section, which is equal to $2\pi p dp$. Here, p is the impact parameter. In Equation (2.4), θ_c is the scattering angle in Figure 2.3, which is defined by Equation (2.5) [22, 24].

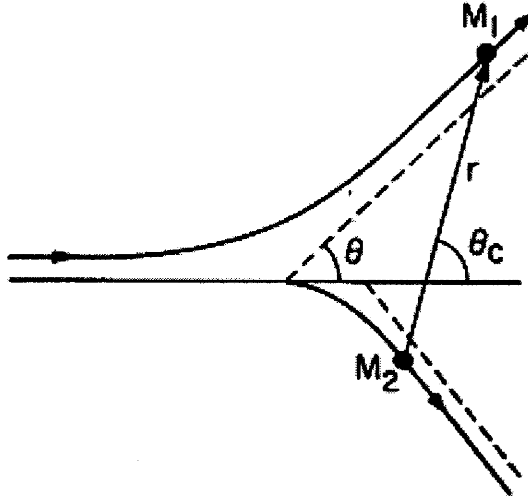

Figure 2.3 Schematic diagram after a collision between two atoms.

$$\theta_c = \pi - 2p \int_{r_{\min}}^{\infty} \frac{dr / r^2}{\sqrt{1-(V(r)/E_r)-(p/r)^2}} \qquad (2.5)$$

where p is the impact parameter, r_{min} the minimum distance of approach, and E_r the energy in the center of mass system equal to $(M_2E)/(M_1+M_2)$. V(r) is the interatomic potential function with a screening function:

$$V(r) = \frac{Z_1 Z_2 q^2}{4\pi\varepsilon_0 r} f(r/a) \qquad (2.6)$$

where Z_1 and Z_2 are the atomic number of the projectile and target atom. In LSS theory, two screening functions are used [22]:

$$f(r/a) = \frac{a}{r}, \qquad (2.7)$$

$$f(r/a) = \left\{ \frac{(r/a)}{\sqrt{(r/a)^2 + C^2}} \right\}, \qquad (2.8)$$

$$a = 0.885 a_0 (Z_1^{2/3} + Z_2^{2/3})^{-1/2}, \qquad (2.9)$$

where a is the screening parameter given by the Thomas-Fermi value, a_0 is the Bohr radius (= 0.529 Å), and C is the fitting constant ($\sim\sqrt{3}$). If Equation (2.7) is chosen for calculation, the standard stopping power (S_n^0) is obtained [22].

$$NS_n(E) = -\left(\frac{dE}{dx}\right)_{nuclear} \cong NS_n^0, \qquad (2.10)$$

$$S_n^0 = 2.8\times10^{-15} \frac{Z_1 Z_2}{(Z)^{1/3}} \frac{M_1}{M_1+M_2} [\mathrm{eV}\cdot cm^2], \qquad (2.11)$$

$$Z^{1/3} = (Z_1^{2/3} + Z_2^{2/3})^{1/2}. \qquad (2.12)$$

The electronic stopping power (S_e) can be treated as a projectile in a viscous medium such as a free electron gas, which can be defined by [13]:

$$NS_e(E) = \left(\frac{dE}{dx}\right)_{electron} = C_{NSE}E^p, \tag{2.13}$$

where C_{NSE} is electronic stopping constant (keV^{1-p}/micron), and p varies from 0.4 to 0.58. For light ions from boron to neon, an empirical formula, presented by Northcliffe and Schilling, can be used:

$$S_e^*(E) = \frac{S_e(E)}{1+[E/E_{NS}]}, \tag{2.14}$$

where E_{NS} is the Northcliffe constant. The following table shows some defined constants for boron or phosphorus in germanium [13], and the calculated energy losses, NS(E), are shown in Figure 2.4 (a) and (b) for boron and phosphorus implant into germanium and silicon, respectively.

Table 2.1 Constants for Boron or Phosphorus in Germanium

	NS_n^0 (keV/μm)	C_{NSE} (keV^{1-p}/μm)	p	E_{NS} (keV)
Boron	0.7031×10^2	0.2299×10^2	1/2	0.286×10^4
Phosphorus	0.4365×10^3	0.3532×10^2	1/2	N/A

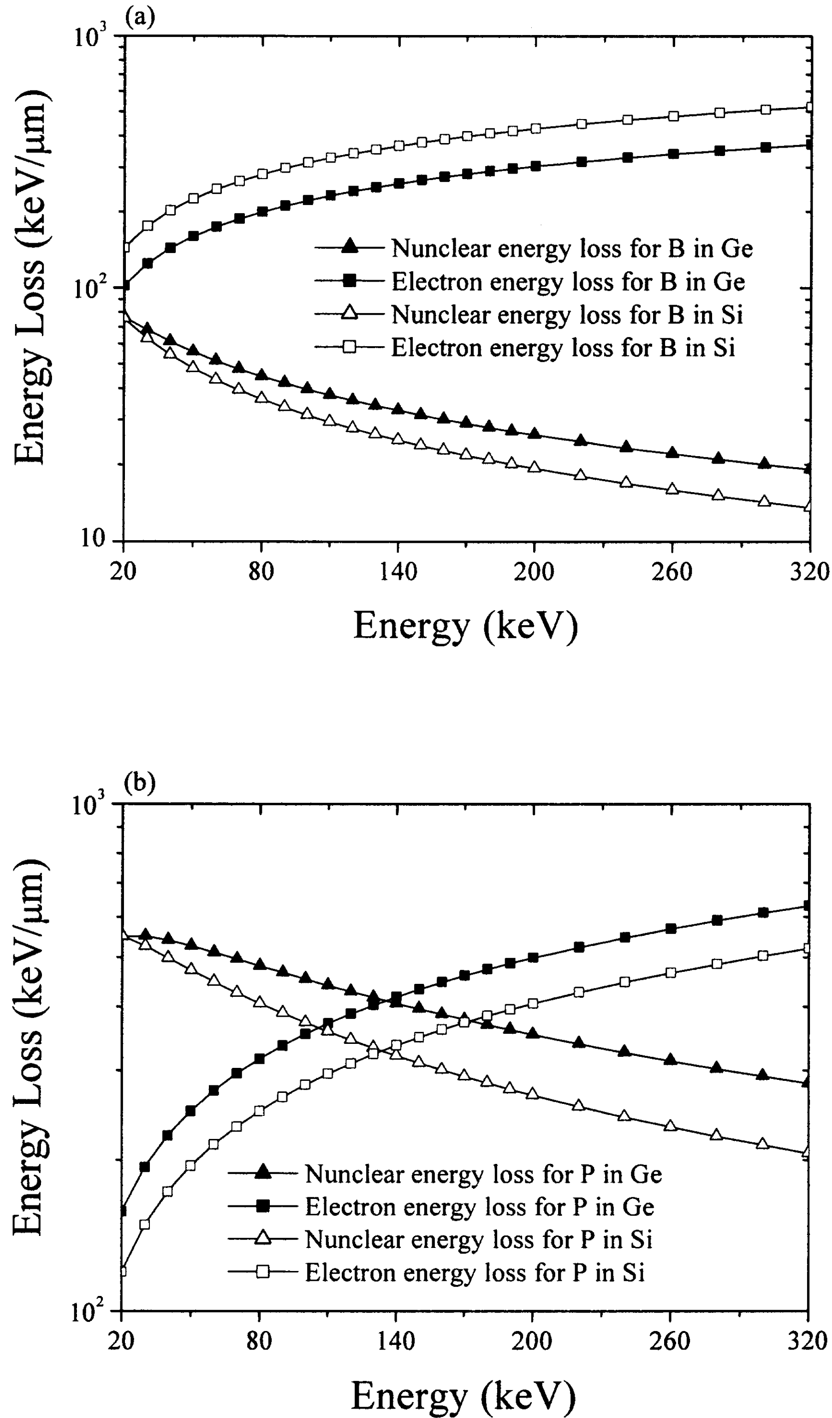

Figure 2.4 Nuclear and electronic energy loss vs. energies for (a) boron and (b) phosphorus in germanium and silicon, calculated from LSS theory.

Due to the collision between the projectiles and the target, the trajectory is not a straight line, as shown in Figure 2.1. Thus, a second parameter called the *projected range*, R_p, is approximately given by [25]:

$$R_p = \frac{R}{1+\left[M_2/(3M_1)\right]}. \tag{2.15}$$

Gibbons et al. calculated the nuclear and electronic stopping power as well as the *projected range* and straggle using the above calculations and experimental corrections [13]. In this study, these calculated values were used to better understand the phenomenon of ion implantation and compare with our experimental data.

2.1.2 Monte-Carlo based SRIM

SRIM [26] based on Monte-Carlo calculation, which is abbreviated from the Stopping and Range of Ion in Matter, is a free program to simulate the implanted profiles. However, the limitation of this program is that the target material is assumed as amorphous, which results in the inability to predict the "channeling effects," usually observed in implantation into the crystalline. In spite of this limitation, it is useful in distinguishing which component of the resulting implant profiles were due to channeling in this study.

The basic idea of Monte-Carlo calculation is the simulation of the history of a projectile through its successive collisions with target atoms [27]. The result is based upon the summation of these scattering events occurring along a large number of simulated particle trajectories within the target. The particle, which is initially possessed of a given energy, position, and direction, is assumed to change direction due to binary nuclear collisions and to move in straight paths between collisions.

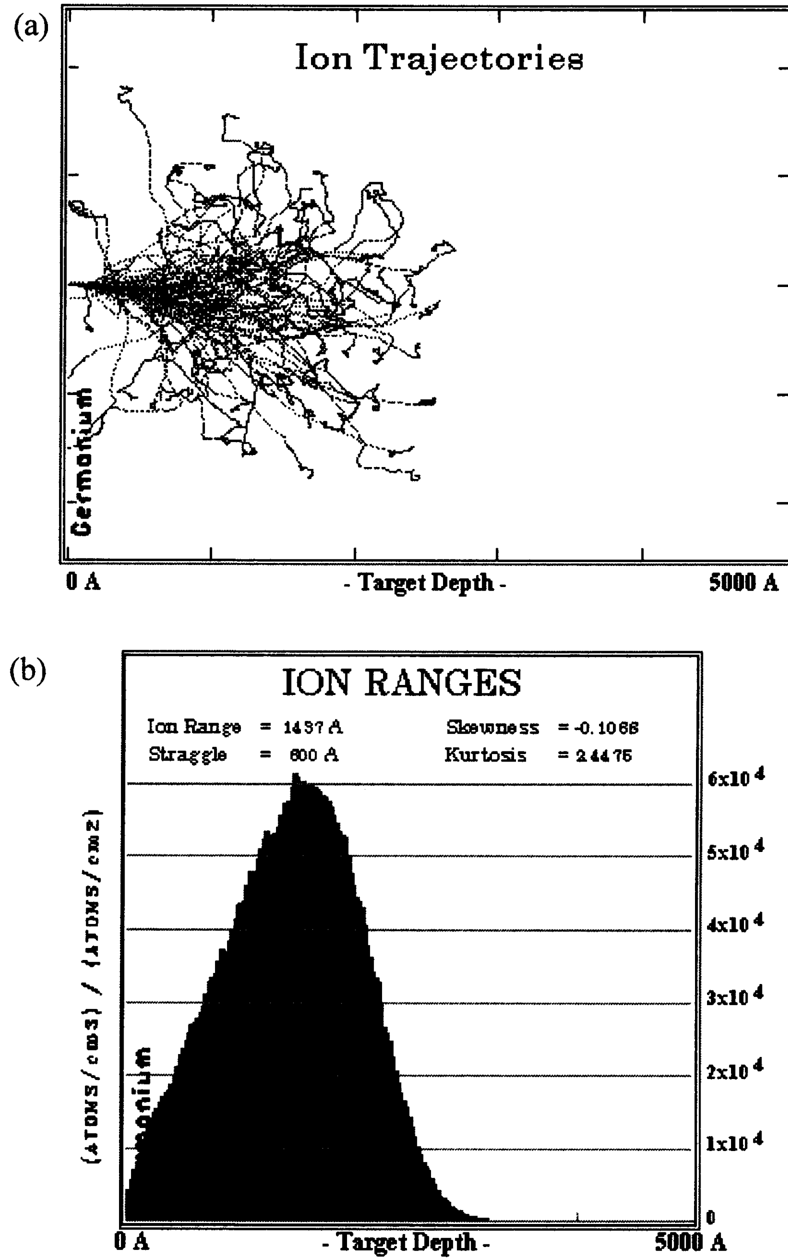

Figure 2.5 SRIM simulation: (a) ion trajectories of 180 boron ions (b) ion ranges of 99,999 boron ions implanted into amorphous germanium at 60 keV.

Figure 2.5 shows a two-dimensional scatter plot for the simulation of 180 boron ions implanted into germanium at 60 keV and the projectile distribution after 99,999 counts with 7° tilt. The implanted ions come to rest as a result of nuclear and electronic energy loss as mentioned in previous section. However, the screening function of interatomic potential used in LSS theory is not accurate at low energies, Figure 2.6 [28]. Thus, due to the unrealistic long tail of charge of the Thomas-Fermi adopted potential, the resulted *projected ranges* would be deviated at the lowest energies. Instead of Thomas-Fermi potential, the simulations in this work use universal screening potential defined as:

$$\Phi(x) = 0.1818e^{-3.2x} + 0.5099e^{-0.9432x} + 0.2802e^{-0.4028x} + 0.02817e^{-0.2016x} \qquad (2.16)$$

where x is (r/a), and a is defined by Equation (2.9).

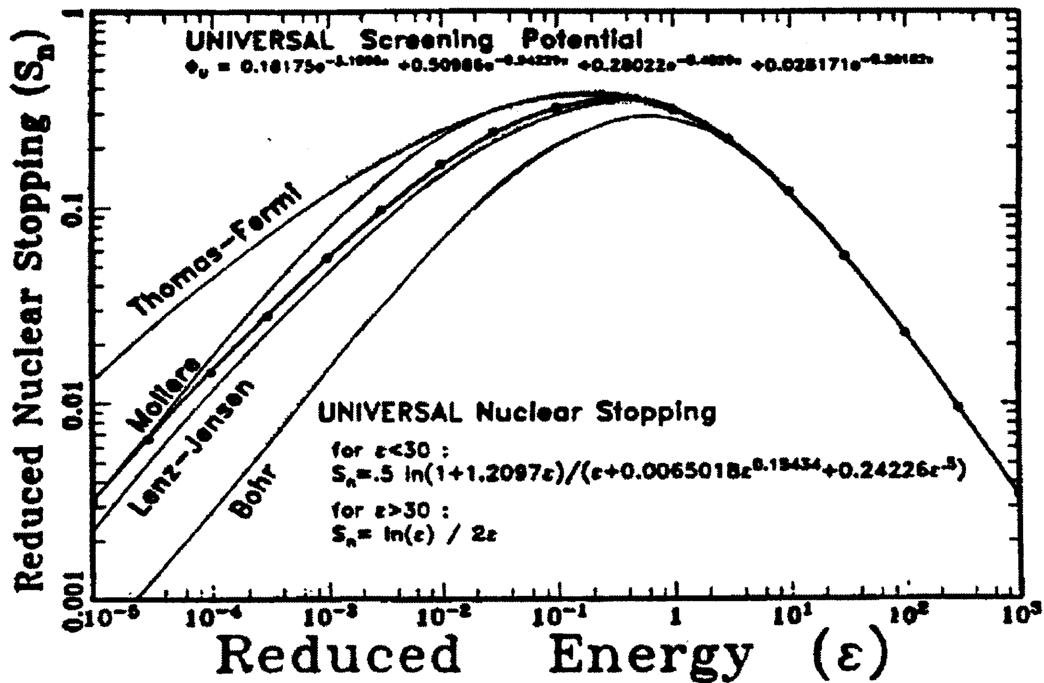

Figure 2.6 Effect of the adopted potential for nuclear stopping power [28].

The nuclear stopping power using Equation (2.16) is shown in Equation (2.17). The reduced energy and nuclear stopping power are also shown in Equation (2.18) and (2.19) [28]:

$$S_n(E) = \frac{8.462\times10^{-15} Z_1 Z_2 M_1 S_n(\varepsilon)}{(M_1+M_2)(Z_1^{0.23}+Z_2^{0.23})} \quad [\text{eV}\cdot cm^2], \tag{2.17}$$

$$\varepsilon = \frac{32.53 M_2 E}{Z_1 Z_2 (M_1+M_2)(Z_1^{0.23}+Z_2^{0.23})}, \tag{2.18}$$

ε is the reduced energy

$$\begin{aligned} &\text{For } \varepsilon \le 30: S_n(\varepsilon) = \frac{\ln(1+1.1383\varepsilon)}{2[\varepsilon + 0.01321\varepsilon^{0.21226} + 0.19593\varepsilon^{0.5}]} \\ &\text{For } \varepsilon > 30: S_n(\varepsilon) = \frac{\ln(\varepsilon)}{2\varepsilon} \end{aligned} . \tag{2.19}$$

In the case of 140 keV boron implant into germanium, the reduced energy is 6.74, and 3.72 for 320 keV phosphorus implant into germanium. Thus, the energy loss (NS_n) of LSS theory is 16% greater than that calculated from Equation (2.17) for 60 keV phosphorus implant into germanium. This difference is reduced as the energy increases.

The damage induced implantation can be roughly predicted from the SRIM simulation. Figure 2.7 shows the result of simulation for the collision events. From the simulation, the amorphization of germanium would be expected for 5×10^{16} cm^{-2} boron (at 60 keV), and 1×10^{15} cm^{-2} and 5×10^{16} cm^{-2} phosphorus (at 170 keV). In this study, all simulations were carried out using 99,999 counts and a 7° tilt with the assumption of amorphous germanium.

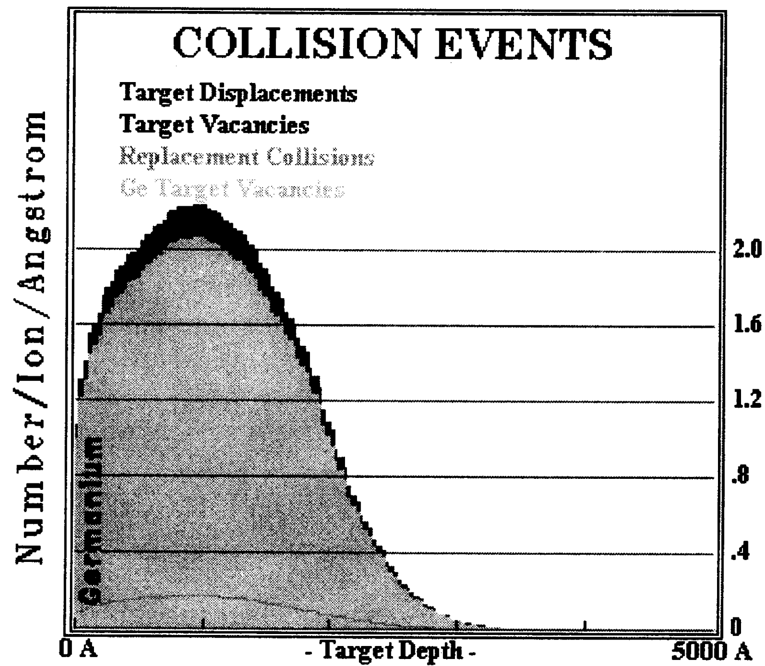

Figure 2.7 SRIM simulation of the collision events for phosphorus implant into germanium at 170 keV, which was carried out 99,999 counts.

2.2 Channeling

Channeling describes the phenomena of implanted ions passing relatively unimpeded in particular crystal directions for which the atoms of the lattice form "channels," see Figure 2.8. In standard device fabrication, channeling is considered undesirable because it tends to increase the junction depth. Shallow junction depths currently represent an increasingly challenging hurdle to future scaling of MOSFETs.

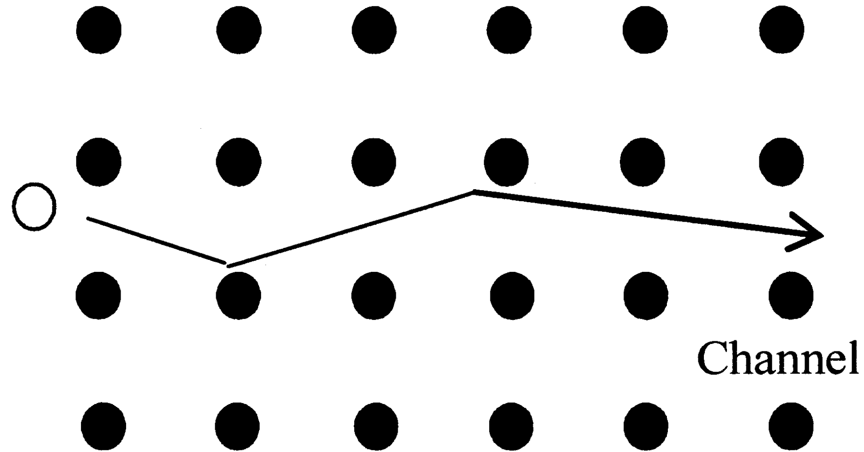

Figure 2.8 Schematic illustration of channeling.

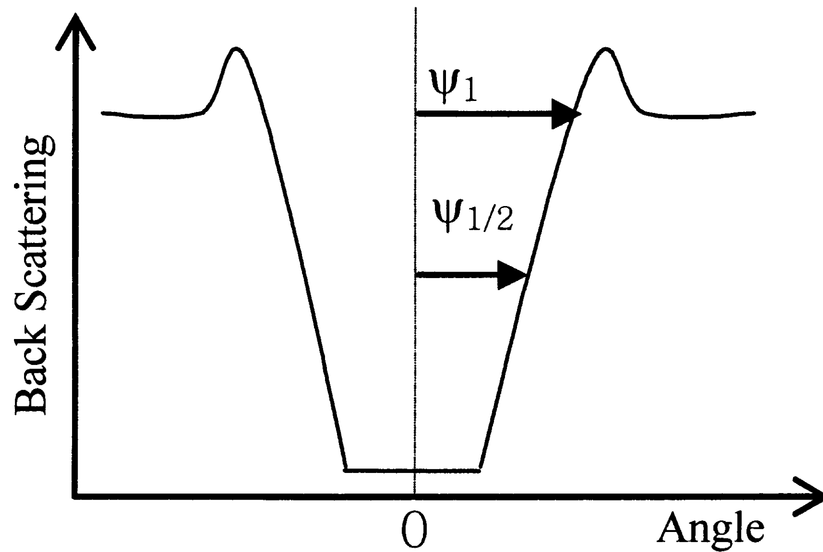

Figure 2.9 Back-scattering yield around a channeling direction. Yield is a minimum when beam is well aligned with a channel [23].

Channeling can be analytically characterized by a critical angle Ψ_1 that is maximum angle between ion and channel for a glancing collision to be possible, in Figure 2.9 [23, 29]:

$$\Psi_1 = 9.73\sqrt{\frac{Z_1 Z_2}{Ed}} \quad \text{(degrees)} \tag{2.20}$$

where d is the atomic spacing along the ion direction (Å), E is the ion energy (keV). A stable channeled trajectory requires multiple glancing collisions. The angular half-width $\Psi_{1/2}$ is given as [23, 29]:

$$\Psi_{1/2} = 7.57\sqrt{\frac{a}{d}\Psi_1} \quad \text{(degrees)} \tag{2.21}$$

where a is the screening length (see Equation (2.9)). Table 2.2 shows the critical angle and the angular half-width for silicon and germanium with selected energies. These calculations indicate an expected increase in the acceptance angle for channeling in the case of germanium compared to silicon for the same species and implant energies. The number of channeled dopant atoms is therefore expected to be greater in the case of germanium than silicon for the same implant conditions. It will be shown, however, that implant distributions into germanium typically show a less pronounced tail than in silicon. Finally, it is common to tilt the substrate by 7°, so that the lattice presents a denser orientation to the incident beam, for implantation into silicon and germanium to reduce the channeling effect.

Table 2.2 Calculation of ψ_1 and $\psi_{1/2}$ for Born and Phosphorus Implanted into Germanium and Silicon

Target	Dopant	Energy (keV)	ψ_1 (°)	$\psi_{1/2}$ (°)
Si	B	20	7.81	3.61
	B	60	4.51	2.74
	B	140	2.95	2.22
	P	60	7.81	3.35
	P	170	4.64	2.58
	P	320	3.38	2.20
Ge	B	20	11.57	3.90
	B	60	6.68	2.96
	B	140	4.37	2.40
	P	60	11.57	3.69
	P	170	6.87	2.84
	P	320	5.01	2.43

Figure 2.10 and 2.11 show three-dimension view along <100> germanium and tilted 7° with respect to <100> direction. Open channels offer ion implanted atoms a low scattering path, however, these are reduced when the crystal is tilted 7°.

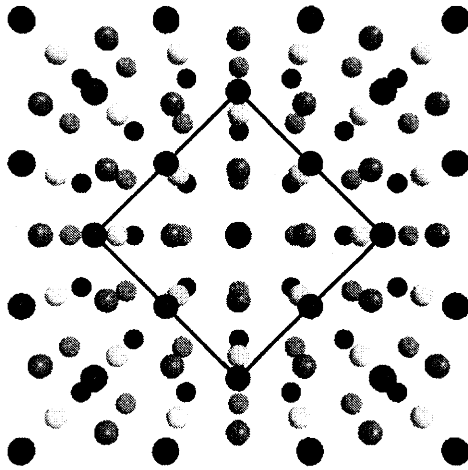

Figure 2.10 Model of germanium crystal seen along the <100> direction.

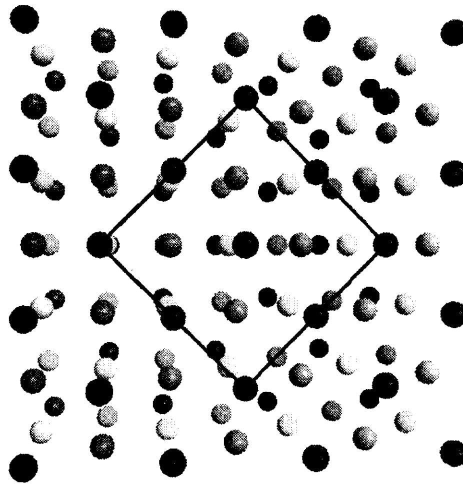

Figure 2.11 Model of germanium crystal tilted 7° with respect to <100> direction.

2.3 Analytical Modeling Method

The analytical method is basically an empirical method. There are several distribution functions to present the implanted profiles, such as the simple Gaussian, the joined half Gaussian, the Edgeworth distribution, the Pearson distributions, and so on. However, it is well known that Pearson distribution is easier and more accurate than others, especially channeling occurs during the implantation into crystal materials. Sometimes, for the purpose of a more accurate description in the tail region, the dual Pearson distribution can be used.

2.3.1 Distribution Functions

The Gaussian distribution is a first approximation, which is characterized by two moments: the *projected range* and the straggle. This distribution was used in LSS theory, and is symmetric so it does not satisfactorily fit experimental data, which are characterized by asymmetrical profiles even if the target is amorphous. Thus, to overcome the limitation of the Gaussian distribution, the modified distributions, such as the joined half Gaussian [30] and the Edgeworth distribution [31], were adopted. However, the joined half Gaussian use only three moments, and the Edgeworth distribution required the knowledge of higher-order moments. Thus, among the analytical modeling methods, the Pearson distribution is probably the best choice for more accuracy and convenience.

2.3.2 Pearson Distribution

One of the advantages of ion-implantation is that the distribution of implanted ions in the substrate can be modeled and predicted. In order to describe the implant profiles, the first four moments were calculated for both the boron and phosphorus SIMS profiles in germanium and silicon. The first four moments are commonly called the *projected range* (the first moment), straggle (the second moment), skewness (the third moment), and kurtosis (the fourth moment) [23]. The *projected range* can be explained as the average depth of the implanted ions. However, the *projected range* does not describe the shape of the profile. The straggle is the width of the distribution, and it indicates the statistical fluctuations of the depths of the implanted ions. The skewness measures the asymmetry of the distribution. For example, if the skewness is negative, the distribution falls off toward the surface more smoothly and decreases rapidly on the other side of the distribution peak. The opposite behavior occurs for a positive value. The kurtosis describes the extent of the tail for any distribution, and also indicates how flat the top of a distribution is. A distribution with a high value for kurtosis will be sharply peaked with a long exponential tail [23, 32]. Figure 2.12 shows graphically the effect of the skewness and kurtosis on the distribution.

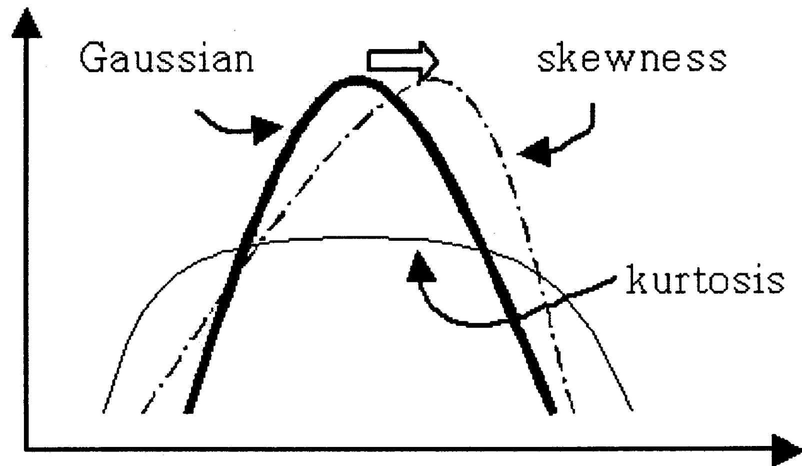

Figure 2.12 Schematic illustration of the skewness and kurtosis.

The *projected range*, R_p can be obtained from Equation (2.22), where x is the depth normal to the surface in unit of cm, and f(x) is the concentration of dopant at x in atoms/cm^3. The denominator of Equation (2.22) equals to the dose (ϕ) of the implanted ions in atoms/cm^2 [33]:

$$R_p = \frac{\int_{-\infty}^{\infty} x f(x) dx}{\int_{-\infty}^{\infty} f(x) dx}. \tag{2.22}$$

The second (σ_p), third (γ) and fourth (β) moments were calculated using Equations (2.23-25) [33]:

$$\sigma_p = \left[\frac{\int_{-\infty}^{\infty} (x - R_p)^2 f(x) dx}{\int_{-\infty}^{\infty} f(x) dx} \right]^{1/2}, \tag{2.23}$$

$$\gamma = \frac{\int_{-\infty}^{\infty}(x-R_p)^3 f(x)dx}{\sigma_p^3 \int_{-\infty}^{\infty} f(x)dx}, \tag{2.24}$$

$$\beta = \frac{\int_{-\infty}^{\infty}(x-R_p)^4 f(x)dx}{\sigma_p^4 \int_{-\infty}^{\infty} f(x)dx}. \tag{2.25}$$

The family of thirteen Pearson distributions (including the Gaussian distribution) is frequently used to fit and simulate dopant implants. The differential Equation, which describes the Pearson distribution, is [23]:

$$\frac{df(y)}{dy} = \frac{(y-a)f(y)}{(b_0 + b_1 y + b_2 y^2)}$$

$$\begin{aligned} &y = x - R_p, \qquad a = b_1 = -\gamma\sigma_p(\beta+3)C \\ &b_0 = -\sigma_p{}^2(4\beta - 3\gamma^2)C, \qquad b_2 = -(2\beta - 3\gamma^2 - 6)C \\ &C = [2(5\beta - 6\gamma^2 - 9)]^{-1} \end{aligned} \tag{2.26}$$

The different Pearson types (from I to XII and Gaussian) is due to the nature of the roots of the Equation, $b_0 + b_1y + b_2y^2 = 0$. For example, common distributions are described by the following: Gaussian ($b_1 = b_2 = 0$) and Pearson IV ($0 < b_1^2/4b_0b_2 < 1$). The typical conditions for determination of Pearson distribution type are shown in Table 2.3. The resulting expression for Pearson I, IV and VI are the following Equations (2.27-29) [33]:

Table 2.3 The Different Pearson Types and Gaussian Distribution with Conditions

Type	Condition
Gaussian	$\gamma = 0,\ \beta = 3$
Pearson type I	$\gamma \neq 0,\ (\gamma^2+1) \leq \beta < [3+(3/2)\gamma^2],\ \lambda \neq 0\ C \neq \infty$
Pearson type IV	$0 < \gamma^2 < 32,\ \beta > [39\gamma^2+48+6(\gamma^2+4)^{3/2}]/(32-\gamma^2)$
Pearson type VI	$\gamma \neq 0,\ (3+(3/2)\gamma^2) < \beta < [39\gamma^2+48+6(\gamma^2+4)^{3/2}]/(32-\gamma^2),\ \lambda \neq 0$

Note: $\lambda = \gamma^2(\beta+3)^2(8\beta-9\gamma^2-12)-4(4\beta-3\gamma^2)(5\beta-6\gamma^2-9)^2$

Type I

$$f(x) = K\left(x - R_p + A_1\right)^{m_1}\left(A_2 + R_p - x\right)^{m_2}$$

here, K is a normalization constant,

$$(m_1+1)A_2 = (m_2+1)A_1, \quad A_2 \geq (x - R_p) \geq -A_1,$$

$$m_1 = \frac{(A_1+b_1)}{b_2(A_1+A_2)}, \quad m_2 = \frac{(A_2-b_1)}{b_2(A_1+A_2)},$$

$$A_1 = \frac{1}{2}\left\{\frac{b_1}{b_2} + \sqrt{\left(\frac{b_1}{b_2}\right)^2 - \frac{4b_0}{b_2}}\right\}, \text{ and } A_2 = -\frac{1}{2}\left\{\frac{b_1}{b_2} - \sqrt{\left(\frac{b_1}{b_2}\right)^2 - \frac{4b_0}{b_2}}\right\} \qquad (2.27)$$

or

$$A_1 = \frac{1}{2}\left\{\frac{b_1}{b_2} - \sqrt{\left(\frac{b_1}{b_2}\right)^2 - \frac{4b_0}{b_2}}\right\}, \text{ and } A_2 = -\frac{1}{2}\left\{\frac{b_1}{b_2} + \sqrt{\left(\frac{b_1}{b_2}\right)^2 - \frac{4b_0}{b_2}}\right\}$$

A_1 and A_2 are both positive.

Type IV

$$f(x) = K\left[1+\left(\frac{(x-R_p)}{A}-\frac{n}{r}\right)^2\right]^{-m}\exp\left[-n\arctan\left(\frac{(x-R_p)}{A}-\frac{n}{r}\right)\right]$$

$$r = 2(m-1) = -\left(2+\frac{1}{b_2}\right), \tag{2.28}$$

$$n = -\frac{rb_1}{\sqrt{4b_0b_2-b_1^2}}, \quad m = -\frac{1}{2b_2}, \quad A = \frac{mrb_1}{n}.$$

Type VI

$$f(x) = K\left(1+\frac{(x-R_p)}{A_1}\right)^{-q_1}\left(1+\frac{(x-R_p)}{A_2}\right)^{q_2}$$

$$(q_1-1)A_2 = (q_2+1)A_1, \text{ and } 1+\frac{(x-R_p)}{A_2} \geq 0 \tag{2.29}$$

$$q_1 = -\frac{(A_1+b_1)}{b_2(A_1-A_2)}, \quad q_2 = -\frac{(A_2+b_1)}{b_2(A_1-A_2)}$$

$$A_1 = \frac{1}{2}\left[\frac{b_1}{b_2}+\sqrt{\left(\frac{b_1}{b_2}\right)^2-\frac{4b_0}{b_2}}\right], \quad A_2 = \frac{1}{2}\left[\frac{b_1}{b_2}-\sqrt{\left(\frac{b_1}{b_2}\right)^2-\frac{4b_0}{b_2}}\right].$$

The program for the calculation of the first four moments and the determination of the Pearson types using Mathematica software is shown in Appendix.

CHAPTER 3

EXPERIMENTAL METHODOLOGY

3.1 Description of Samples

In experiments, n- and p-type (100) germanium, and n- and p-type (100) silicon wafers were used as substrates. The n-type germanium was nominally doped with 2×10^{16} cm^{-3} antimony (Sb) (0.04-0.4 ohm-cm), and the p-type germanium substrate was nominally doped with 1×10^{18} cm^{-3} Gallium (Ga) (0.005-30.0 ohm-cm), see Table 3.1. All germanium wafers were single sided chemomechanically polished, and had dislocation densities that were less than 5000 cm^{-2}.

Table 3.1 Certified Test Data of Germanium and Silicon Wafers

	Germanium (Ge)		Silicon (Si)	
	n-type	p-type	n-type	p-type
Resistivity (ohm-cm)	0.04 ~ 0.4	0.005 ~ 30.0	48.0 ~ 67.0	9.5 ~ 15
Orientation	(100) ± 1°	(100) ± 1°	(100)	(100) ± 0.5°
Thickness (μm)	360 ± 38	360 ± 51	525.0 ± 25.0	380 ± 50
Diameter (mm)	50	50	100	50

3.2 Process of Ion Implantation

Ion Implantation is a common method for doping semiconductors. The most important advantages over more simple techniques such as driven-in diffusion are (1) the ability to introduce nearly any kind dopant into the substrate with precise control of the dopant location, and (2) the ability to model and therefore predict the dopant location as well as the distribution. The implanted dose (ϕ in cm^{-2}) is precisely controlled by beam current (I in ampere), and implantation duration (t in second):

$$\phi = \frac{It}{qA}, \tag{3.1}$$

where A is the area of target in cm^2, and q is the charge per ion (= 1.602×10^{-19} C) [16].

In this study, germanium and silicon substrates were implanted with $^{31}P^+$ or $^{11}B^+$, while tilted 7° away from the beam axis, which was expected to reduce channeling. In this condition, the crystal surface seems to be much more densely packed with atoms and the channels are much less pronounced [22], as shown in Figure 2.10 and 2.11. The ion source gases were PF_5 or BF_3 for $^{31}P^+$ or $^{11}B^+$, respectively, and VARIAN CF4 or VARIAN A2F-200 was used for phosphorus or boron ion implant, respectively. Implant energies for boron or phosphorus ranged from 20 to 320 keV. Ion doses ranged from 5×10^{13} to 5×10^{16} cm^{-2} for both boron and phosphorus, as listed in Table 3.2.

Table 3.2 Conditions of Ion Implantation into (100) Germanium and Silicon wafers

Substrate	Dopant	Energy (keV)	Dose (cm^{-2})	Beam current density ($\mu A/cm^2$)
Ge, Si (n-type)	B	20	5×10^{13}	0.04
		60	5×10^{13}	0.06
		60	1×10^{15}	1.33
		60	5×10^{16}	1.74
		140	5×10^{13}	0.08
Ge, Si (p-type)	P	60	5×10^{13}	0.07
		170	5×10^{13}	0.10
		170	1×10^{15}	1.20
		170	5×10^{16}	2.00
		320	5×10^{13}	0.10

3.3 Process of Activation Annealing

After ion implantation, dopant annealing is necessary for the electrical activation of the implanted ions. To examine the dopant activation in germanium, the samples were subsequently cleaved and annealed for 3 hours at either 400, 600 or 800°C in ultra high purity N_2 (O_2 < 2ppm and H_2O < 1ppm). As shown in Figure 3.1, the annealing system consists of three main parts: gas delivery, furnace and exhaust system. In gas delivery system, conventional mass flow controllers were used to monitor and control a 100 sccm flow rate of nitrogen. A MKS Baratron gauge with a 1000 Torr range was used to monitor the pressure in the chamber. The chamber is made of a fused quartz tube, and

inserted into a Lindbergh three-zone furnace with operation temperatures up to 1200°C. Plantinel II thermocouples (type F) were connected to the furnace, and were used to sense and control the temperature. The chamber was sealed at both openings by end caps and O-rings. Water was allowed to circulate around the end caps to keep avoiding thermal expansion of the O-rings, which can cause leakage in the system. The pressure was kept constant by a control valve.

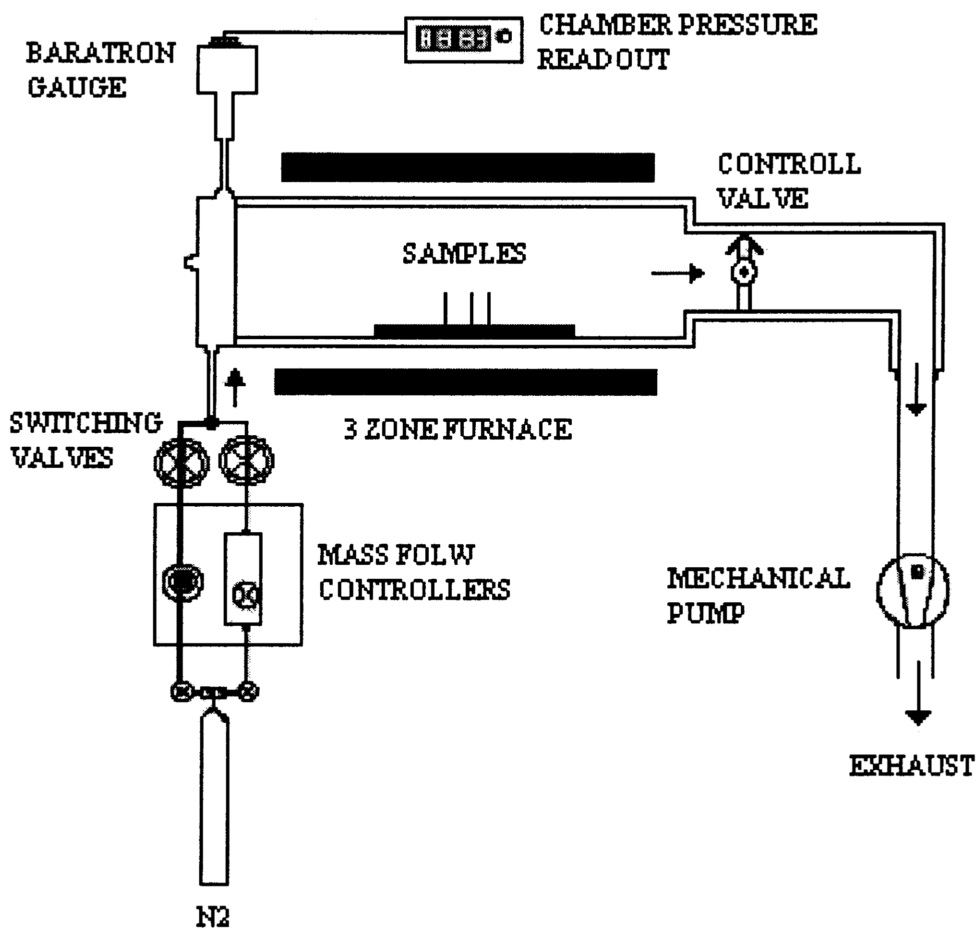

Figure 3.1 Schematic of the annealing system.

The calibration of flow rate and temperature were carried out before annealing process. The readout on the mass flow controller needs to be calibrated before experiment. The following Equation (3.2) shows how to calculate the flow rate in sccm:

$$\frac{dV}{dt} = \left(\frac{V_r}{760}\right) \times \left(\frac{273}{T}\right) \times \left(\frac{dP}{dt}\right), \tag{3.2}$$

where dV/dt is the flow rate of gas in sccm, V_r is the volume of the chamber ($\sim 1.8\times10^4$ cm^3), T is the measured chamber temperature in Kelvin, and dP/dt is the rate of pressure increase. For measurement of the rate of pressure increase, first, the chamber was evacuated for several hours. Then, N_2 gas is allowed to flow in the chamber. When the pressure is stable, the outlet valve of the chamber was closed, and the pressure change with time was measured.

The thermocouple was positioned outside of chamber, so it is important to measure the difference of temperatures between outside and inside chamber. The temperature is controlled by manual settings of the oven controls. The K-type thermocouple was inserted in the desired position, on which the sample should be placed. The temperature inside the chamber was then measured under the nitrogen flow.

Annealing at a higher temperature to improve dopant activation, 800°C for 3 hours, resulted in substantial roughening of the surface, perhaps due to the evaporation of germanium [34]. In Figure 3.2, the degradation of the surface is shown as viewed with a microscope after 800°C annealing. The surface after 600°C annealing is also shown.

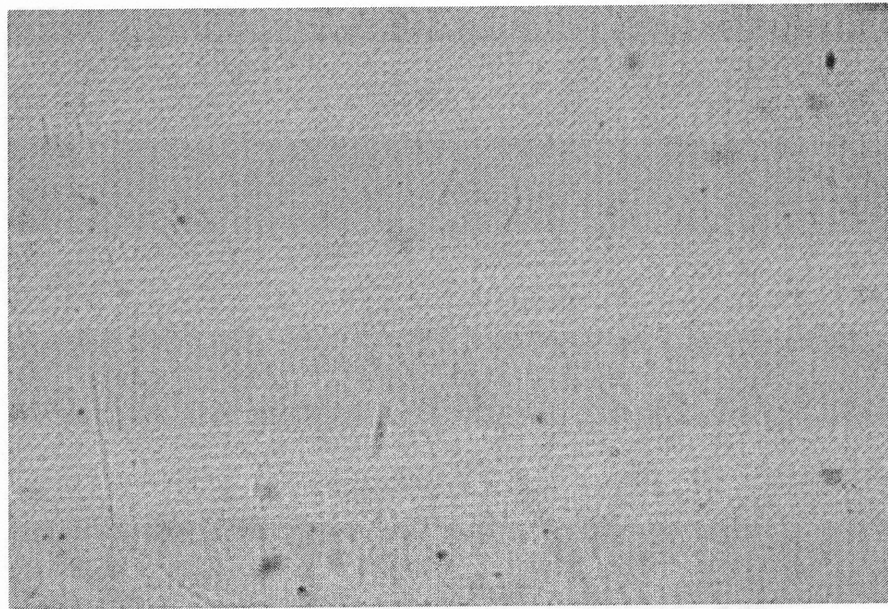

(a)

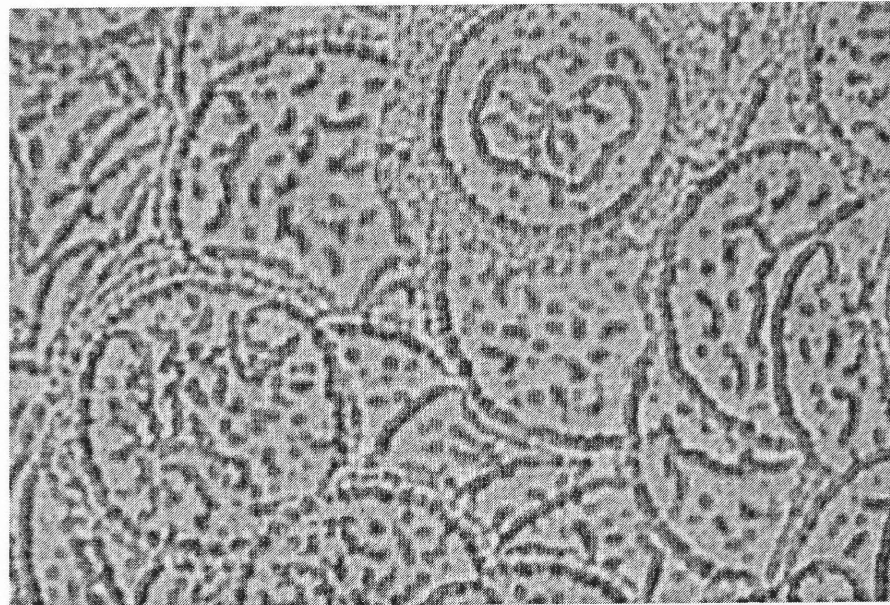

(b)

Figure 3.2 Effect of annealing at high temperature: 60 keV, 1×10^{15} cm^{-2} boron implantation into germanium with annealing temperature of (a) 600°C and (b) 800°C for 3 hours in N_2 (60×10 magnification).

CHAPTER 4

CHARACTERIZATION METHODS

4.1 Secondary Ion Mass Spectrometry (SIMS)

Secondary ion mass spectrometry (SIMS) is a very powerful analytical technique for the characterization of surface and near surface chemical profiles, and it is ideal for characterization of dopants in semiconductor materials. A beam of energetic primary ions impinges onto the sample surface, and the ions in the sample surface are sputtered off. The ions that are sputtered off are called secondary ions, and these ions are detected by a mass spectrometer, Figure 4.1.

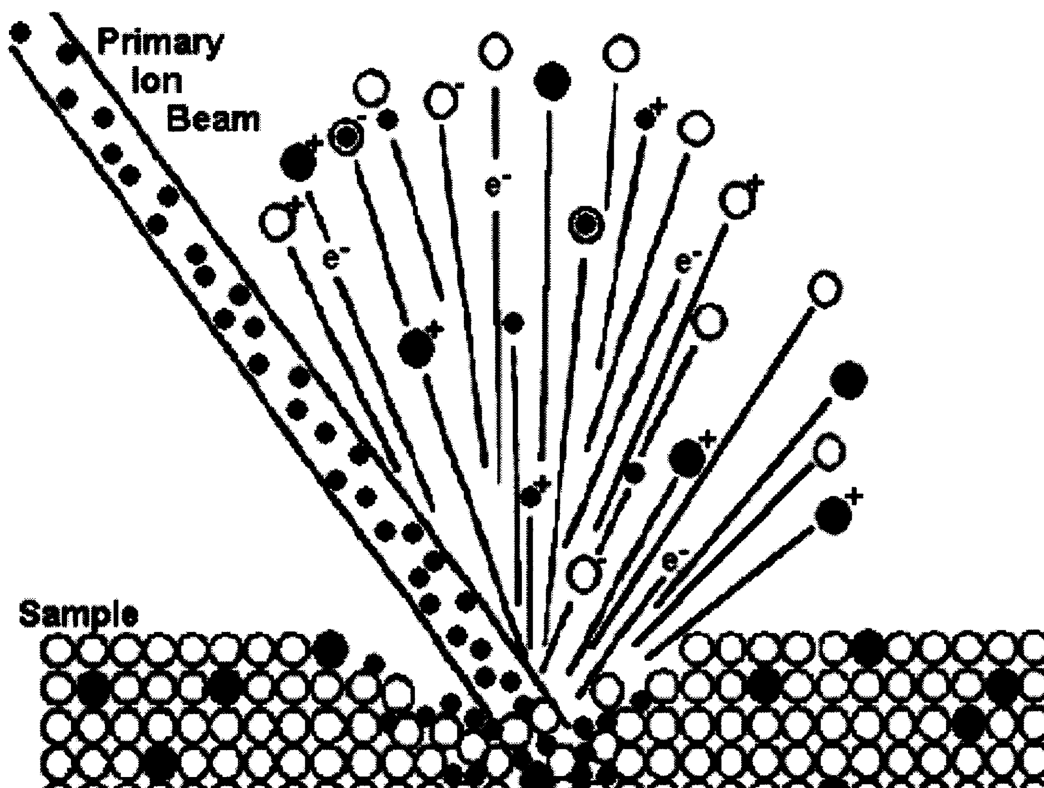

Figure 4.1 Schematic diagram of the sputtering process [35].

The primary beam can be O_2^+, Cs^+, Ga^+, and so on. O_2^+ is typically used for the detection of electropositive species, Cs^+ for electronegative, and Ga^+ for improved lateral resolution. In this study, after implantation, substrates were cleaved into samples and each sample was measured using SIMS, which was performed with a PHI Quadrupole SIMS instrument using a primary beam with 3.0 keV O_2^+ or 4.0 keV Cs^+ for boron or phosphorus, respectively, in Table 4.1. Quantitative data were obtained by counting the number of secondary ions of a given species as a function of sputter time. Then, the crater depth was measured using standard profilometry. The concentration as a function of depth was then determined using sputter rate for translating time to depth. Typically a calibration factor called the relative sensitivity factor (*RSF*) is used to translate ion count to concentration [36]:

$$C_i = (RSF)[I_i / I_m] \tag{4.1}$$

where C_i is the concentration of the impurity, and *RSF* is the relative sensitivity factor, which is a function of the impurity of interest and the sample matrix. I is the secondary ion intensity for impurity (i) or matrix (m), respectively.

Table 4.1 Instrument Conditions and Detection Limits for the Analyses

	B in Si	P in Si	B in Ge	P in Ge
Primary Ion Species	O_2^+	Cs^+	O_2^+	Cs^+
Primary Ion Energy (keV)	3.0	4.0	3.0	4.0
Primary Ion Angle of Incidence	60°	60°	60°	60°
Secondary Ion Polarity	Positive	Negative	Positive	Negative
Detection Limit (atoms/cm^3)	5×10^{14}	2×10^{15}	1×10^{15}	1×10^{15}

The accuracy of the depth calibration should be within ±3%, and the concentration accuracy depends on the accuracy of the reference material estimated to be within approximately 20-30% in all samples, unless otherwise noted. The detection limit is the lowest concentration that can be measured for a given element, which is commonly limited by either the ion yield from the sputtering process or non-intentional deposition of trace species in the vacuum chamber during the sputtering process. Detection limits can vary depending on many parameters including matrix, element and sputtering species. The detection limit of this study for both species in germanium was approximately 1×10^{15} cm^{-3} as shown in Table 4.1.

In general, *RSF* is a constant as long as the element is present as a dilute solute in the matrix. However, the dependence of ion count on concentration is known to become nonlinear in some cases when the concentration approaches atomic densities (e.g. ~ 5×10^{20} cm^{-3}) [37]. The concentration dependence and accuracy of the SIMS *RSF*s were, therefore, examined by comparing measured doses in silicon reference substrates with that found in the germanium substrates for both species. In the case of the highest boron dose implants, the total implanted dose detected by SIMS in the germanium was over twofold greater than in the silicon reference wafers (see Table 5.1). *RSF*s are relatively well established for silicon; however, those for germanium are not. Because the doses measured by SIMS in silicon matched those expected from the implant conditions but disagreed with those measured in the germanium at high dose, the germanium profile at high concentration is suspect. The uncertainty in the high boron dose implant case into germanium (i.e. in the case of 5×10^{16} cm^{-2}) is suspect and is therefore believed to far exceed that of the previously estimated 20% uncertainty.

The discrepancy of the measured doses in all other germanium cases was, however, within ±21% of that measured in the silicon for the same implant conditions. This is in good agreement with the previous estimate of the *RSF* uncertainty.

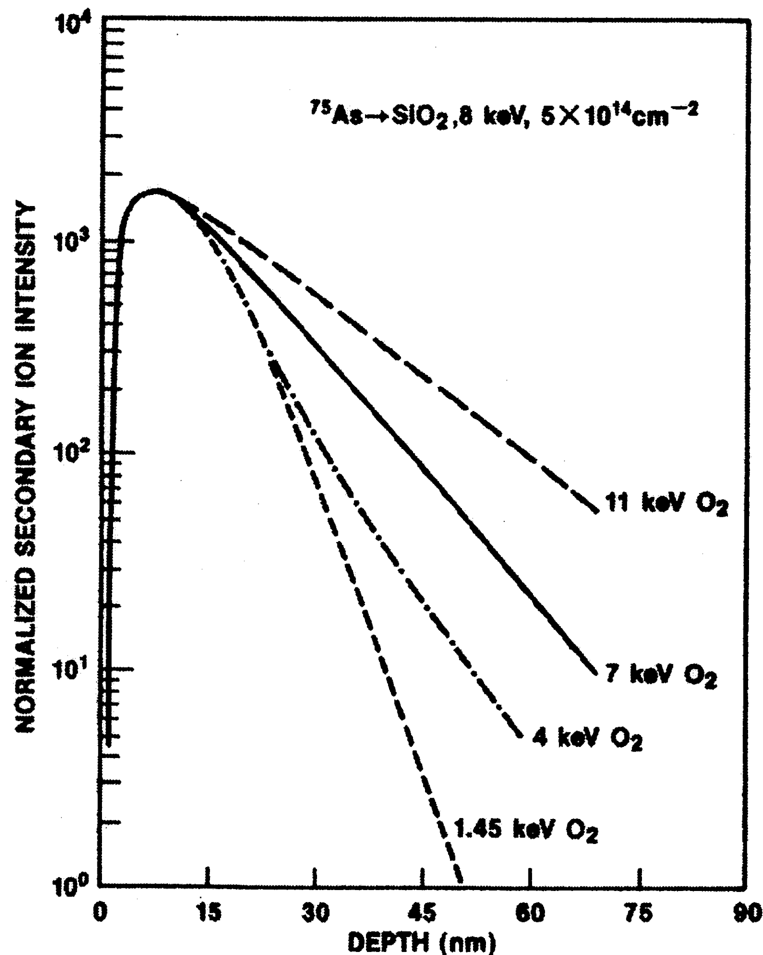

Figure 4.2 Example of "knock-on" effect with primary ion beam energies [36].

Another common difficulty with SIMS profiles in new materials, for which the SIMS sputtering parameters are not well characterized, are artifacts in the trailing edge due to affects like "knock-on," as shown in Figure 4.2 [23, 36]. Profile artifacts in SIMS usually result in a limited slope of the trailing edge. This effect produces

a measured dopant profile that extends much deeper into the substrate than is actually there. Spreading resistance profiles and SIMS of annealed implant profiles show good agreement between the locations of the measured junctions and the SIMS profiles (see Figure 5.14 and 5.16). Furthermore, a trailing edge slope of ~ 25 nm/decade of phosphorus was measured at concentrations as low as 1×10^{17} cm^{-3} using the same SIMS conditions as that used in this work, indicating that the SIMS conditions can resolve much steeper phosphorus falling edges than are observed in the as-implanted samples presented in this work. These combined observations indicate that the SIMS profiles presented in this work do not suffer from grossly exaggerated trailing edges due to SIMS artifacts like the "knock-on effect."

4.2 Spreading Resistance Profiling (SRP)

Spreading resistance profiling (SRP), which was proposed by Mazur and Dickey [38], is normally used to determine active doping profiles in semiconductor materials. Two-probe methods are usually used. This approach uses two probes that make direct contact, and are moved along a polished bevel as gentle as possible. A known current (I) is applied between the probes, and the voltage drop (V) is measured across these probes to get a spreading resistance (R_{SR}) defined by Ohm's Law (R_{SR} = V/I) [16]. Figure 4.3 shows the schematic diagram of spreading resistance profiling for the two-probe method.

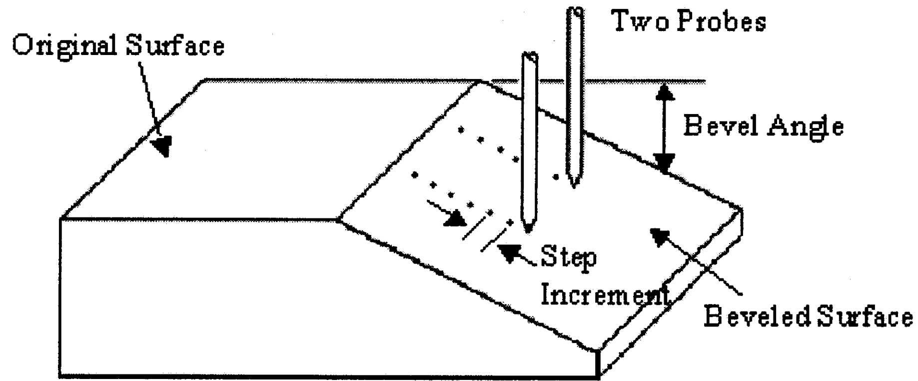

Figure 4.3 Schematic diagram of spreading resistance profiling.

The spreading resistance can be converted to the resistivity (ρ) by the following Equation for the two-point probe system:

$$\rho = R_{SR}(2a), \tag{4.2}$$

where a is an empirical quantity which is related to the effective electrical contact radius. The depth scale is obtained by using bevel angle and step increment. To quantify the efficiency of dopants to produce free carriers, the resistivity vs. depth profile is converted to the active carrier concentration vs. depth. The resistivity can be converted to the active carrier concentration by using Sze & Irvin curves [39, 40] or Equation (4.3) when the mobility of carrier is known:

$$\rho = \frac{1}{q}\left[\frac{1}{\mu_n n + \mu_p p}\right] \tag{4.3}$$

where μ is the carrier mobility in cm^2/volts-sec, q is the charge of an electron (= 1.602×10^{-19} C), and ρ is the resistivity in ohm-cm. The n and p indicate the electron and hole, respectively. To determine doping type from SRP measurement, the hot probe

method is generally used. The conductivity type can be determined by changing the polarity of the voltage. It is also important to take into account compensation effects, that is, the charge neutrality due to the background doping for investigating SRP results. The sheet resistance from the SRP data, which is useful to determine the extent of activation percentage after annealing treatment, can be obtained by the following Equation:

$$R_{sheet} = \left[\sum \frac{t}{\rho} \right]^{-1} \tag{4.4}$$

where ρ is the resistivity, and t is the depth of each sub layer [41].

In the SRP measurement for this study, the bevel angles between 0.00676–0.706° were used leading to ±3% uncertainty in depths, and ±15% uncertainty has been estimated for the accuracy of the measured resistivity. In addition, the sampling volume correction adds ±15% uncertainty. The probes were loaded with 3.0 g on the samples. The SRP calibration for germanium is however not well established compared with silicon [42, 43]. Thus, the comparison the SRP results with the SIMS data is necessary. Carrier concentrations (background doping) in the substrate, calculated using the single crystal mobility, agree very well (i.e. within ±14%) with the dopant concentrations found in the substrate using SIMS indicating a relatively good calibration of SRP to the expected active dopants in the substrate.

4.3 X-ray Diffraction (XRD)

After ion implantation, the lattice is damaged by atoms displaced from their substitutional sites sometimes so much so as to create an amorphous layer [44]. This induced damage generates strain in the crystal [45]. To observe the ion implantation induced damage and the formation of amorphous layers, high-resolution x-ray diffraction (HRXRD) and Rutherford backscattering spectrometry (RBS), which will be discussed in Section 4.5, have been used. The implant damage can be removed by subsequent thermal annealing. Because the diffraction patterns are sensitive to the crystallinity and lattice constant, XRD is capable of qualitatively indicating the effects of the presence of defects by the location of the peak and increased diffuse scattering. Thus, x-ray diffraction was also used to examine the effect of thermal annealing on the structural properties of the implanted germanium [46].

The basic concept of x-ray diffraction is expressed by Bragg's Law [47]. In the condition of satisfying Bragg's Law, the intensity of diffraction is strong. To examine the damage in the implanted single crystal materials, the rocking curves are used. The width of a rocking curve is a direct measurement of the amount of strain presented in the irradiated area of the crystal [48, 49]. That is, the changes can be determined from line broadening [50]. The depth of X-ray penetration can be calculated by the following Equation:

$$x = \frac{K_x \sin\theta}{2\mu} \tag{4.5}$$

where μ is the linear absorption coefficient in unit of cm^{-1}. Values of K_x for various assumed values of G_x are given in Table 4.2. G_x is determined by the intensity diffracted

by the layer of depth x as a fraction of the total integrated intensity diffracted by a specimen of infinite thickness. Generally, 95 percent of the total would be contributed in the result of x-ray diffraction [48]. In this study, the linear absorption coefficient of germanium for copper K_{α} radiation (λ = 1.54 Å) is 361.33 cm^{-1}. The peak for (100) germanium would appear at 33°. Thus, the depth of x-ray penetration is around 23 μm assuming G_x is 0.95 (that is, K_x is 3.00). Thus, the result of x-ray diffraction gave the information within the depth of ~ 23 μm from surface.

The rocking curves were collected with a high resolution diffractometer, equipped with a conventional x-ray source (sealed tube with Cu anode), a parabolic mirror, and a Bartels monochromator (Ge (220)). The role of the mirror is to collect all radiation that exit from the tube and to convert it in a parallel beam, so to increase the intensity of the beam. The monochromator is able to suppress unwanted wavelength, so that only a part of the Cu $K_{\alpha 1}$ line of copper spectrum survives. The spectra were collected with a slit put in front of the detector, to reduce the angular acceptance to 0.25°. The current was 40 mA, and the applied voltage was 40 kV. The used reflection was (004).

Table 4.2 Values of K_x for Various Assumed Values of G_x

G_x	0.50	0.75	0.90	0.95	0.99	0.999
K_x	0.69	1.39	2.30	3.00	4.61	6.91
x (μm) at 33°	5.20	10.48	17.33	22.61	34.74	52.08

4.4 Hall Effect Measurement

The SRP data relies on calibration based on data in previously published literature and known carrier mobility in a sample [39]. It is necessary that the actual mobility of the sample be measured to account for effects of radiation damages. The Hall effect measurement is an indispensable technique for the simultaneous determination of carrier density and mobility of carriers in semiconductors. The principle of the Hall effect measurement is demonstrated in Figure 4.4 [51].

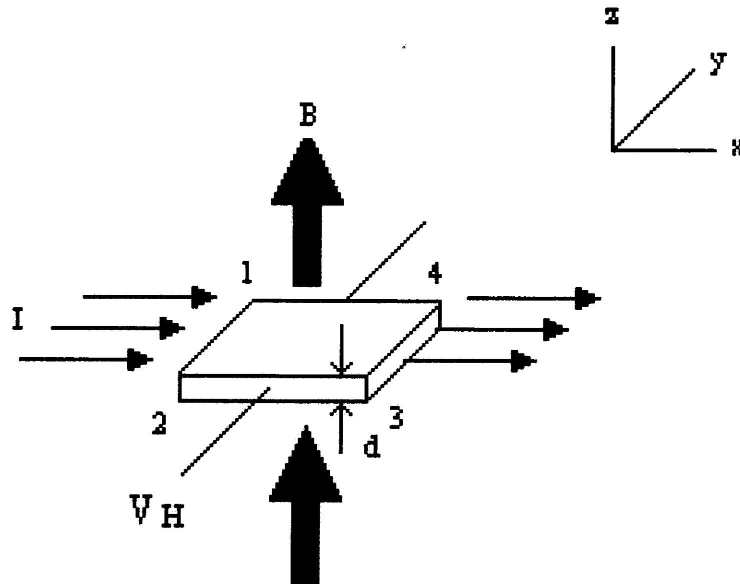

Figure 4.4 The principle of Hall effect measurement.

When a constant current (I_x) flows along the x-direction, and while applying simultaneously a magnetic field (B_z) in z-direction, electrons for n-type semiconductor (hole for p-type) move toward the negative y-direction, resulting in an excess surface electrical charge (i.e. due to the Lorentz force [52]) on the sides of the sample.

A resulting voltage is produced called the Hall voltage, V_H, as shown in Figure 4.4. This V_H can be expressed by Equation (4.6), where I_x is the current, B_z is the magnetic field, d is the effective sample thickness, n_0 is the carrier density, and q (= 1.602×10^{-19} C) is the elementary charge (Note that the sign is negative for electrons and positive for holes):

$$V_H = \frac{I_x B_z}{q n_0 d}. \tag{4.6}$$

Also, the sheet density n_s (= $n_0 d$) of charge carriers can be obtained by Equation (4.7):

$$n_s = \frac{I_x B_z}{q|V_H|}. \tag{4.7}$$

Finally, as a rapid measure of the total resistivity of surface, 4-point probe techniques are employed to measure the "sheet" resistance. The sheet resistance R_s can be determined by a van der Pauw resistivity measurement technique. In this technique, a dc current (I) is applied to contact 1 and out of contact 2, and the voltage V_{43} from contact 4 to contact 3 is measured. Next, the current flows into contact 2 and out of contact 3, and the voltage V_{14} from contact 1 to contact 4 is measured. Then, R_A, R_B, and R_s can be calculated by means of the following Equation:

$$\exp\left(-\frac{\pi R_A}{R_s}\right) + \exp\left(-\frac{\pi R_B}{R_s}\right) = 1$$
$$R_A = \frac{V_{43}}{I_{12}}, \text{ and } R_B = \frac{V_{14}}{I_{23}} \tag{4.8}$$

The carrier mobility is obtained from Equation (4.9):

$$\mu = \frac{|V_H|}{R_s IB} = \frac{1}{q n_s R_s}. \tag{4.9}$$

Unfortunately, Hall effect measurement was not successfully conducted in this study. It might be due to the leakage current between the implanted and the unimplanted region in germanium, which might have resulted from the relatively high background doping, the narrow bandgap, and the damage during implantation.

4.5 Rutherford Backscattering Spectrometry (RBS)

Rutherford backscattering spectrometry (RBS) is commonly used to evaluate the impurity distribution and the crystal damages. The 2 MeV He^+ was used as a projectile to obtain RBS spectrum. The intensity of the final backscattered primary projectile is recorded as a function of the final energy of the primary ions. The final energy (E_f) is related with mass of the target and the scattering angle (θ) [47]:

$$E_f = \left\{ \frac{\sqrt{M^2 - M_0^2 \sin^2\theta} + M_0 \cos\theta}{M_0 + M} \right\}^2 E_0 \qquad (4.10)$$

where M_0 and E_0 are mass and energy of an incident ion, and M is mass of the target.

RBS can detect and measure the thickness of an amorphous layer on a single crystal of the same material by means of the difference in the backscattered ion intensity between a channeling and a random direction. An ion beam that penetrates a single crystal in an "open" direction will channel deep into the crystal and therefore only a relatively small fraction will be backscattered. However, in an amorphous layer, an ion beam impinges in a "random" crystal direction, the intensity of the backscattered ions will be larger [53] as shown in Figure 4.5.

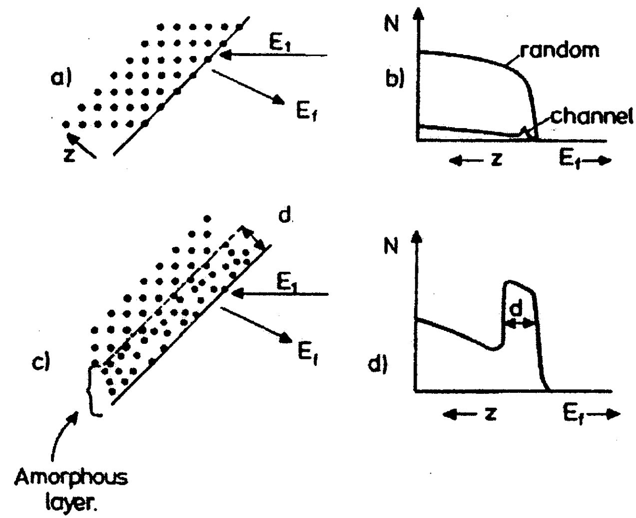

Figure 4.5 Detection of an amorphous layer with RBS. (a) Ion beam penetrating crystal in "open" direction; (b) corresponding spectrum of channel and random; (c) ion beam scattered from amorphous layer; (d) corresponding spectrum [53].

CHAPTER 5

RESULTS AND DISCUSSION

5.1 Observation of Dopants Implanted into Germanium

Boron and phosphorus implanted into germanium were measured by secondary ion mass spectrometry (SIMS), high resolution x-ray diffraction (HRXRD), and Rutherford backscattering spectrometry (RBS) to examine distribution of dopants and induced damage in the substrate. Implants with the same dose and different energies were chosen to study the variation of the dopant distribution with increasing energy, and implant with increasing dose were chosen to examine the effects of increasing amorphization due to increasing radiation damage, which are separately discussed in Section 5.3. The increasing amorphization can reduce the channeling component as the crystal structure of substrate changes from the crystalline to the amorphous state [44]. The doses and energies used to study the energy dependence of the profiles are believed to be below the threshold to form an amorphous layer, which is supported by SRIM simulations as well as the RBS spectra. The initial discussion and modeling focus on the profile dependence on energy in the non-amorphous regime of implantation. Modeling of the effects of amorphization is more complex and comments on this are left to the end of Chapter 5.

5.1.1 Observation of Dopant Distribution by SIMS

In Figure 5.1, as-implanted dopant profiles are shown with different doses and energies. The peak of distributions increased with increasing dose, and at higher energy the peak of distribution was observed deeper in the substrate. In Figure 5.2, as implanted dopant profiles in silicon were also shown with the same implant parameters as the case of germanium.

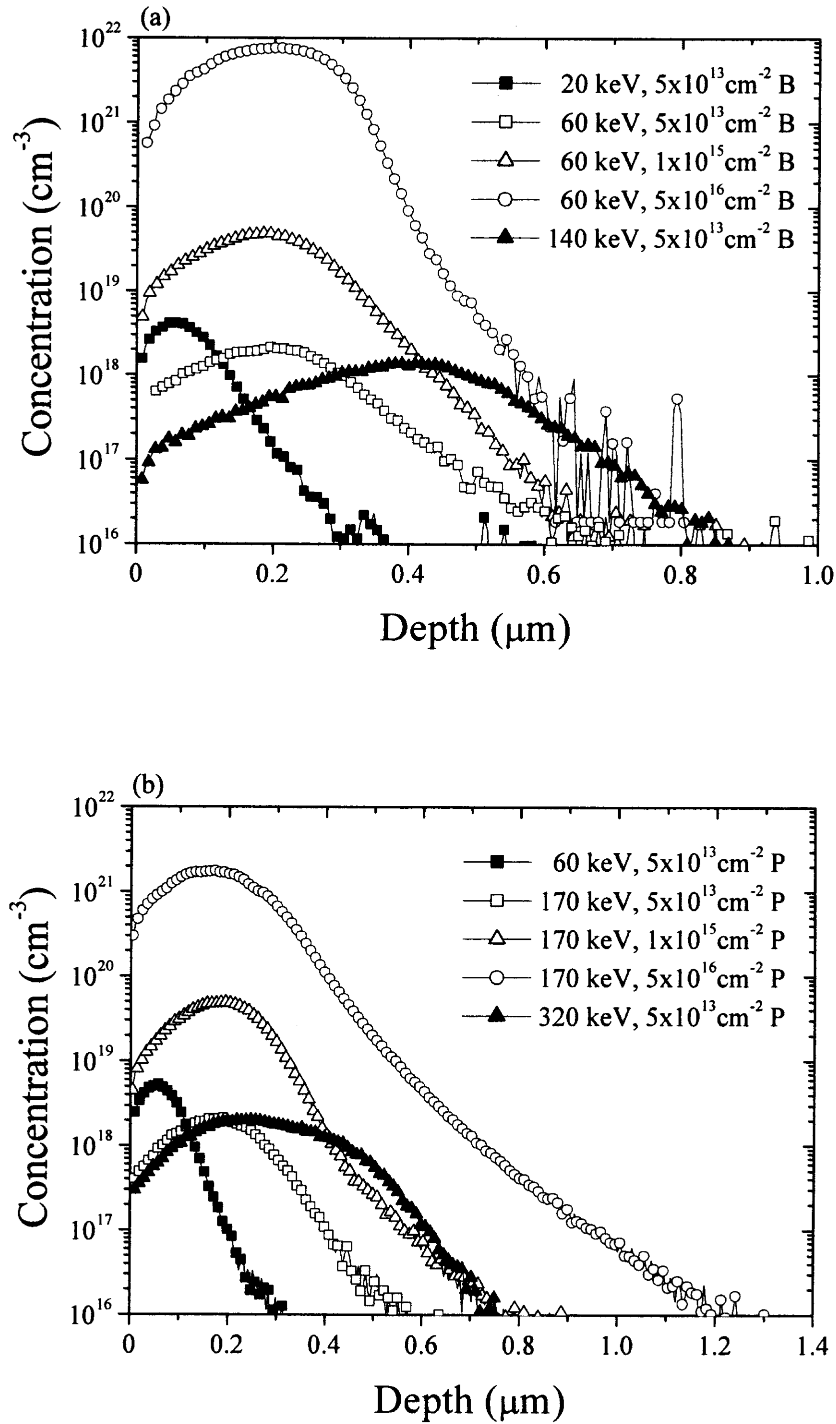

Figure 5.1 SIMS data of (a) boron and (b) phosphorus implanted into germanium with various doses and energies.

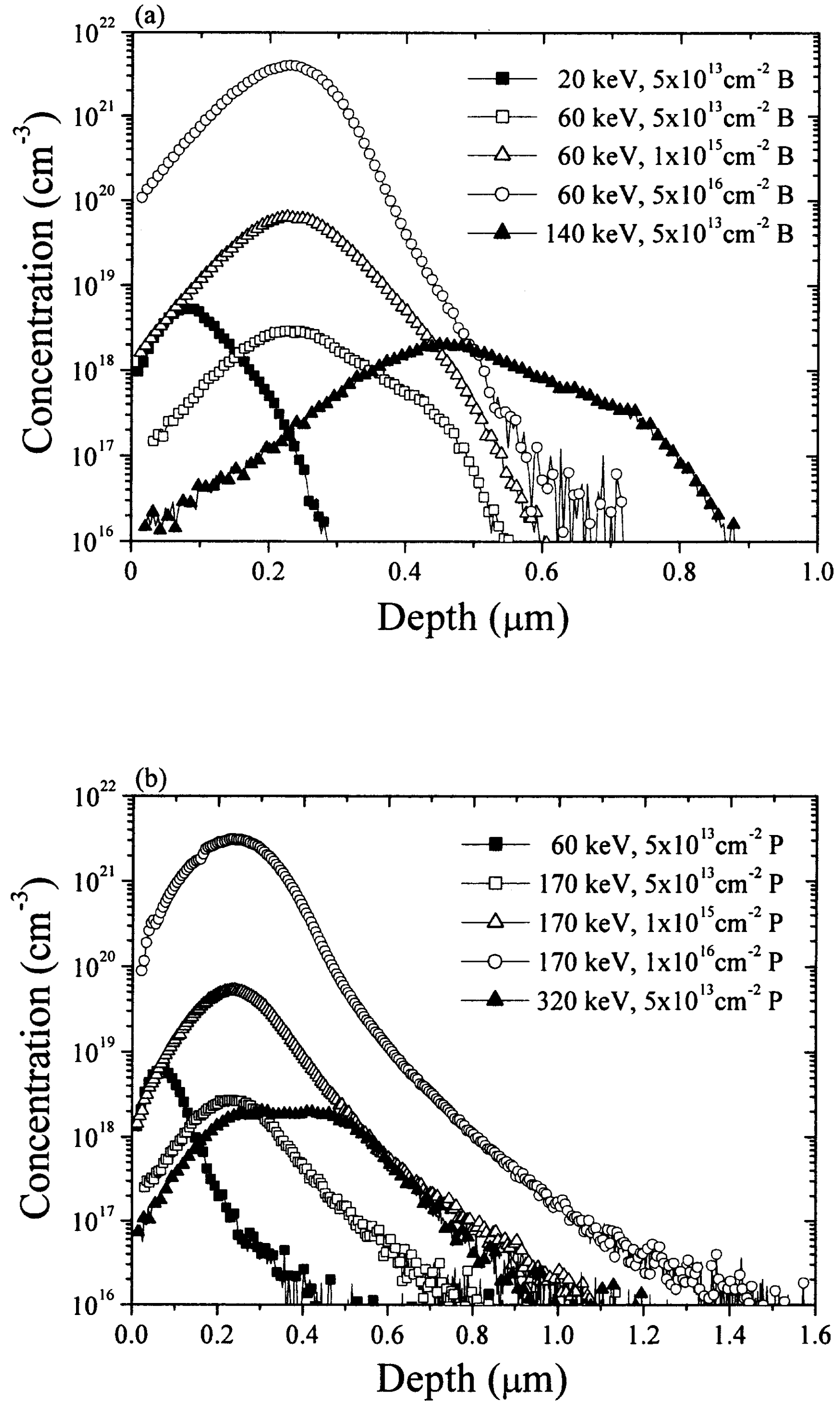

Figure 5.2 SIMS data of (a) boron and (b) phosphorus implanted into silicon with various doses and energies.

Table 5.1 The Implantation Conditions and the Obtained Areal Density from SIMS Measurement for the Boron Implanted into Germanium and Silicon Witness Wafers

Target	Energy (keV)	Dose (cm^{-2})	Areal density from SIMS (cm^{-2})
Ge	20	5×10^{13}	4.17×10^{13}
Si	20	5×10^{13}	5.33×10^{13}
Ge	60	5×10^{13}	4.90×10^{13}
Si	60	5×10^{13}	5.69×10^{13}
Ge	60	1×10^{15}	1.00×10^{15}
Si	60	1×10^{15}	1.10×10^{15}
Ge	60	5×10^{16}	1.61×10^{17}
Si	60	5×10^{16}	6.10×10^{16}
Ge	140	5×10^{13}	4.52×10^{13}
Si	140	5×10^{13}	5.30×10^{13}

Table 5.2 The Implantation Conditions and the Obtained Areal Density from SIMS Measurement for the Phosphorus Implanted into Germanium and Silicon Witness Wafers

Target	Energy (keV)	Dose (cm^{-2})	Areal density from SIMS (cm^{-2})
Ge	60	5×10^{13}	4.87×10^{13}
Si	60	5×10^{13}	5.76×10^{13}
Ge	170	5×10^{13}	4.57×10^{13}
Si	170	5×10^{13}	5.76×10^{13}
Ge	170	1×10^{15}	1.01×10^{15}
Si	170	1×10^{15}	1.10×10^{15}
Ge	170	5×10^{16}	4.11×10^{16}
Si	170	5×10^{16}	6.63×10^{16}
Ge	320	5×10^{13}	6.93×10^{13}
Si	320	5×10^{13}	7.82×10^{13}

As shown in Figure 5.1 (a) and Table 5.1, in the case of the highest boron dose implants, the total implanted dose detected by SIMS in the germanium was over twofold greater than in the silicon witness wafers. This is, as mentioned in Chapter 4, due to the inaccuracy of SIMS RSF for germanium.

5.1.2 Modeling by Pearson Distribution

The Pearson distribution requires knowledge of the first four moments, which are the *projected range* (the first moment, R_p), straggle (the second moment, σ_p), skewness (the third moment, γ), and kurtosis (the fourth moment, β), and from these four moments the appropriate one of twelve Pearson distributions can be chosen [33]. These four moments were, therefore, calculated from the SIMS data using Equations (2.22-25). In this calculation, the low concentrations of SIMS data, which would be the noise of the measurement, were subtracted from the measured profile in order to make more accurate calculations of the moments (e.g. below ~ 1×10^{16} cm^{-3}).

The moments of the boron and phosphorus implants can also be predicted either using the LSS theory or by a standard Monte-Carlo algorithm such as SRIM-2003 [26]. Two moments for the LSS theory have been previously tabulated for boron and phosphorus in "*Projected Range Statistics*" published by J. F. Gibbons, et al. [13], and are shown in Table 5.3 and 5.4 for boron and phosphorus in germanium and silicon, respectively. All four moments can also be calculated using SRIM-2003. These simulations were carried out using 99,999 counts, a 7° tilt and the material properties for amorphous germanium. Appropriate Pearson types obtained from the relation between the skewness and kurtosis, were also presented in Table 5.3 and 5.4.

Table 5.3 The first Four Moments with Pearson Type for Boron and Phosphorus in Germanium

Dose	Energy	R_p (μm)			σ_p (μm)			Skewness (γ)		Kurtosis (β)		Pearson Type
(cm^{-2})	(keV)	SIMS	LSS	SRIM	SIMS	LSS	SRIM	SIMS	SRIM	SIMS	SRIM	
Boron implantation into germanium												
5×10^{13}	20	0.0739	0.0474	0.0573	0.0448	0.0353	0.0284	1.3462	0.2447	6.5157	2.5225	VI
5×10^{13}	60	0.2024	0.1506	0.1443	0.0988	0.0814	0.0599	0.7731	-0.0876	4.3984	2.4837	IV
1×10^{15}	60	0.1835	0.1506	0.1443	0.0839	0.0814	0.0599	0.3902	-0.0876	3.4451	2.4837	IV
5×10^{16}	60	0.1907	0.1506	0.1443	0.0762	0.0814	0.0599	-0.0044	-0.0876	2.5382	2.4837	I
5×10^{13}	140	0.3751	0.3573	0.2984	0.1414	0.1404	0.0988	-0.0486	-0.4413	3.0001	2.8781	I
Phosphorus implantation into germanium												
5×10^{13}	60	0.0672	0.0475	0.0587	0.0387	0.0273	0.0297	1.0984	0.3422	5.2620	2.6966	VI
5×10^{13}	170	0.1810	0.1369	0.1542	0.0859	0.0626	0.0665	0.4473	0.0217	3.3435	2.5302	VI
1×10^{15}	170	0.1812	0.1369	0.1542	0.0821	0.0626	0.0665	0.3747	0.0217	3.7043	2.5302	IV
5×10^{16}	170	0.1773	0.1369	0.1542	0.0920	0.0626	0.0665	0.6568	0.0217	4.2360	2.5302	IV
5×10^{13}	320	0.2760	0.2627	0.2807	0.1315	0.0995	0.1041	0.3327	-0.2322	2.6793	2.6457	I

Table 5.4 The first Four Moments with Pearson Type for Boron and Phosphorus in Silicon

Dose	Energy	R_p (μm)			σ_p (μm)			Skewness (γ)		Kurtosis (β)		Pearson Type
(cm^{-2})	(keV)	SIMS	LSS	SRIM	SIMS	LSS	SRIM	SIMS	SRIM	SIMS	SRIM	
Boron implantation into silicon												
5×10^{13}	20	0.0926	0.0662	0.0790	0.0452	0.0283	0.0315	0.7094	-0.1026	3.4865	2.5898	I
5×10^{13}	60	0.2449	0.1903	0.2026	0.0864	0.0556	0.0605	0.3413	-0.5063	3.0982	3.1403	I
1×10^{15}	60	0.2318	0.1903	0.2026	0.0753	0.0556	0.0605	0.1352	-0.5063	3.4154	3.1403	IV
5×10^{16}	60	0.2154	0.1903	0.2026	0.0646	0.0556	0.0605	-0.2612	-0.5063	3.2024	3.1403	IV
5×10^{13}	140	0.4754	0.3974	0.4199	0.1255	0.0813	0.0914	0.0807	-0.8880	3.3491	4.3487	IV
Phosphorus implantation into silicon												
5×10^{13}	60	0.0820	0.0730	0.0843	0.0442	0.0298	0.0331	1.4997	0.0750	7.3159	2.6553	VI
5×10^{13}	170	0.2430	0.2149	0.2233	0.0964	0.0689	0.0699	0.6266	-0.2716	3.9718	2.8123	IV
1×10^{15}	170	0.2451	0.2149	0.2233	0.0958	0.0689	0.0699	0.7806	-0.2716	5.1076	2.8123	IV
5×10^{16}	170	0.2393	0.2149	0.2233	0.0878	0.0689	0.0699	0.3902	-0.2716	4.1551	2.8123	IV
5×10^{13}	320	0.3652	0.4060	0.4067	0.1406	0.1059	0.1055	0.1912	-0.5550	2.7088	3.2894	I

The resulted Pearson fits with the experiment data were shown in Figure 5.3 for the same energy and Figure 5.4 for the same dose. The Pearson distributions were well fitted to the experimental data. In Figure 5.3, at the highest boron dose case, the Pearson curve does not fit well the tail of the experimental data. However, as mentioned in Section 4.1, the SIMS data was suspect in this case.

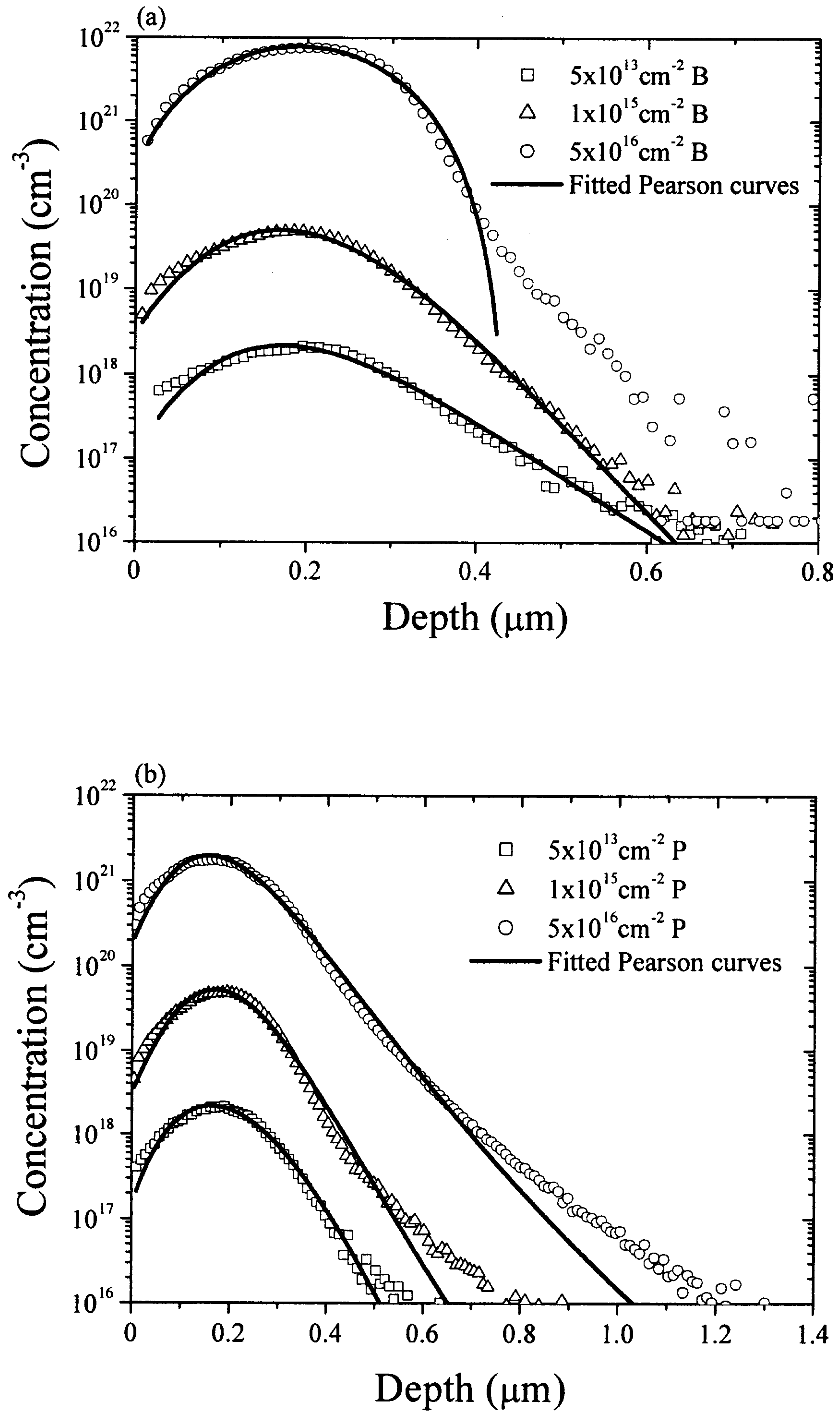

Figure 5.3 The SIMS data and the fitted Pearson distribution curves of (a) 60 keV boron and (b) 170 keV phosphorus implanted into germanium with various doses.

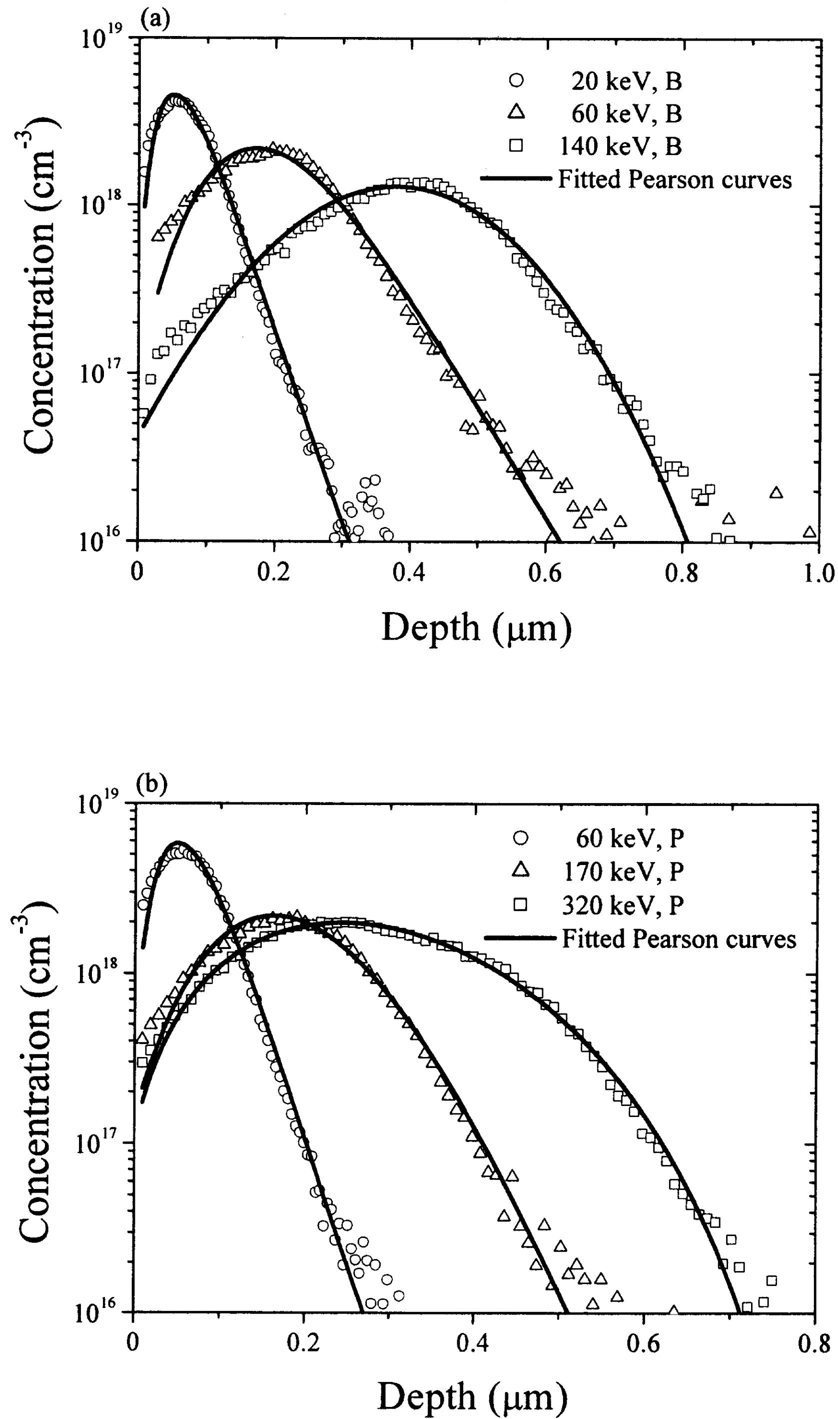

Figure 5.4 Comparison of experimental data from SIMS and fitted Pearson curves with various energies and same dose (5×10^{13} cm^{-2}): (a) boron and (b) phosphorus implantation into germanium.

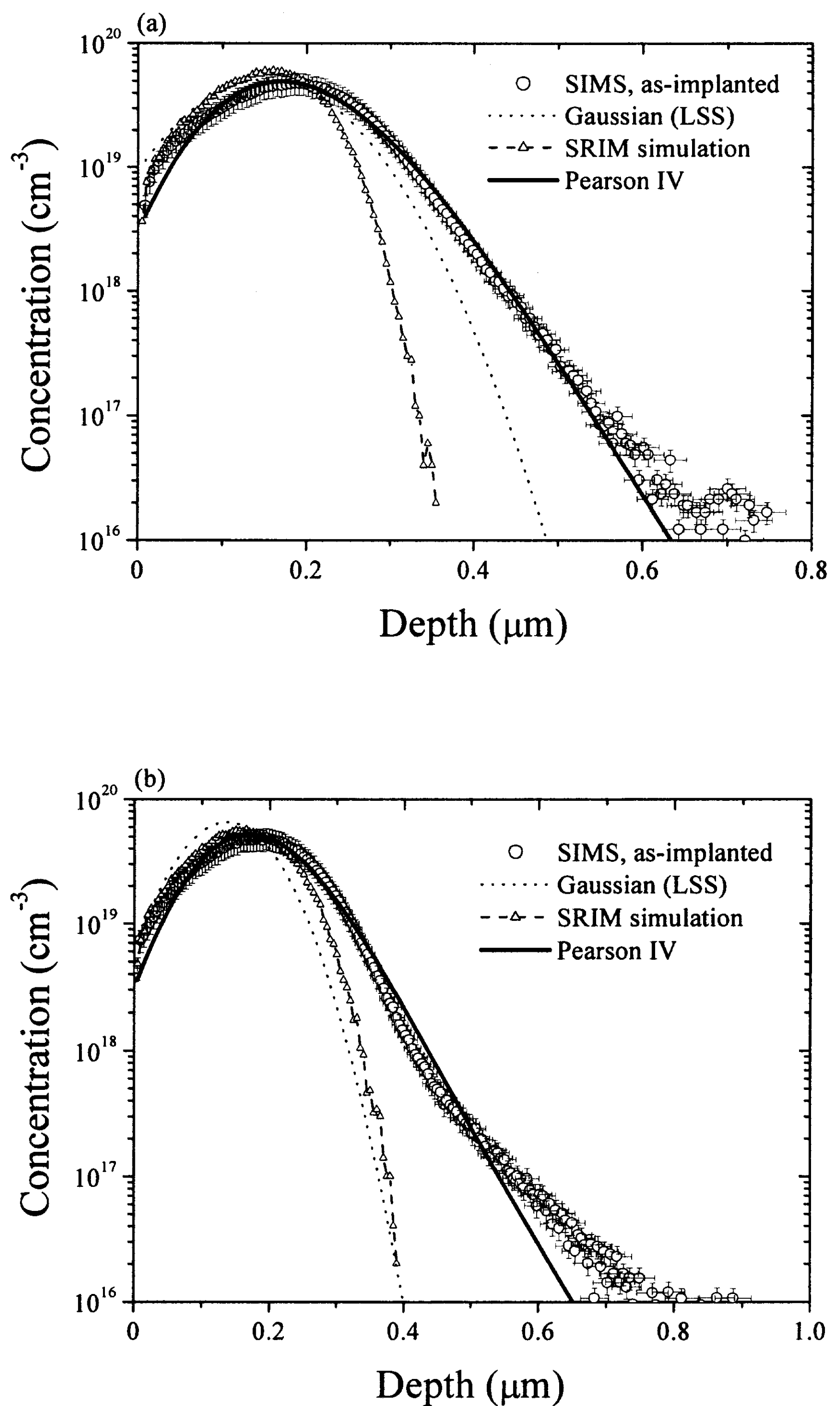

Figure 5.5 Comparison of SIMS data, Gaussian distribution based on LSS theory, and SRIM simulation compared to the fitted Pearson distribution curves of (a) 60 keV, 1×10^{15} cm^{-2} boron and (b) 170 keV, 1×10^{15} cm^{-2} phosphorus implanted into germanium.

As shown in Figure 5.5, the Pearson curves were better fitted with the experimental data from SIMS compared to both of Gaussian distribution based on LSS theory and SRIM simulation. It should be noted, however, that both the LSS and SRIM calculations were done to gain insight about the implants into germanium rather than to compare to state of the art implant calculations. More complete Monte-Carlo simulation that calculates channeling contributions, do exist and would be expected to agree better with the experimental profiles.

5.1.3 Relationship between Moments and Energy

Implants with the same dose and different energies were chosen to study the variation of the dopant distribution with increasing energy. It has previously been suggested that the first two moments dependence on energy can be fit relatively well with an empirical relation $A*E^{B}$, where A and B are fitting constants, so that Pearson distributions over the entire implant range may be generated [32]. The unit of energy in the empirical relation is keV, and the first two moments have the unit of μm. Relatively good fits to the SIMS data compared to theoretical predictions were made for both boron and phosphorus, as shown in Figure 5.6 (a) and (b) respectively. The constants A and B were calculated to be 0.00786 and 0.783 for boron and 0.00311 and 0.780 for phosphorus.

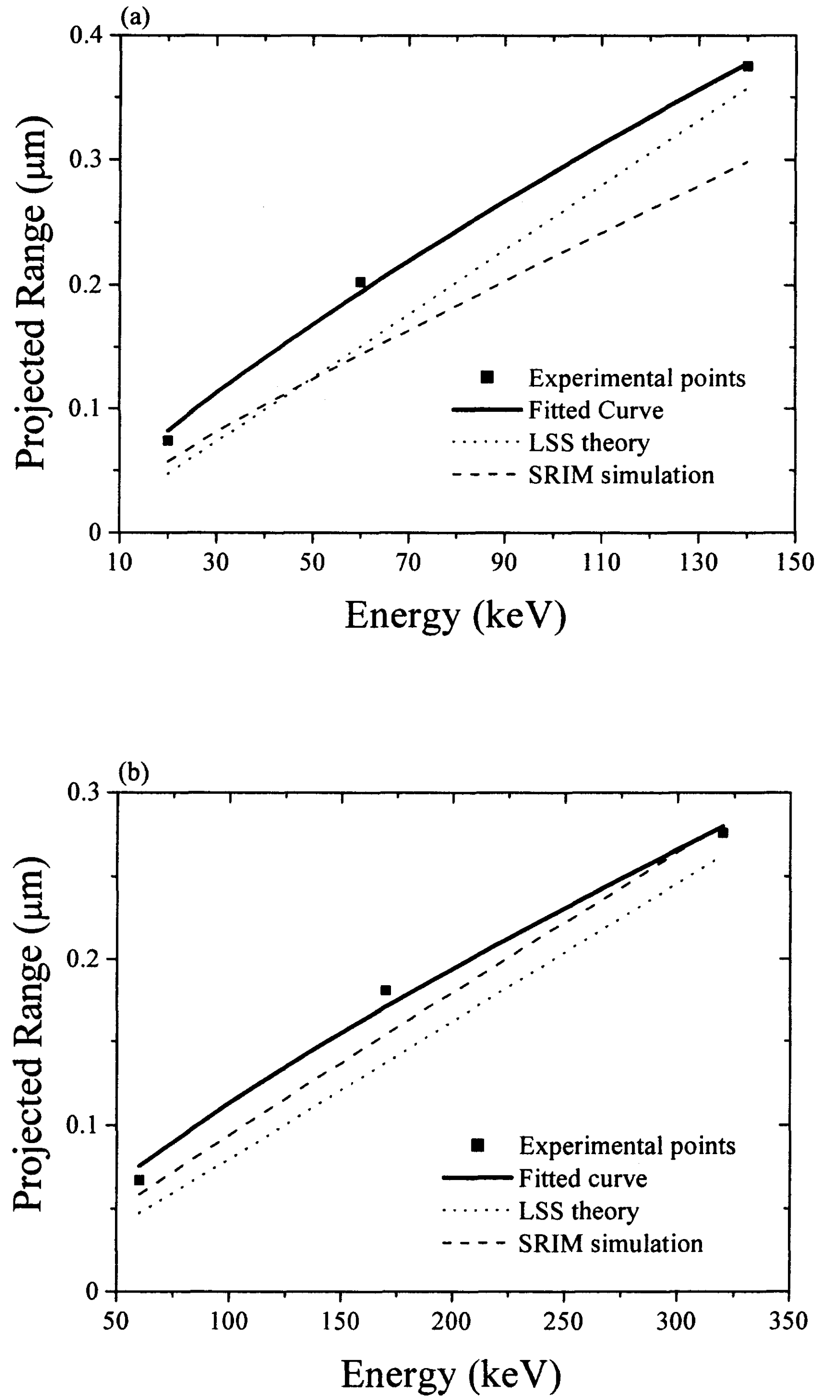

Figure 5.6 Experimental points, fitted curve, and data from LSS theory and SRIM simulation for *projected range* (R_p) of (a) boron and (b) phosphorus 5×10^{13} cm^{-2} implants into germanium. The fitted curve for boron is $R_p[\mu m] = 0.00786E^{0.783}$ and $R_p[\mu m] = 0.00311E^{0.780}$ for phosphorus. The unit of energy is keV.

The *projected range* as a function of energy for the LSS, SRIM and SIMS results for the case of boron and phosphorus implantation in germanium with a dose of 5×10^{13} cm^{-2} are presented in Figure 5.6 (a) and (b). The *projected range* was found to be as much as 56% and 41% greater than that predicted by LSS theory for boron and phosphorus at the lower energy, respectively. This difference between the experimental data and LSS theory is reduced as the energy is increased. The neglect of the channeling effect in the SRIM simulation and the LSS theory presumably contributes to this disagreement. In addition, inaccuracy of the Thomas-Fermi adopted potential in the LSS theory is believed to produce errors for the LSS predictions at low energy [28].

The *projected ranges* were shallower in germanium than in silicon for the same ion species and energy. Rates of energy loss have been calculated using the LSS theory for the nuclear and electronic components to better understand this trend and are shown in Figure 2.4. The rates of energy loss are used to calculate a *range* (i.e. the total path length in the lattice), which is a combination of both the depth of penetration and the lateral excursion of the atom in the lattice. To calculate the *projected range* (i.e. the first moment calculated from the SIMS profile), an approximate relationship between the *projected range* and the *range* has been derived for the LSS theory, which accounts for the scattering angle dependence on incident and target masses [25] as defined in Equation (2.15).

For phosphorus, according to the LSS theory, both nuclear and electronic stopping play significant roles in the slowing of the phosphorus ions depending on the implant energy regime. In all cases, the energy loss is greater in germanium than in

silicon and the shallower *projected ranges* are easily understood as a result of a faster rate of energy loss in germanium.

For boron, the electronic energy loss is calculated to dominate over the nuclear energy loss in both silicon and germanium, Figure 2.4 (a). The LSS theory predicts that the stopping power in silicon is, furthermore, greater than that in germanium leading to longer predicted *ranges* in germanium than in silicon (i.e. longer total path lengths). Shallower *projected ranges* in germanium compared to silicon are, nevertheless, observed and predicted by the LSS theory because of the higher lateral excursion produced by the larger angle collisions with the higher mass germanium. The ratio of R to R_p is found to be 73% greater in germanium than silicon, which is enough to account for the shallower predicted *projected range* in germanium despite the longer boron *range* in silicon.

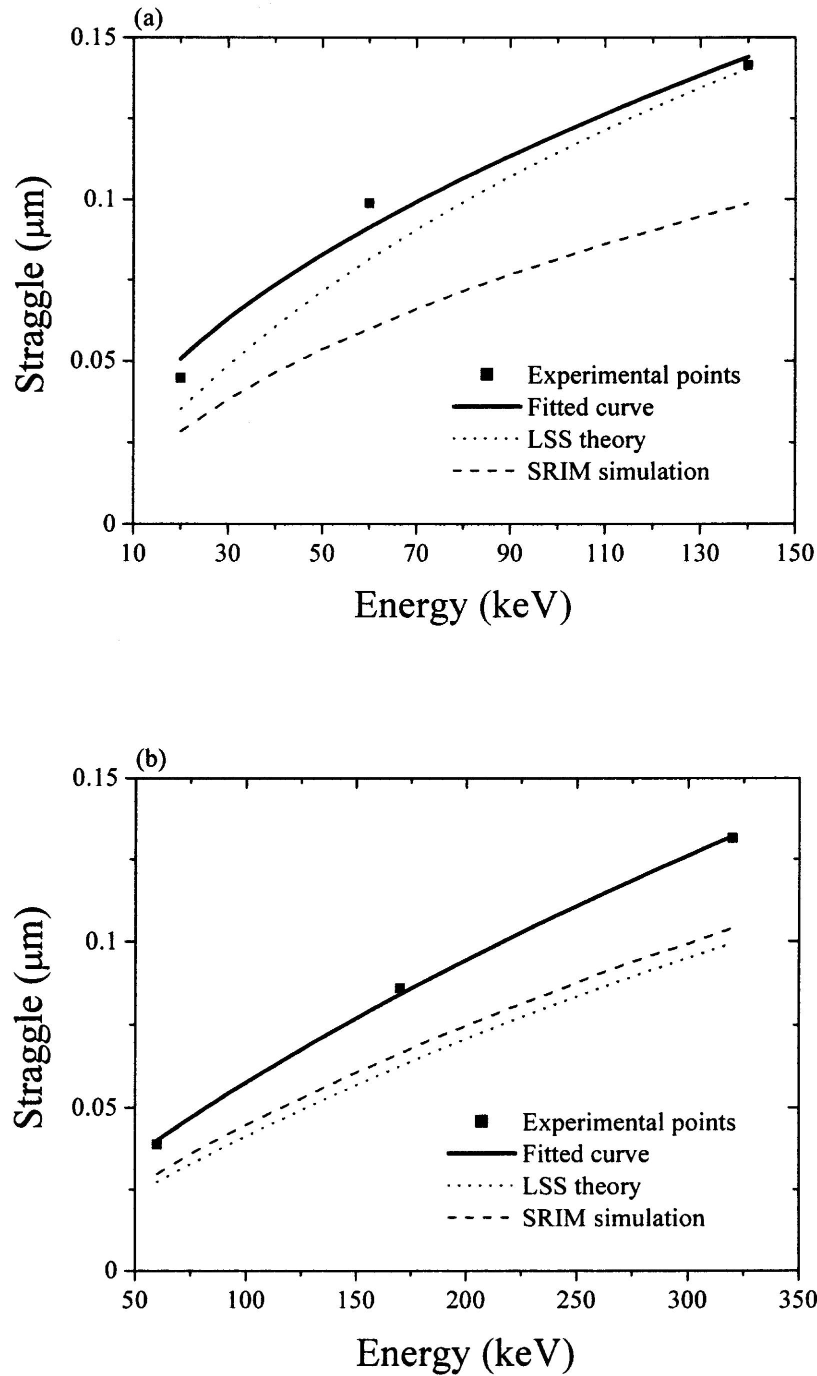

Figure 5.7 Experimental points, fitted curve, and data from LSS theory and SRIM simulation for straggle (σ_p) of 5×10^{13} cm^{-2} (a) boron and (b) phosphorus implants into germanium. The fitted curves are $\sigma_p[\mu m] = 0.0101E^{0.537}$ and $\sigma_p[\mu m] = 0.00216E^{0.713}$ for boron and phosphorus, respectively. The unit of energy is keV.

The boron and phosphorus straggle (i.e. the second moment) after 5×10^{13} cm^{-2} dose implants in the germanium are shown as a function of energy for the LSS, SRIM and SIMS results, Figure 5.7 (a) and (b), respectively. The straggle of the phosphorus and boron measured by SIMS was as much as 42% greater than that calculated by the LSS theory, and 65% greater than that simulated by the SRIM simulation. The fitted curve has the same functional form as that used for the *projected range* [32] and the constants for boron were 0.0101 and 0.537, for A and B respectively; while for phosphorus they were found to be 0.00216 and 0.713, respectively. Small straggle is important for the fabrication of sharp dopant profiles required for shallow junctions and other size-scaled electronic devices. It is interesting to note, therefore, that the boron straggle is greater in the germanium than the silicon for the same implant energies (i.e. a greater straggle was observed in the germanium despite a smaller projected range than in silicon).

Figure 5.8 shows the skewness (the third moment) as a function of energy for the experimental data and SRIM calculation for 5×10^{13} cm^{-2} boron or phosphorus in germanium. The experimental data was found to be higher than predicted by the SRIM in all cases, which is a signature of the calculated SRIM distribution decreasing more sharply on the substrate side of the profile than that measured by the SIMS. The experimentally obtained skewness was, furthermore, fit with the functional form $A-B\ln(E)$ [31], where E is the energy in keV and A, B are the coefficients determined from the SIMS data. The resulting fits were $3.53-(0.707)\ln(E)$ for the boron, and $3.00-(0.474)\ln(E)$ for the phosphorus implantation.

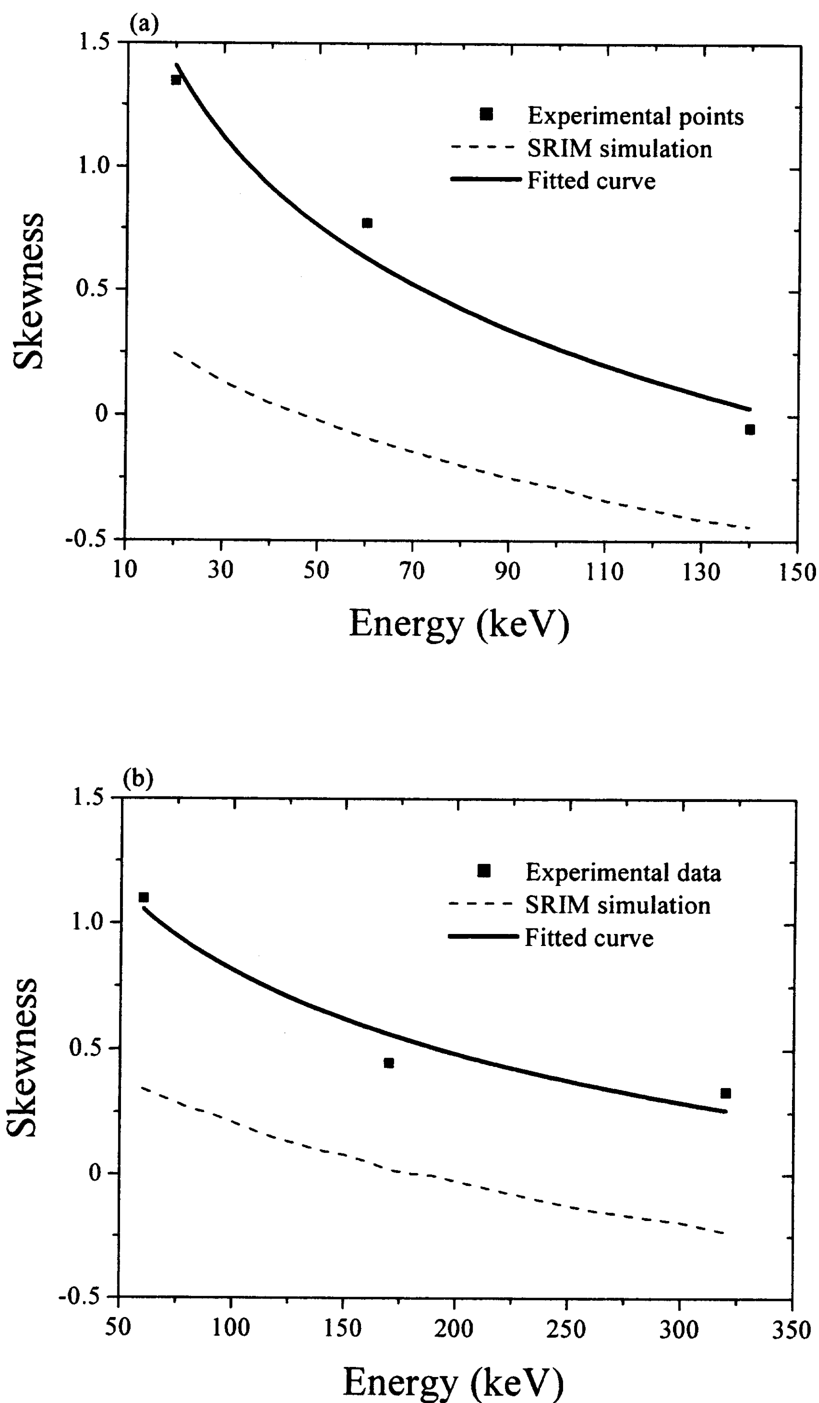

Figure 5.8 Experimental points, fitted curves, and data from SRIM simulation for skewness (γ) of 5×10^{13} cm^{-2} (a) boron and (b) phosphorus implants into germanium. The fitted curves are $\gamma = 3.53-(0.707)\ln E$ and $\gamma = 3.00-(0.474)\ln E$ for boron and phosphorus, respectively. The unit of energy is keV.

The kurtosis or forth moment as a function of energy for the experimental data and SRIM calculation are shown for boron and phosphorus implantation into germanium with the dose of 5×10^{13} cm^{-2}, in Figure 5.9. The kurtosis is found to be higher than that predicted by the SRIM simulation in most cases and the values above 3 are indicative of the extended tails that are not predicted by the simulation. The smaller kurtosis predicted by the SRIM calculation is in part due to the neglect of the channeling component in the simulation. This disagreement becomes less at higher energies.

To estimate the kurtosis over the entire range of implant conditions the fourth moment was fitted using a functional form $A+B\gamma^2$. Previously, the kurtosis has been found to correlate with the square of the skewness [23, 54], and this functional form appears to hold over the energies considered in this work, Figure 5.9. The resulting curves were $3.33+(1.64)\gamma^2$ for boron and $2.46+(2.51)\gamma^2$ for phosphorus.

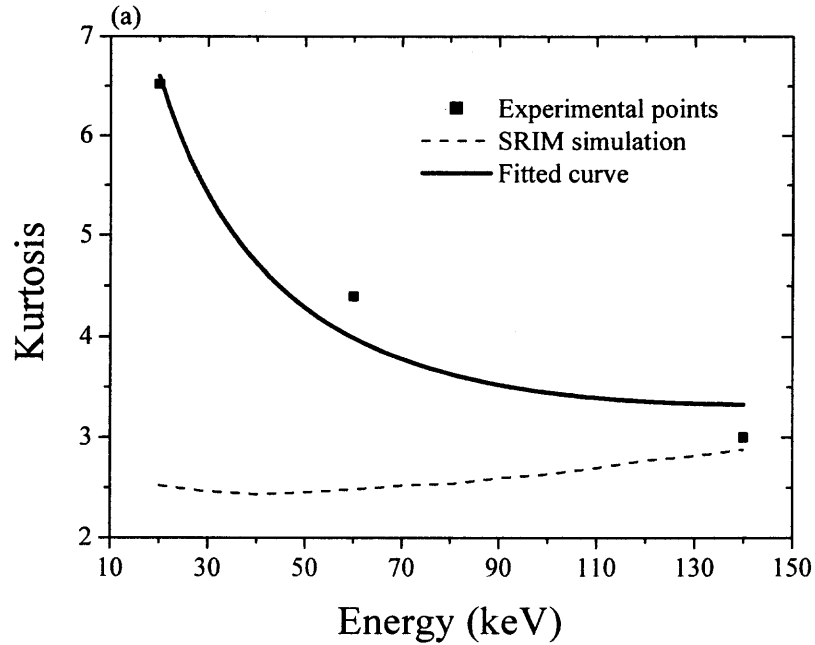

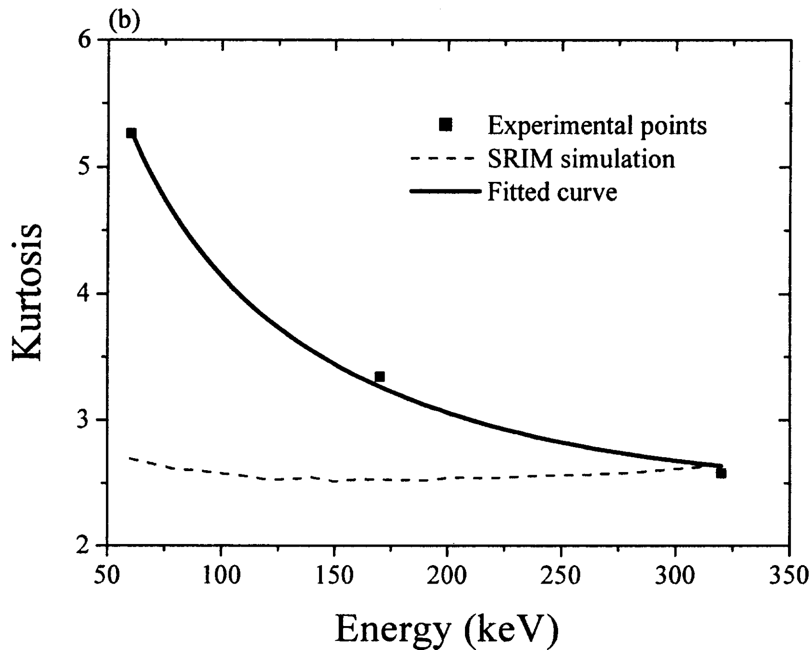

Figure 5.9 The kurtosis (β) dependence on energy for 5×10^{13} cm^{-2} (a) boron and (b) phosphorus implants calculated from SIMS profiles and SRIM simulated profiles. The experimental kurtosis was fit with (a) $\beta = 3.33+(1.64)\gamma^2$ for boron and (b) $\beta = 2.46+(2.51)\gamma^2$ for phosphorus.

Pearson fitting parameters can be derived from the first four moments of the implant distribution. However, initially the appropriate one of twelve distributions must be selected to fit the implant distribution. Ashworth, et al. have shown that the appropriate distribution can be selected based on the implants skewness and kurtosis [33]. The respective relationship between skewness, kurtosis and the Pearson's domains for all cases considered in this work are shown in Figure 5.10. Most SRIM simulation cases fell into the region of the Pearson I distribution, whereas, some implant profiles measured with SIMS required either the Pearson IV or VI distributions in addition to the Pearson I to fit the profiles.

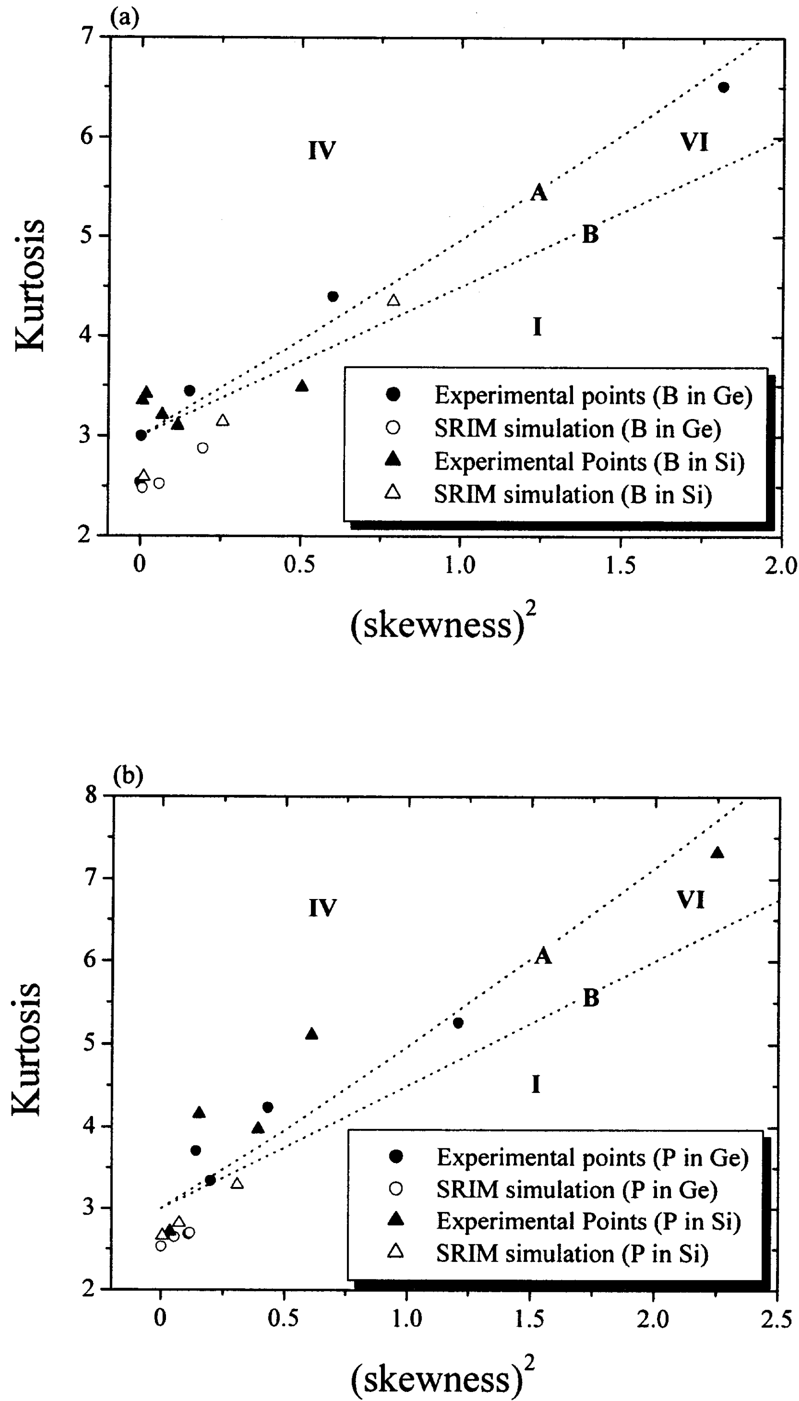

Figure 5.10 Domains of Pearson types on the β-γ^2 plane: the experimental points and SRIM simulation (a) for boron and (b) for phosphorus implantation into germanium and silicon. The region of Pearson type is indicated (i.e. I, IV, or VI). The line A and B are the boundary between Pearson types.

After the appropriate distribution was selected the Pearson parameters were calculated from the first four moments for each of the implant conditions [33]. All Pearson parameters calculated in this study are summarized in Tables 5.5 and 5.6.

Table 5.5 Summary of Pearson Parameters for Boron Implanted into Germanium

Energy (keV)	R_p (μm)	σ_p (μm)	Skewness	Kurtosis	Pearson type
20	0.0821	0.0505	1.4120	6.5998	VI
30	0.1127	0.0627	1.1254	5.4069	VI
40	0.1412	0.0732	0.9220	4.7240	IV
60	0.1940	0.0910	0.6353	3.9919	IV
80	0.2430	0.1062	0.4319	3.6359	IV
100	0.2894	0.1198	0.2741	3.4533	IV
120	0.3338	0.1321	0.1452	3.3646	IV
140	0.3766	0.1435	0.0363	3.3322	IV

Table 5.6 Summary of Pearson Parameters for Phosphorus Implanted into Germanium

Energy (keV)	R_p (μm)	σ_p (μm)	Skewness	Kurtosis	Pearson type
60	0.0758	0.0400	1.0593	5.2764	IV
70	0.0855	0.0447	0.9862	4.9013	VI
110	0.1216	0.0617	0.7720	3.9558	VI
120	0.1302	0.0656	0.7307	3.8003	I
170	0.1708	0.0841	0.5656	3.2631	I
220	0.2089	0.1011	0.4434	2.9535	I
280	0.2521	0.1200	0.3291	2.7319	I
320	0.2798	0.1320	0.2658	2.6374	I

5.2 Activation Annealing

Annealing is necessary to remove the induced damage during ion implantation as well as to electrically activate dopants. To examine electrical activation and dopant diffusion, all samples were annealed at either 400, 600, or 800°C for 3 hours in nitrogen ambient.

5.2.1 Boron Activation Behavior

Figure 5.11 shows 60 keV, 1×10^{15} cm^{-2} boron implanted into germanium (SIMS data) after 400 and 600°C annealing, and as-implanted case. Negligible broadening of the boron profiles was observed after annealing at 400 or 600°C, consistent with the diffusion lengths expected from previously reported diffusivities in the literature [55]. The absence of enhanced diffusion due to implant damage or an increase in dopant activation suggests a significantly different and enigmatic relationship between boron and the point defects formed in germanium by the implant.

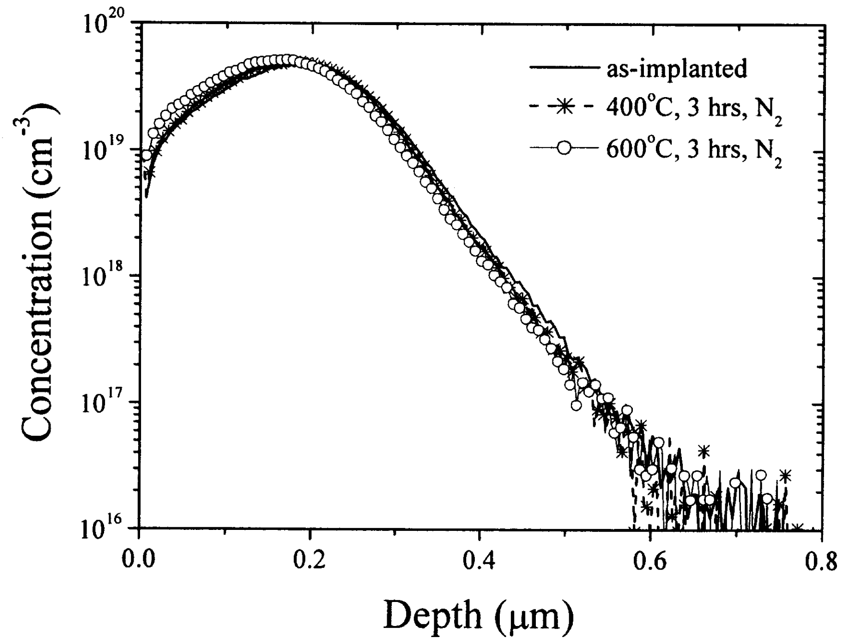

Figure 5.11 Comparison of SIMS data for 60 keV, 1×10^{15} cm^{-2} boron implanted into germanium after 400 and 600°C annealing, and as-implanted case.

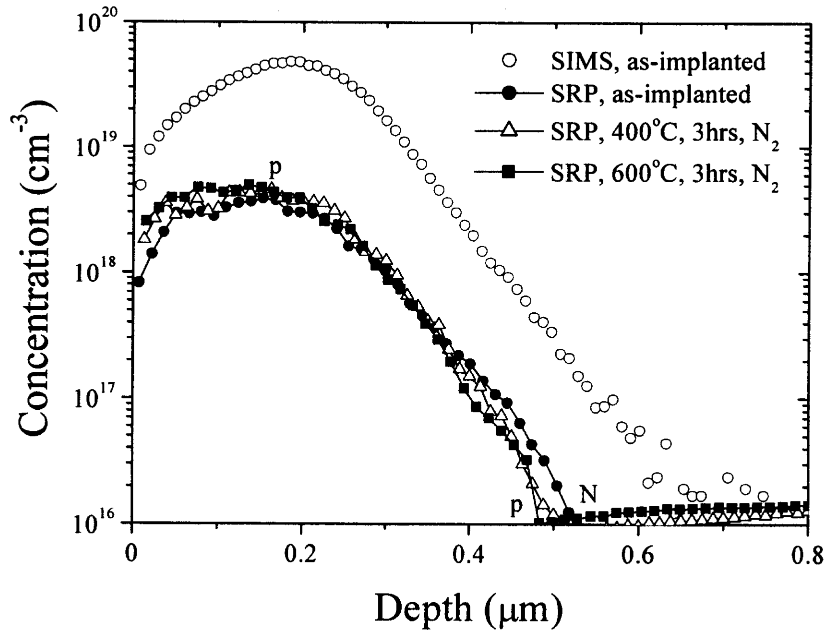

Figure 5.12 SIMS and SRP data of the as-implanted and annealed cases (3 hours at either 400 or 600°C in N_2) for 60 keV, 1×10^{15} cm^{-2} boron implant into germanium. The n and p's indicate carrier type.

SRP measurements indicated hole carrier concentrations in the boron implanted regions immediately after boron implantation in Figure 5.12, resulting in sheet resistances of 388, 171, and 18 ohms/sq for the 5×10^{13}, 1×10^{15}, and 5×10^{16} cm^{-2} boron doses, respectively, in Table 5.7. No increase in carrier concentration was observed with subsequent annealing at either 400 or 600°C, Figure 5.12. P-type defect centers (H1, H2 and H3) have previously been identified as a result of implant damage, however, previously these were observed to anneal out at temperatures above 350°C [7], suggesting that these defects were not responsible for the observed hole concentrations in this study.

Table 5.7 Sheet Resistance from SRP for Boron in Germanium

Dose (cm^{-2})	Temperature (°C)	Sheet Resistance (ohms/sq)
	as-implanted	388
5×10^{13}	400	382
	600	323
	as-implanted	171
1×10^{15}	400	153
	600	150
	as-implanted	18
5×10^{16}	400	15
	600	19

Immediate activation of 100% of all boron implanted into germanium without annealing has previously been reported for boron implants (but not BF_2) as high as 1×10^{14} cm^{-2} and for energies ranging from 25-150 keV [7]. Peak hole concentrations measured in this study, for the case of 5×10^{13} cm^{-2} dose, were also approximately the same as measured by SIMS suggesting 100% activation. For higher doses, 1×10^{15} and 5×10^{16} cm^{-2}, above that examined by Jones and Haller, the peak carrier concentration did not increase linearly with boron concentration, Figure 5.13, possibly because of increasing implant damage.

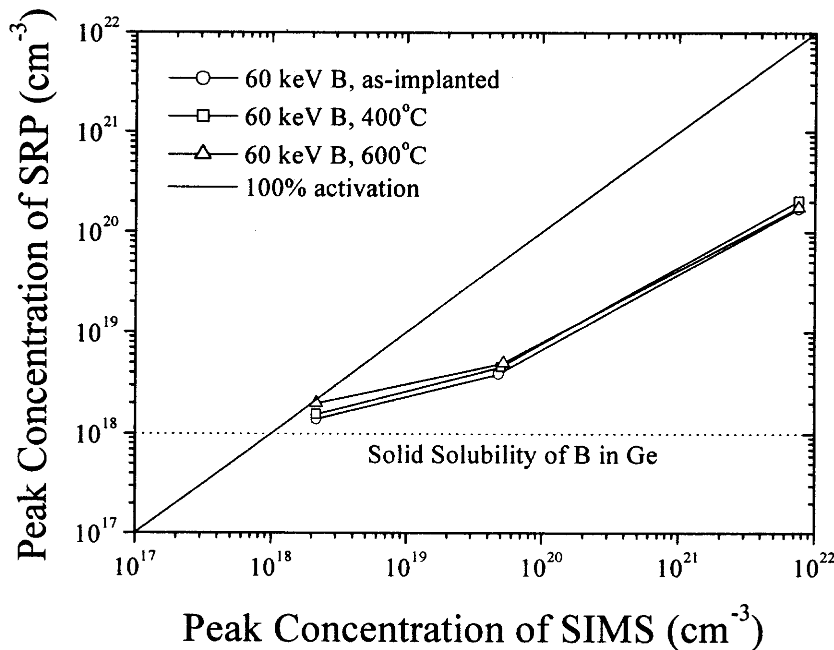

Figure 5.13 Summary of peak for boron concentrations measured from SRP and SIMS assuming single crystal mobilities for germanium [39]. Previously reported solid solubilities of boron in germanium were also shown [55].

5.2.2 Phosphorus Activation Behavior

In contrast to boron implant, annealing of the phosphorus implants significantly changed the electron concentrations in the implanted region, which is consistent with the previous report [59]. Figure 5.14 shows SIMS and SRP data for 170 keV, 5×10^{16} cm^{-2} phosphorus implant into germanium after 400 and 600°C annealing. Initially a p-type region was observed immediately after the phosphorus implant. Annealing at 400°C resulted in an increase of the peak electron concentration switching the region to n-type, and annealing at 600°C further increased the peak electron concentration to as high as 2×10^{19} cm^{-3}, leading to sheet resistances of 157 and 13 ohms/sq for the temperatures of

400 and 600°C, Table 5.8. This behavior is qualitatively similar to dopant activation in Si [57], for which both phosphorus and boron implants must be annealed to remove damage and dissolve dopants on substitutional sites. The peak carrier concentrations were, however, lower than previously reported dopant solid solubilities at this temperature [55], but were similar to what has been observed in more recent reports [42]. Possible sources of discrepancy are improper calibration of SRP and residual unannealed damage leading to an over estimate of the carrier mobility used to calculate the carrier concentration.

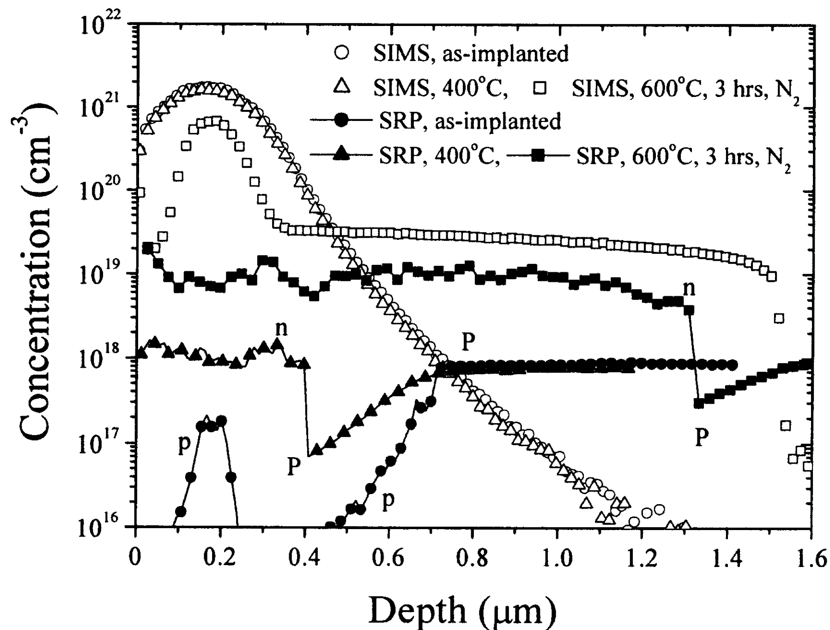

Figure 5.14 SIMS and SRP data of the as-implanted and annealed cases (3 hours at either 400 or 600°C in N_2) for 170 keV, 5×10^{16} cm^{-2} phosphorus implant into germanium. The n and p's indicate carrier type.

Table 5.8 Sheet Resistance from SRP for Phosphorus in Germanium

Dose (cm^{-2})	Temperature (°C)	Sheet Resistance (ohms/sq)
5×10^{13}	as-implanted	N/A
	400	N/A
	600	N/A
1×10^{15}	as-implanted	N/A
	400	201
	600	150
5×10^{16}	as-implanted	N/A
	400	157
	600	13

Negligible phosphorus diffusion was observed after annealing at 400°C for 3 hours in all cases, Figure 5.14, 5.15, and 5.16. The phosphorus diffusion after the 5×10^{13} cm^{-2} implant exhibited a slow diffusing peak with a faster diffusing tailing edge, Figure 5.15, which is similar to post-implant transient enhanced diffusion (TED) observed for boron and phosphorus in Si [58]. As the dose was increased and concentrations increased above the intrinsic carrier concentration, ~ 4×10^{18} cm^{-3} (at 600°C), the phosphorus profiles flattened out and showed very non-gaussian behavior, Figure 5.16. Such profiles are characteristic of highly extrinsic diffusion and can be explained qualitatively as a consequence of a very rapid diffusivity in the high concentration region, which leads to uniformly distributed regions terminated by sharp leading edges due to the slower low concentration diffusivity.

Chui et al. have successfully modeled the concentration dependence for phosphorus in germanium using an extrinsic diffusivity of the form $D \sim (n/n_i)^2$ [42]. An order of magnitude estimate of the phosphorus diffusion length can be made to determine whether the observed diffusion depths are reasonable or enhanced due to radiation damage (e.g. TED). Assuming that the concentration remains constant and approximately equal to the concentrations measured by SIMS in Figure 5.14 and 5.16, diffusion lengths of 0.58 μm and 1.72 μm were calculated for the 10^{19} and 3×10^{19} cm^{-3} cases, respectively [23, 42]. These diffusion lengths are of the same order of magnitude as the observed diffusion depths and suggest that the extremely rapid diffusion might only be a consequence of the extrinsic diffusivity and not related to TED. The immobile phosphorus peak in the highest dose case (see Figure 5.14), however, clearly indicates more complex diffusion dynamics for high dose implants with concentrations over $\sim 4\times10^{19}$ cm^{-3} phosphorus, and we furthermore note that, if measured carrier concentrations (SRP) are used rather than SIMS concentrations, the calculated diffusion lengths are much too slow to explain the observed diffusion. Further investigation is needed to evaluate the disagreement between SIMS and SRP.

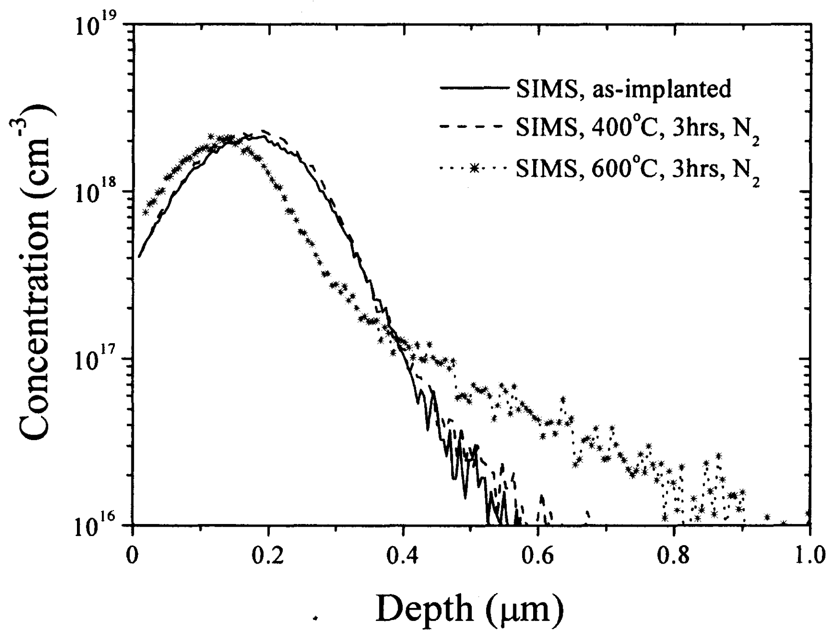

Figure 5.15 SIMS of the as-implanted and annealed cases (3 hours at either 400 or 600°C in N_2) for 170 keV, 5×10^{13} cm^{-2} phosphorus implant into germanium.

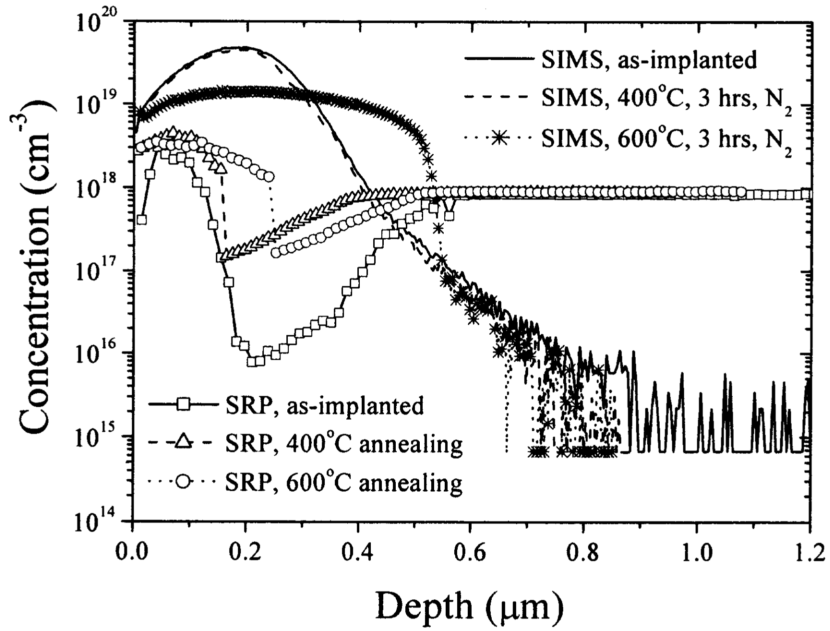

Figure 5.16 SIMS and SRP data of the as-implanted and annealed cases (3 hours at either 400 or 600°C in N_2) for 170 keV, 1×10^{15} cm^{-2} phosphorus implant into germanium.

In Figure 5.17, the electron concentrations increase with increasing annealing temperature, while the electron concentrations remain below reported solid solubilities even after long anneals at 600°C [55].

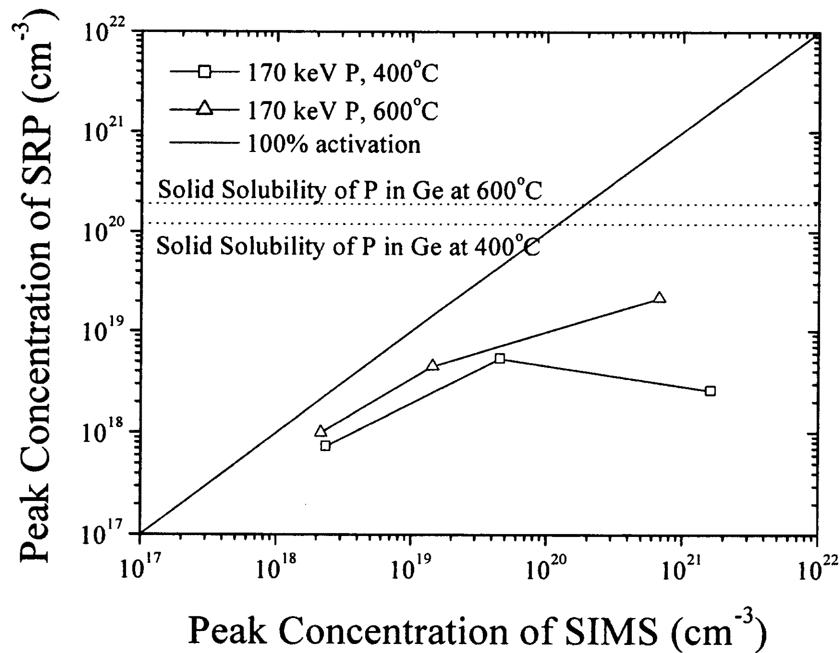

Figure 5. 17 Summary of peak phosphorus concentrations measured from SRP and SIMS assuming single crystal mobilities for germanium [39]. Previously reported solid solubilities of phosphorus in germanium were also shown [55].

5.3 Observation of Damage Induced by Ion Implantation

RBS-channeling measurements were performed by G. Bisognin at the University of Padova on the germanium implanted with phosphorus and boron to observe the implantation-induced damage. In Figure 5.18, the resulting RBS spectra are shown for various doses of boron (at 60 keV) and phosphorus (at 170 keV) implanted into germanium. The spectra were taken in channeling geometry along the [001] direction. As reference, a spectrum in a random geometry was also measured. It is clear that the germanium substrate, which was implanted with 1×10^{15} cm^{-2} phosphorus, is amorphized (the green spectrum had the same high of the red random spectrum in the region of higher-energy). As the phosphorus dose was increased (the blue spectrum) the layer apparently undergoes a reordering, since the channeling yield is measured to decrease indicating more crystalline behavior. This effect is very probably due to the phenomenon of Ion Beam Induced Epitaxial Crystallization (IBIEC). The beam of phosphorus is able, at 170 keV, to recrystallize partially the implanted-damaged layer, maybe assisted by heating due to the high dose implantation. Csepregi, et al. reported that epitaxial regrowth of ion-implanted amorphous germanium occurred between 300 and 400°C [60], and for implantation doses similar to the highest phosphorus dose case in this work, the temperature is expected to reach several hundred degrees during the implant.

In the case of the boron implantation, for two lower boron doses (the magenta and cyan spectrum), there was no damage detectable by channeling of the germanium samples, while for the higher boron dose (the orange spectrum) there was detectable damage in the substrate. The sharp peak of the orange spectrum (5×10^{16} cm^{-2} boron) corresponds to damage located at the surface. The backscattering peak disappears with

increasing energy followed by a small increase indicating crystal disorder in both the surface and a sub-surface region. This phenomenon may also be a result of IBIEC combined with heating.

To convert the energy scale to a thickness scale, the reference was that 11.7 keV corresponded to 10 nm. The germanium edge corresponded to the surface; lower energies correspond to signals coming from the deeper part of the germanium sample. Thus, the depth of the amorphous region for 170 keV, 1×10^{15} cm^{-2} phosphorus implant into germanium is about 0.15 μm.

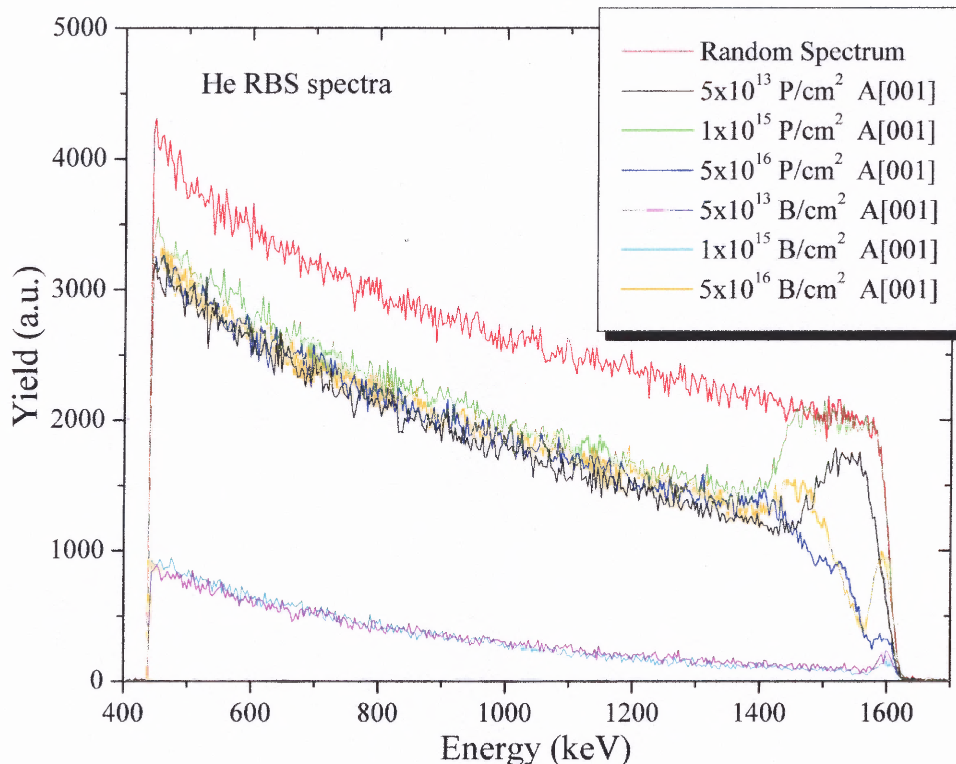

Figure 5.18 The RBS spectra for various boron and phosphorus doses implanted into germanium. The red curve indicates random spectrum.

To quantify the amount of boron and its substitutional fraction, a nuclear reaction in random and in channeling ([001] geometry) was conducted. The $^{11}B(p,\alpha)\ ^{8}Be$ nuclear reaction was used, which is sensitive only to ^{11}B and not to ^{10}B. The nuclear reaction yield from ^{11}B atoms was obtained by using a 650 keV proton beam to exploit the maximum of the broad resonance in the $^{11}B(p,\alpha)\ ^{8}Be$ nuclear reaction cross section. After the reaction, the energy of α particles was measured. The random spectra were collected while rotating the sample around the selected axial direction, with an azimuth angle of 5°. The channeling spectra were collected on [001] axial direction. The substitutional fraction can be obtained using the ratio between the random and channeling yield. Table 5.9 shows the measured boron dose and the substitutional fraction. The data of 5×10^{13} cm^{-2} boron implanted into germanium were not available because of the low implantation boron dose (see the random spectra of 5×10^{16} and 1×10^{15} cm^{-2} boron implant into germanium, Figure 5.19).

Table 5.9 The Result of $^{11}B\ (p,\alpha)\ ^{8}Be$ Nuclear Reaction

Nominal B dose (cm^{-2})	^{11} B Dose (cm^{-2})	Substitutional fraction %
1×10^{15}	$1.3\times10^{15} \pm 0.1\times10^{15}$	16 ± 5
5×10^{16}	$6\times10^{16} \pm 0.2\times10^{16}$	18 ± 8

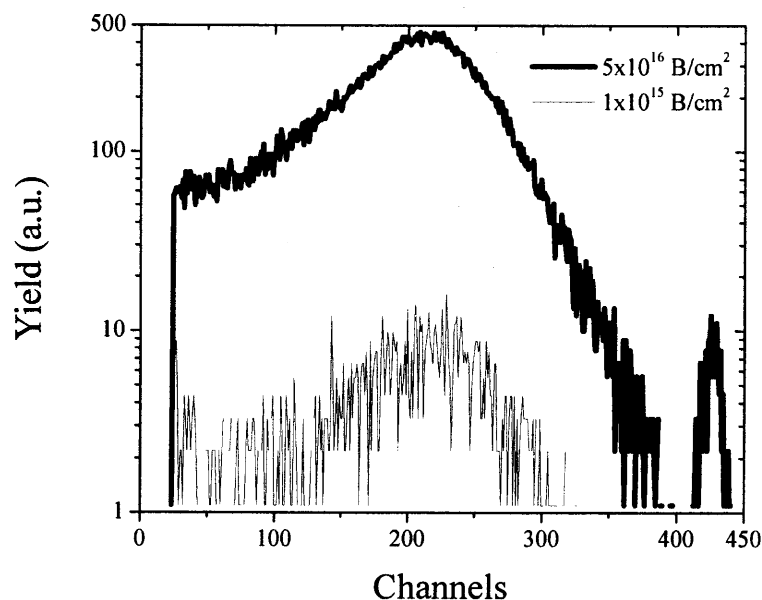

Figure 5.19 The random spectra of α particle from ^{11}B (p,α) ^{8}Be nuclear reaction on 5×10^{16} and 1×10^{15} cm^{-2} boron implant into germanium.

To further examine the crystal damage, the lattice of germanium was probed using x-ray diffraction rocking curves around the 004 reflection, courtesy of G. Bisognin of the University of Padova. Because the lattice constant is sensitive to strain, XRD can sometimes be useful in detecting damage and substitutional dopants. Figure 5.20 shows data observed on the germanium sample implanted with 60 keV, 5×10^{16} cm^{-2} boron (red line). The rocking curve exhibits two features other than the sharp 004 peak resulting from the substrate reflection: (1) a peak at approximately 1000 arcsec displaced from the 004 reflection indicative of a tensily strained layer and (2) a shoulder on the negative displacement of the 004 peak, which can be indicative of compressive strain. The ^{11}B(p,α) ^{8}Be nuclear reaction indicates a large fraction of substitutional boron (i.e. ~ 15%) and for this high dose boron concentrations are of the order of an atomic

percent. A tensily strained layer would be consistent with lattice dilation, which would be expected when large atomic fractions of a smaller atom like boron are incorporated in the germanium lattice. Without modelling it is unclear what the sources of these XRD features are, however. The blue curve of Figure 5.20 is from the XRD rocking curve of the germanium sample implanted with 60 keV, 1×10^{15} cm^{-2} boron. In this case, there is no peak at the right of substrate peak (tensile strain), although there is a less pronounced compressive shoulder (more visible in Figure 5.21). Defects introduced by ion implantation even at smaller boron doses can induce defects and may be the cause of this less pronounced shoulder [61]. The solid black curve in Figure 5.20 corresponds to the 60 keV, 5×10^{13} cm^{-2} boron, which shows no X-ray scattering on either side of the 004 reflection. The rocking curve in this case is indistinguishable from that of a single crystal showing that this low dose implant produces no damage detectable by this technique.

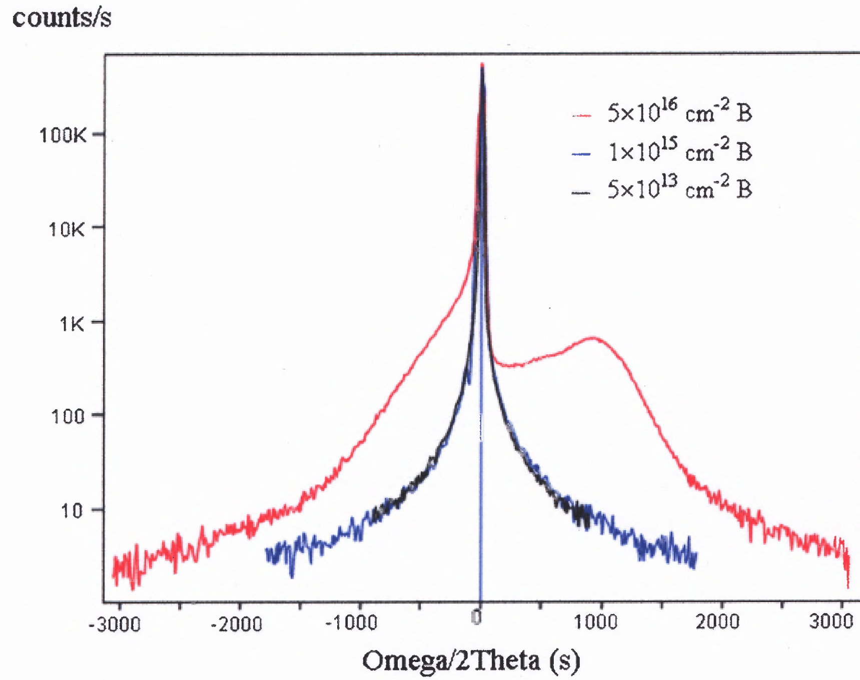

Figure 5.20 The rocking curves for 60 keV boron implantation into germanium with various doses.

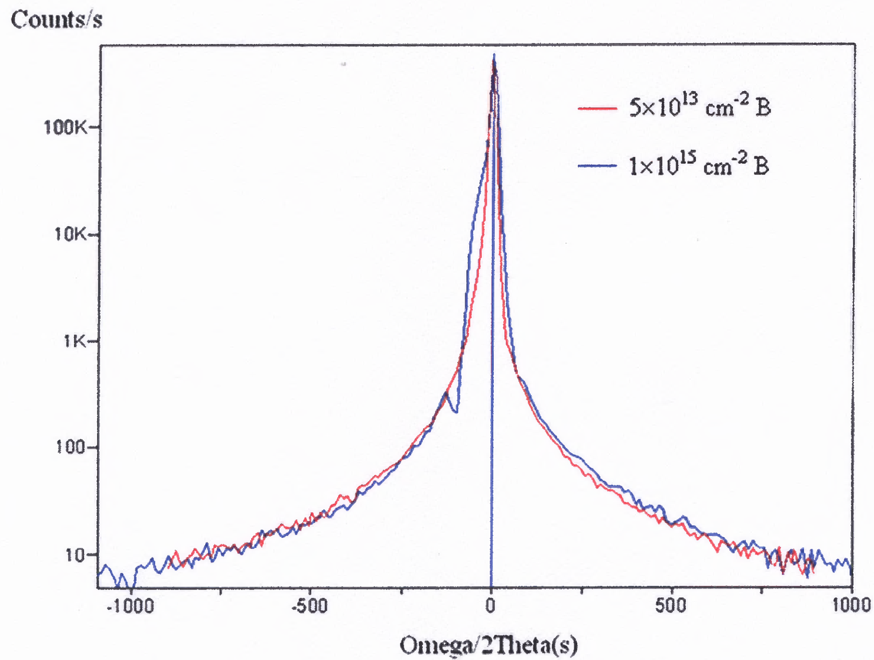

Figure 5.21 Comparison of two rocking curves related to 5×10^{13} and 1×10^{15} cm^{-2} boron implanted into germanium with the energy of 60 keV.

For the phosphorus implant into germanium, the same considerations apply as described for the boron, Figure 5.22. In this case, the blue curve (170 keV, 5×10^{16} cm^{-2} phosphorus) shows the same qualitative features exhibited by the boron case (red curve, 60 keV, 5×10^{16} cm^{-2} boron) of Figure 5.20. In the 1×10^{13} cm^{-2} dose case a new feature is observed, pendelosung fringes, overlapped on the X-ray scattering in the compressive strain side of the rocking curve. The scattering on the compressive strain side of the rocking curve suggests the formation of a highly defective layer (~ 0.201 ± 0.001 μm). The Pendelosung fringes, furthermore, are indicative of X-ray interference between high quality interfaces and suggest that the highly defective layer is in fact buried below a defect free germanium cap layer. Further modeling would be necessary to verify this hypothesis, however, this was not the purpose of this study. In Figure 5.23, the peak related to tensile strain for the highest dose of boron and phosphorus was shown. The case of phosphorus implant was closer to the substrate peak, indicating less tensile strain than in the sample implanted with boron despite implanting the approximately the same number of atoms. This may qualitatively be accounted for by several effects: (1) the smaller lattice mismatch produced by incorporation of the larger phosphorus atom; (2) less substitutional incorporation of phosphorus than boron immediately after implant; (3) more lattice relaxation in the phosphorus doped layer than in the boron case. The p-type layer after phosphorus implant does suggest that this affect may be explained by less substitutional incorporation of phosphorus. To check how pseudomorphically strained the layers are, reciprocal space maps were measured.

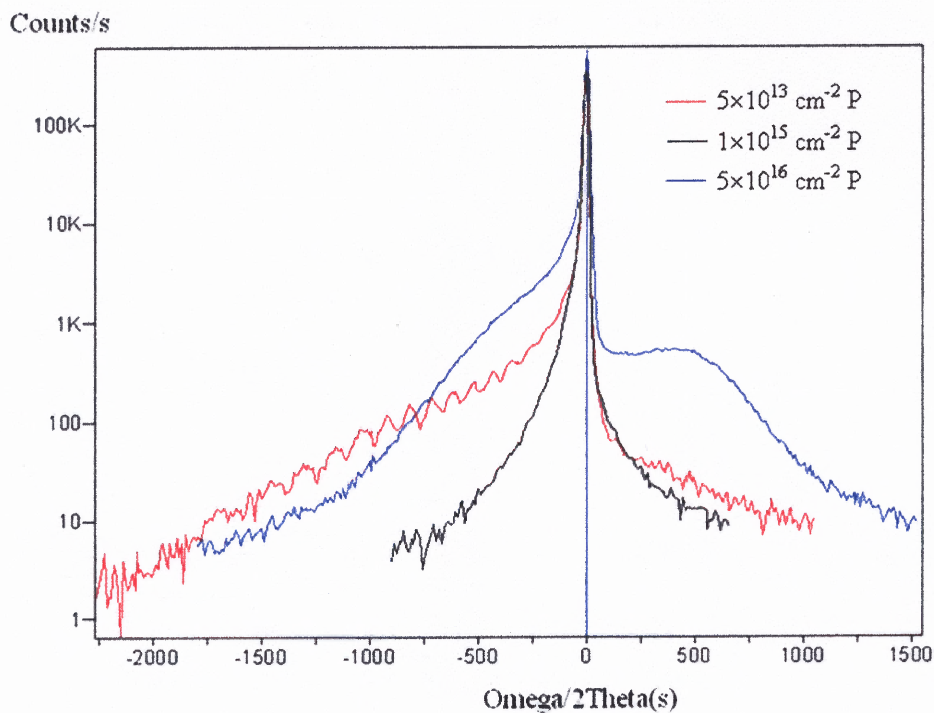

Figure 5.22 The rocking curves for 170 keV phosphorus implantation into germanium with various doses.

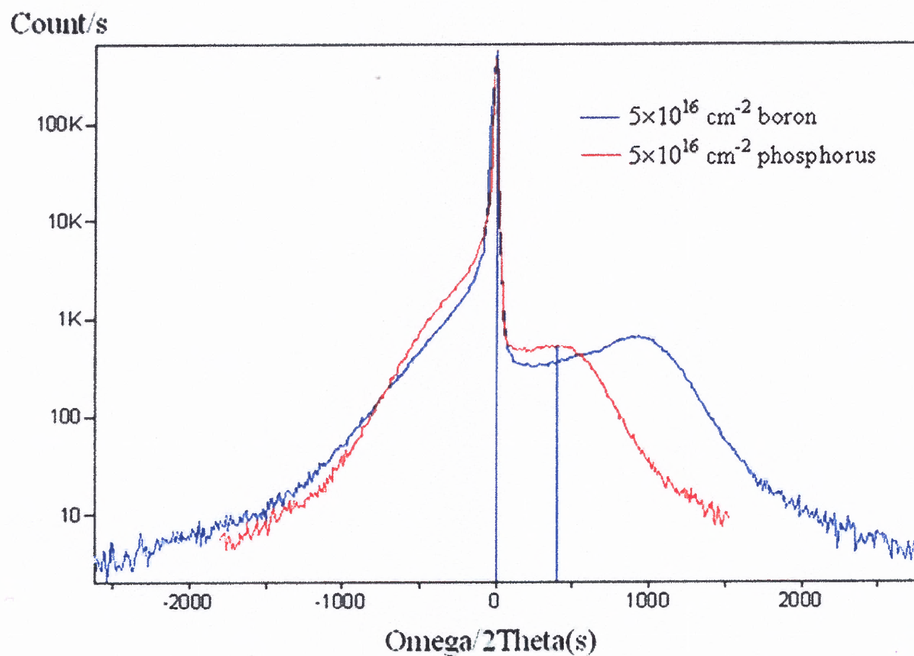

Figure 5.23 Comparison of the rocking curves of boron and phosphorus with the dose of 5×10^{16} cm^{-2}.

In Figure 5.24 (a), the reciprocal space map around (224) reflection of the germanium implanted with 5×10^{16} cm^{-2} boron was shown. It is clear that the boron doped zone was almost fully strained and that the in-plane parameter was almost equal to the germanium substrate parameter (the (224) node of the doped layer was aligned with that of the substrate). Figure 5.24 (b) shows the reciprocal space map around (224) reflection of the germanium implanted with 5×10^{16} cm^{-2} phosphorus. The strain was not so high as in the phosphorus doped zone. The layers in the phosphorus implanted sample are, therefore, not completely pseudomorphically strained indicating that the reduced strain observed in the rocking curve is also partly due to incoherent relaxation. No conclusive observation about the substitutional incorporation in the phosphorus compared to the boron can, therefore, be made.

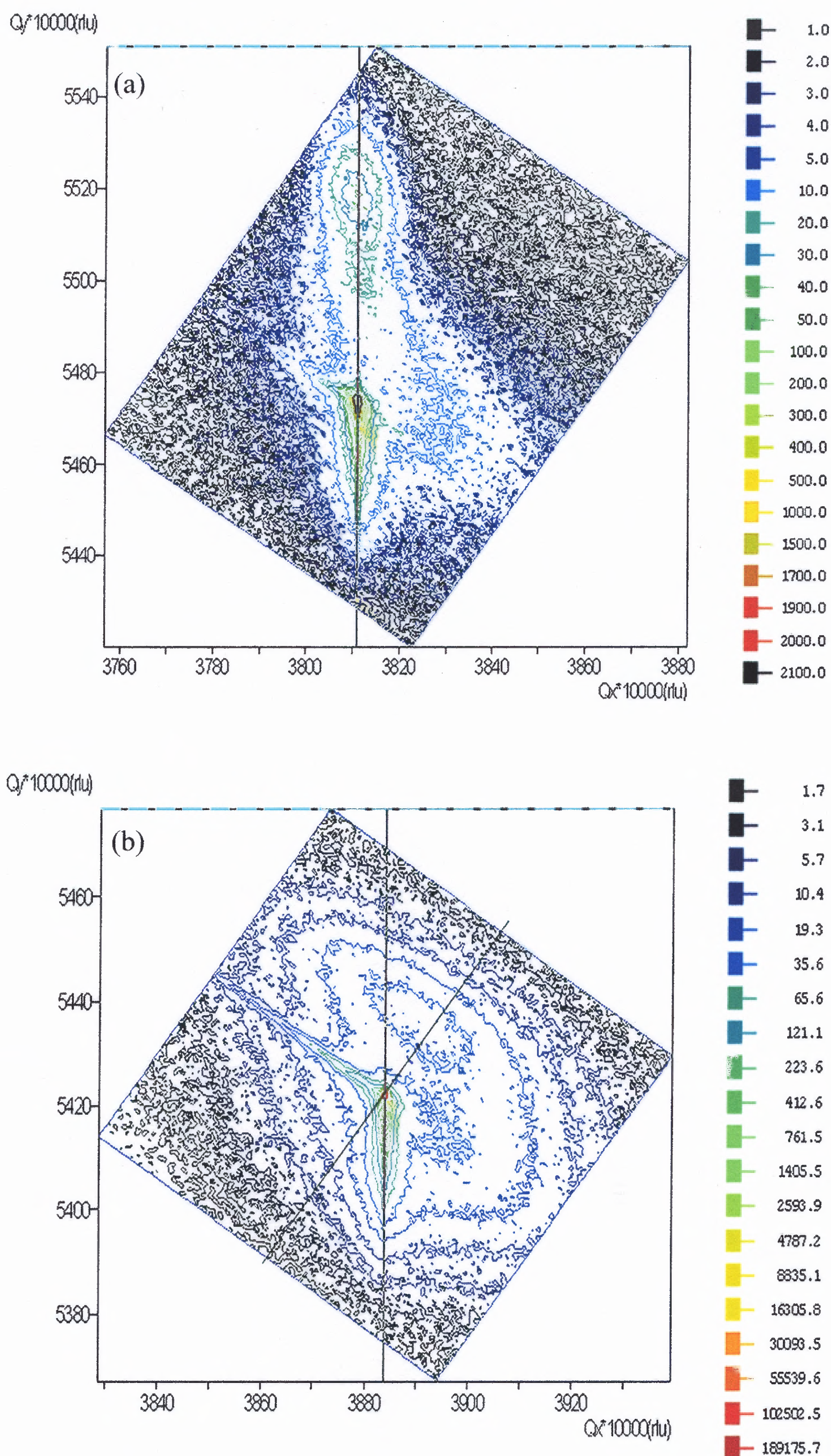

Figure 5.24 The reciprocal space map around (224) reflection of the germanium implanted with 5×10^{16} cm^{-2} (a) boron and (b) phosphorus.

After thermal annealing, the strain due to implantation-induced damage was observed to decrease in the broadening, which indicates that the annealing does indeed partially remove the crystal damage after the 400°C anneal and completely removes the damage after the 600°C anneal.

CHAPTER 6

CONCLUSIONS

A renewed interest in germanium based semiconductor devices has arisen due to advances in alternative gate dielectrics and an increased desire to find silicon CMOS compatible devices that have more desirable properties for optoelectronic and high-speed electronic applications. However, critical process parameters necessary for device design and fabrication, which are typically available for silicon, are not currently available for germanium. Implantation and dopant activation represent two of these primary device fabrication steps for which more characterization and fundamental understanding is needed. In this dissertation, boron and phosphorus implants into germanium before and after annealing were characterized using secondary ion mass spectrometry (SIMS), spreading resistance profiling (SRP), high resolution x-ray diffraction (XRD), Rutherford backscattering spectrometry (RBS), and nuclear reaction analysis (NRA). Numeric simulation (SRIM) and LSS theory were used to better understand the underlying physics of the resulting implant distributions and the combined measurements were used to develop a better understanding of the effects of annealing on dopant activation and diffusion.

Specifically, boron and phosphorus implantation profile in germanium were measured using SIMS, and the first four moments of the distributions were extracted from the SIMS measurements. *Projected ranges* were found to be shallower in germanium than in silicon for the same implant energies for both dopant species, but the boron straggle (i.e. the second moment) was found to be greater in germanium than in

silicon. The qualitative behavior of the first two moments is consistent with the LSS theory's predictions, which gives the first two moment's dependence on implant energy based on calculated electronic and nuclear stopping powers. An analytic fit for the moments dependence on implant energy between the ranges of 20–320 keV was determined, providing values for all four moments over the entire range of energies examined in this work. These moments were used to determine the appropriate Pearson distributions that fit the implant profiles. Pearson parameters were, subsequently, calculated from the first four moments.

The implantation-induced damage was, furthermore, examined by RBS and HRXRD. As expected from SRIM calculations, low doses of boron resulted in no detectable disordering of the germanium substrates, however at the highest dose of boron significant damage was produced in germanium. In the case of phosphorus implantation, substrates were found to be completely amorphized to depths as great as 0.15 μm beginning at a dose of 1×10^{15} cm^{-2}. Interestingly, however, in the highest dose boron and phosphorus cases, evidence of recrystallization during the implant were seen, which was presumably due to solid phase epitaxy produced by the increased temperature during ion implantation. Through channeling experiments, a large fraction (as much as 15%) of the boron was found to be substitutional immediately after implant for doses as high as 5×10^{16} cm^{-2}.

Phosphorus was found not to be active immediately after implant, however, boron was active immediately after implant. The behavior of phosphorus and boron in germanium after 400 and 600°C annealing were characterized using SIMS and SRP. Annealing led to very rapid phosphorus diffusion and increased electron carrier

concentrations, presumably due to annealing of implant damage. Boron implanted germanium, in contrast, showed relatively low resistance (i.e. for the boron dose implanted) p-type surfaces immediately after implantation, and carrier concentrations did not increase with annealing. The combination of SRP, SIMS, RBS, NRA and XRD measurements indicates that a very large fraction of boron is active and resides in substitutional sites immediately after implant for doses as high as 5×10^{16} cm^{-2}, presumably due to recrystalization during implantation. Negligible diffusion was, furthermore, observed in the boron case. Finally, this work is also relevant to the issue of scaling of silicon complementary MOSFETs, which is increasingly challenged by the need to anneal and activate the p-type dopant, boron. Post-implant anneals are well known to lead to rapid diffusion that ultimately defines the size of the device. In this thesis, it is observed that boron implants into pure germanium result in relatively high p-type activation without the need of further annealing. The junction might, therefore, be limited only by the implant rather than diffusion. This observation combined with recent introduction of SiGe to the source/drain region for strained silicon is significant, therefore, as it may offer insight in how future shallow junctions are formed in high germanium content SiGe source/drains. Advantages may exist in moving towards engineering source/drains with very high or pure germanium content for p-channel MOSFETs. In summary, to assist in future device design and modeling, a predictive model for boron or phosphorus implant distributions vs. energy in germanium is presented; and the pre- and post-annealing electrical, structural and diffusion behavior is characterized.

APPENDIX

PROGRAMMING FOR CALCULATION OF MOMENTS

The first four moments can be calculated using the below programming cord for Mathematica software. Using this cord, the first four moments can be easily and fast calculated.

(1) The data import from SIMS data:

```
listge:=Import["name.txt","Table"]

Dimensions[listge]

listge1:=Table[{listge[[i,1]]*10^-4, listge[[i,2]]}, {i,95}]

clistge:=Table[listge[[i,2]],{i,1,95}]

dlistge:=Table[listge[[i,1]]*10^-4,{i,1,95}]
```

(2) The first moment (the *projected range*, R_p) using Equation (2.22):

```
sumwtlst:=clistge dlistge

s1=Plus@@clistge (*equal to dose*)

s2=Plus@@sumwtlst

rp=s2/s1 (*the projected range*)
```

(3) The second moment (the straggle, σ_p), Equation (2.23):

```
m2:=(dlistge-rp)^2

sumsigmalst:=clistge m2

s3=Plus@@sumsigmalst
```

```
var=s3/s1

sigmap=Sqrt[var] (*the straggle*)
```

(4) The third moment (the skewness, γ), Equation (2.24):

```
m3:=(dlistge-rp)^3

sumskelst:=clistge m3

s4=Plus@@sumskelst

ske1=s4/s1

skewness=ske1/(sigmap)^3 (*the skewness*)

ske2=skewness^2
```

(5) The fourth moment (the kurtosis, β), Equation (2.25):

```
m4:=(dlistge-rp)^4

sumkurlst:=clistge m4

s5=Plus@@sumkurlst

kur1=s5/s1

kurtosis=kur1/(sigmap)^4 (*the kurtosis*)
```

(6) The calculation of Pearson parameters, Equation (2.26):

```
c=(2(5*kurtosis-6*ske2-9))^-1

b1=-skewness*sigmap*(kurtosis+3)*c

b0=-sigmap^2*(4*kurtosis-3*ske2)*c

b2=-(2*kurtosis-3*ske2-6)*c
```

(7) The determination of the Pearson type [32]:

```
namuda=ske2 (kurtosis+3)^2 (8 kurtosis-9 ske2-12)-4 (4 kurtosis-3 ske2) (5 kurtosis-6 ske2-9)^2

cond1=(39 ske2+48+6 (ske2+4)^(3/2))/(32-ske2)

(*For Gaussian*)

If[skewness=0 And kurtosis=3, yes,no]

(*Type I*)

If[skewness≠0 And  (ske2+1)≤kurtosis<(3+(3/2) ske2),yes,no]

If[namuda≠0 And c≠Infinity, yes,no]

(*Type II*)

If[skewness=0 And 1≤kurtosis<3, yes,no]

(*Type III*)

If[skewness≠0 And kurtosis=(3+(3/2) ske2), yes,no]

(*Type IV*)

If[0<(b1^2)/(4*b0*b2)<1, yes,no]

(*Type V*)

If[0<ske2<32 And kurtosis=cond1, yes,no]

(*Type VI*)

If[skewness≠0 And (3+(3/2) ske2)<kurtosis<cond1, yes,no]

If[namuda≠0, yes,no]

(*Type VII*)

If[skewness=0 And kurtosis>3, yes,no]

kurtosis1=2.8+2.4*ske2
```

(8) Pearson type I, Equation (2.27):

```
A1=(1/2)*((b1/b2)+Sqrt[(b1/b2)^2-4 b0/b2])

A2=(-1/2)*((b1/b2)-Sqrt[(b1/b2)^2-4 b0/b2])

m1=(A1+b1)/(b2*(A1+A2))

m2=(A2-b1)/(b2*(A1+A2))

If[(m1+1) A2=(m2+1) A1, yes,no]

-A1+rp≤x0≤A2+rp

x1=-A1+rp

x2=A2+rp

f[x_]:=((x*10^-4-rp+A1)^(m1))*((A2+rp-x*10^-4)^(m2))

NIntegrate[f[x]*10.^-4,{x,0,0.5}]

K=dose/NIntegrate[f[x]*10.^-4, {x,0,0.5}]

g[x_]:=K*f[x]
```

(9) Pearson type IV, Equation (2.28):

```
m=-1/(2*b2)

r=-(2+1/b2)

n=-r*b1/Sqrt[4 b0 b2-b1^2]

A=m r b1/n

f[x_]:=(1+((x*10^-4-rp)/A-n/r)^2)^(-m)*Exp[-n ArcTan[(x*10^-4-rp)/A-n/r]]

NIntegrate[f[x]*10.^-4,{x,0,Infinity}]

K=dose/NIntegrate[f[x]*10.^-4, {x,0,Infinity}]

g[x_]:=K*f[x]
```

(10) Pearson type VI, Equation (2.28):

```
A1=(1/2)*((b1/b2)+Sqrt[(b1/b2)^2-4 b0/b2])

A2=(1/2)*((b1/b2)-Sqrt[(b1/b2)^2-4 b0/b2])

q1=-(A1+b1)/(b2*(A1-A2))

q2=-(A2+b1)/(b2*(A1-A2))

If[(q1-1) A2□(q2+1) A1, yes,no]

x0≥-1*A2+rp

x0=-1*A2+rp

f[x_]:=((1+(x*10^-4-rp)/A1)^(-q1))*((1+(x*10^-4-rp)/A2)^(q2))

NIntegrate[f[x]*10.^-4,{x,0,0.5}]

K=dose/NIntegrate[f[x]*10.^-4, {x,0,0.5}]

g[x_]:=K*f[x]
```

REFERENCES

1. R. E. Jones, S. G. Thomas, S. Bharatan, R. Thoma, C. Jasper, T. Zirkle, N. V. Edwards, R. Liu, X. D. Wang, Q. Xie, C. Rosenblad, J. Ramm, G. Isella, H. von Känel, J. Oh, and J. C. Campbell, *IEDM Tech. Dig.* 793 (2002).

2. C. O. Chui, H. Kim, D. Chi, B. B. Triplett, P. C. McIntyre, and K. C. Saraswat, *IEDM Tech. Dig.* 437 (2002).

3. J. Oh, S. Csutak, and J. C. Campbell, *IEEE Photon. Technol. Lett.* **14**, 369 (2002).

4. H. Shang, H. Okorn-Schmidt, K. K. Chan, M. Copel, J. A. Ott, P. M. Kozlowski, S. E. Steen, S. A. Cordes, H. –S. P. Wong, E. C. Jones, and W. E. Haensch, *IEDM Tech. Dig.* 441 (2002).

5. L. Colace, G. Masini, and G. Assanto, *IEEE J. Quantum Electron.* **35**, 1843 (1999).

6. S. Uppal, A. F. W. Willoughby, J. M. Bonar, A. G. R. Evans, N. E. B. Cowern, R. Morris, and M. G. Dowsett, *J. Appl. Phys.* **90**, 4293 (2001).

7. K. S. Jones and E. E. Haller, *J. Appl. Phys.* **61**, 2469 (1987).

8. D. R. Lide, *Chemical Rubber Company Handbook of Chemistry and Physics, 77th* (CRC Press, Boca Raton, FL, 1996).

9. W. Shockley, *Bell Syst. Tech. J.* **28**, 435 (1949).

10. T. Miya, Y. Teramuna, Y. Hosaka, and T. Miyashita, *Electron. Lett.* **15**, 106 (1979).

11. J. M. Senior, *Optical Fiber Communications: Principles and Practice* (Prentice-Hall, London, UK, 1985), p. 330.

12. F. Schäffler, *Semicond. Sci. Technol.* **12**, 1515 (1997).

13. J. F. Gibbons, W. S. Johnson, and S. W. Mylroie, *Projected Range Statistics: Semiconductors and Related Materials, 2nd* (Dowden Hutchinson & Ross, Inc., Stroudsburg, PA, 1975).

14. H. Okamoto, *Desk Handbook: Phase Diagrams for Binary Alloys* (ASM International, Materials Park, OH, 2000), p. 422.

15. J. D. Cressler and G. Niu, *Silicon-Germanium Heterojunction Bipolar Transistors* (Artech House, Boston, MA, 2003), pp. 557-559.

16. S. Wolf and R. N. Tauber, *Silicon Processing for the VLSI Era*, *2nd*, **1** (Lattice Press, Sunset Beach, CA, 2000), Chap. 1, p. 1; Chap. 10, pp. 372-378.

17. M. Shur, *Physics of Semiconductor Devices* (Prentice-Hall, Englewood Cliffs, NJ, 1990), Chap. 5, p. 478.

18. B. G. Streetman and S. Banerjee, *Solid State Electronic Devices*, *5th* (Prentice-Hall, Upper Saddle River, NJ, 2000), Chap. 3, pp. 55-107.

19. Loffe Physico-Technical Institute (2003, July 8), *Physical Properties of Semiconductors*. http://www.ioffe.rssi.ru/SVA/NSM/Semicond/index.html (24 March 2004).

20. K. Hess, *Advanced Theory of Semiconductor Devices* (IEEE Press, New York, NY, 2000), Chap. 3, pp. 46-50.

21. G. Masini, L. Colace, and G. Assanto, *Mater. Sci. Eng. B* **89**, 2 (2002).

22. J. F. Gibbons, *Proc. IEEE* **56**, 295 (1968).

23. M. D. Giles, *VLSI Technology*, *2nd*, edited by S. M. Sze (McGraw-Hill, New York, 1988), Chap. 8, pp. 328-335, p. 344; J. B. Bindell, *ibid.*, Chap. 12, p. 543.

24. M. T. Robinson and I. M. Torrens, *Phys. Rev. B* **9**, 5008 (1974).

25. J. Lindhard and M. Scharff, *Phys. Rev.* **124**, 128 (1961).

26. J. F. Ziegler, J. P. Biersack, and U. Littmark, *The Stopping and Range of Ions in Solids*, **1** (Pergamon, New York, 1985).

27. W. P. Petersen and W. Fichtner, *IEEE Trans. Electron Devices* **30**, 1011 (1983).

28. J. F. Ziegler, *Handbook of Ion Implantation Technology* (North-Holland, New York, 1992), p. 42.

29. D. S. Gemmell, *Rev. Mod. Phys.* **46**, 129 (1974).

30. J. F. Gibbons and S. Mylroie, *Appl. Phys. Lett.* **22**, 568 (1973).

31. J. B. Sanders, *Can. J. Phys.* **46**, 455 (1968).

32. S. Ahmed, C. J. Barbero, and T. W. Sigmon, *J. Appl. Phys.* **77**, 6194 (1995).

33. D. G. Ashworth, R. Oven, and B. Mundin, *J. Phys. D* **23**, 870 (1990).

34. S. Uppal, A. F. W. Willoughby, J. M. Bonar, A. G. R. Evans, N. E. B. Cowern, R. Morris, and M. G. Dowsett, *Physica B* **308-310**, 525 (2001).

35. R. Fleming of Charles Evans & Associates (1995), *Secondary Ion Mass Spectrometry Theory Tutorial*, http://www.eaglabs.com/cai/simstheo/caistheo.htm (30 March 2004).

36. R. G. Wilson, F. A. Stevie, and C. W. Magee, *Secondary Ion Mass Spectrometry* (John Wiley & Sons, New York, 1989).

37. D. E. Sykes, *Methods of Surface Analysis: Techniques and Applications*, edited by J. M. Walls (Cambridge University Press, New York, 1989), Chap. 7.

38. R. G. Mazur and P. H. Dickey, *J. Electrochem. Soc.* **113**, 255 (1966).

39. S. M. Sze and J. C. Irvin, *Solid-State Electron.* **11**, 599 (1968).

40. D. B. Cuttriss, *Bell Syst. Tech. J.* **40**, 509 (1961).

41. Solecon Laboratories, Inc. (2004, February 2), *Dose, Sheet and 4 Point Probe*, http://www.solecon.com/pdf/dose_sheet_and_four-point_probe_sheet.pdf (22 April 2004).

42. C. O. Chui, K. Gopalakrishnan, P. B. Griffin, and J. D. Plummer, *Appl. Phys. Lett.* **83**, 3275 (2003).

43. S. Voss, N. A. Stolwijk, and H. Bracht, *J. Appl. Phys.* **92**, 4809 (2002).

44. S. Prussin, D. I. Margolese, and R. N. Tauber, *J. Appl. Phys.* **57**, 180 (1985).

45. J. F. Gibbons, *Proc. IEEE* **60**, 1062 (1972).

46. J. Boussey-Said, G. Ghibaudo, I. Stoemenos, and P. Zaumseil, *J. Appl. Phys.* **72**, 61 (1992).

47. M. Ohring, *The Materials Science of Thin Films* (Academic Press, San Diego, CA, 1992), Chap. 1, p. 7; Chap. 6, p. 289.

48. B. D. Cullity and S. R. Stock, *Elements of X-Ray Diffraction*, *3rd* (Prentice Hall, Upper Saddle River, NJ, 2001).

49. F. Cembali, M. Servidori, and A. Zani, *Solid-State Electron.* **28**, 933 (1985).

50. B. C. Larson and J. F. Bathorst, *J. Appl. Phys.* **51**, 3181 (1980).

51. *Annual Book of ASTM Standards*, **10.05**, (West Conshohocken, PA, 1999), p. 41.

52. R. E. Hummel, *Electronic Properties of Materials*, 2nd (Springer-Verlag, New York, NY, 1993), Chap. 8, p. 110.

53. H. W. Werner, *Thin Film and Depth Profile Analysis*, edited by H. Oechsner (Springer-Verlag, Berlin, 1984), p. 5.

54. K. B. Winterbon, *Appl. Phys. Lett.* **42**, 205 (1983).

55. S. M. Sze, *Physics of Semiconductor Devices*, 2nd (Wiley-Interscience, New York, NY, 1981), p. 69.

56. V. M. Glazov and V. S. Zemskov, *Physicochemical Principles of Semiconductor Doping* (Israel Program for Scientific Translations, Jerusalem, 1968), Chap. 2, p. 119, p. 140.

57. G. G. Devyatykh, V. K. Vasil'ev, V. A. Gavva, A. V. Gusev, Y. A. Danilov, E. S. Zharkov, and G. A. Maksimov, *Inorganic Materials* **32**, 1258 (1996).

58. S. Mader, *Ion Implantation Science and Technology*, edited by J. F. Ziegler (Academic Press, Orlando, FL, 1984), p. 109.

59. P. A. Stolk, H. –J. Gossmann, D. J. Eaglesham, D. C. Jacobson, C. S. Rafferty, G. H. Gilmer, M. Jaraíz, J. M. Poate, H. S. Luftman, and T. E. Haynes, *J. Appl. Phys.* **81**, 6031 (1997).

60. L. Csepregi, R. P. Küllen, and J. W. Mayer, *Solid State Commun.* **21**, 1019 (1977).

61. S. Tian, M. F. Morris, S. J. Morris, B. Obradovic, G. Wang, A. F. Tasch, and C. M. Snell, *IEEE Trans. Electron Devices* **45**, 1226 (1998).